CO_2 geological sequestration and utilization for enhanced gas/oil recovery from molecular perspectives

by

Mingshan Zhang

A thesis submitted in partial fulfillment of the requirements for the degree of

Doctor of Philosophy

in

Petroleum Engineering

Department of Civil and Environmental Engineering
University of Alberta

Abstract

Atmospheric CO_2 concentration has been gradually growing since the industrial revolution, leading to climate change and global warming. As a result, carbon capture, utilization, and sequestration (CCUS) has become utterly important for human society. CO_2 geological sequestration in depleted shale gas reservoirs is regarded as a promising strategy to mitigate the emission of CO_2. As one of the typical clay minerals in shale reservoirs, kaolinite presents two structurally and chemically distinct basal surfaces known as siloxane and gibbsite surfaces which can significantly affect CO_2 adsorption in kaolinite nanopores, especially in the presence of water. Nevertheless, due to the complicated surface properties and pore structures, it is practically impossible to distinguish the contributions from two distinct kaolinite surfaces for CO_2 adsorption. In addition, to the best of our knowledge, the effect of moisture on CO_2 adsorption in different kaolinite nanopores is rarely reported. We systematically explored CO_2 adsorption in partially water-saturated kaolinite nanopores by molecular dynamics (MD) and Grand canonical Monte Carlo (GCMC) simulations using the flexible clay model. In the absence of water, CO_2 presents a stronger adsorption ability on gibbsite surfaces. In gibbsite pores, the water tends to spread out on the surface forming a thin film while water bridges are observed in siloxane pores. In siloxane mesopores, a more CO_2-wet surface appears as pressure increases, while it is not obvious in micropores because of stronger confinement effects. In general, the presence of water will result in the reduction of CO_2 sequestration in both gibbsite and siloxane pores, while a slight enhancement is observed in siloxane mesopores when the pressure is quite low.

CO_2 utilization for enhancing gas recovery has been attracting extensive attention as it can greatly alleviate the financial burden from CO_2 capture while it can also achieve CO_2 sequestration in the deep formations. Compared with the conventional reservoirs, shale has heterogeneous rock

compositions consisting of organic and inorganic matters and some shale formations contain anextensive number of heavier alkanes, such as ethane (C2) and propane (C3). While CO_2 huff-n-puff is proved to be an effective method to enhance recovery of methane (C1), competitive adsorption between shale gas mixtures (C1-C2-C3) and CO_2 in organic and clay minerals remains unexplored. On the other hand, the different recovery mechanisms of hydrocarbon mixtures during pressure drop, CO_2 huff, and CO_2 huff are still unclear. We used Grand Canonical Monte Carlo (GCMC) simulations to study competitive sorption of C1-C2-C3 and C1-C2-C3-CO_2 mixtures in shale organic and inorganic nanopores under different production schemes. We found that while C1 in the adsorption layer can be readily recovered during pressure drawdown, C2 and C3 are trapped in pores, especially in organic micropores. CO_2 injection can effectively recover each component in the adsorption layer in organic pores, while in inorganic pores, the adsorption layer is dominated by CO_2 molecules, displacing all hydrocarbon components.

Additionally, application of CO_2 responsive surfactants provides a novel idea for economical and sustainable oil production. While the experimental work can test and design a promising smart surfactant formula for efficient O/W emulsification and demulsification processes, the microscopic structural properties and interface hydration structures related to CO_2 switching mechanisms from molecular perspectives remain unclear. MD simulations are employed to carefully study the interfacial properties of n-heptane/water emulsion before and after purging CO_2 using lauric acids (LA) as the surfactant. Before purging CO_2, the deprotonated lauric acid (DLA) help to form and stabilize O/W emulsion droplets in aqueous solution due to high interface activity and strong surface electrostatic repulsion, whereas the protonation of lauric acid (PLA) arising from CO_2 injection results in the coalescence of emulsion droplets thanks to the increased IFT and surface charge neutralization, which is also in line the potential mean force (PMF) calclation resutls.

Preface

All the contents (except Introduction and Conclusion Chapters) have been published in the peer-reviewed journals or will be submmited to the journal for peer review. **Chapter 3** has been submmited to *Chemical Engineering Journal* for peer review. **Chapter 4** has been published in *Chemical Engineering Journal* (*Zhang et al*., 382, 2020). **Chapter 5** has been submmited to *Fuel* for peer review. I was responsible for setting up and running the simulations, analyzing the data, and writing and editing these papers. My co-authors were responsible for providing valuable technical supports and insightful discussion and comments as well as computing resource (supercomputers) and reviewing and revising the manuscript drafts. The necessary approvals to include the journal papers as chapters in this work are provided in sequential order in the Copyright Permissions section.

Acknowledgements

Throughout my PhD program, I have received a great number of help and support from my supervisor, friends and family, which drives me to make progress and warms my heart on my tough days.

Firstly, I would like to express my sincere gratitude to my supervisor, Dr. Zhehui Jin. Without his kind and patient guidance, I would not never have accomplished these present works and become an independent researcher. In addition, I would like to thank China Scholarship Council for the financial support and Compute Canada for providing the computational resource and technique support. Meanwhile, I would also extend my thanks to Dr. Huazhou Li, Dr. Nobuo Maeda, Dr. Juliana Leung, Dr. Liangliang Huang for being my examination committee members and providing me with instructive suggestions to improve my work.

I would like to acknowledge my colleagues (Wenhui Li, Yiling Nan, Wanying Pang, Yingnan Wang, Yinuo Zhao and Haoxiang Wang) in our group for their kind suggestions and critical questions. I would also offer my thanks to my roommates (Shiyuan Zhan and Yandong Yang) who accompany me a lot in Edmonton and cook delicious food for me. In addition, I would like to present my sincere gratitude to my friends who help me a lot in my academic studies (Dr Pan Bin, Dr. Hui Mao, Dr. Meiming Gao, Dr. Yi Lu, Dr. Yang Liu)

My thanks would also go to my beloved my parents (Huazheng Zhang and Lanying Song) and my two elder sisters (Meiming Zhang and Mingfeng Zhang) for their endless love and unconditional support.

Finally, special thanks to Wenwen Zhai, my girlfriend. We experienced a long-distance

relationship for four years during my PhD study and we made it eventually thanks to our persistence and trust. She spent her most precious youth time to accompany me without any complaints or regrets. Without her, I cannot imagine what my life will be. Thanks a lot for her patient waiting and support and she deserves the best happiness in the world.

Be grateful to everyone who has helped you. Enjoy the life and get along well with others. Just like the songs in Friends

I'll be there for you when the rain starts to pour

I'll be there for you like I've been there before

I'll be there for you 'cause you're there for me too

Table of Contents

List of Tables

List of Figures

Chaper 1 Introduction

1.1 Research background and motivation

Due to human activities, a great amount of CO_2 is emitted to the atmosphere, leading to climate change and global warming [1, 2]. Since the second industrial revolution, the atmospheric CO_2 concentration has increased from 290 ppm [3] to more than 400 ppm [4] and the averaged global temperature experienced an increment of 1.5 degree [5]. The global warning has caused a series of environmental issues such as glaciers melting [6], ocean acidification [7] and more frequent EL Nino phenomenon [8]. Therefore, it is imperative to reduce and control CO_2 emission to maintain a healthy atmosphere for the sustainable development of human beings. Carbon capture, utilization, and sequestration (CCUS) technology [9-11] is regarded as a promising strategy to control and mitigate the emission of CO_2, during which CO_2 would be captured via physical or chemical techniques or CO_2 is pumped into underground and stored in formations permanently to isolate their circulation in atmosphere. Geological sequestration [12-14] is proved to be an effective method to achieve the CO_2 storage in deep formations and has been initiated in many countries. Typically, several geological zones can be considered as the target sequestration sites, such as saline aquifers, oil and gas reservoirs, unminable coal beds and so on [15]. A short description of all storage sites is summarized as follows:

1). Saline aquifer: CO_2 sequestration in saline geological formations is considered as the most feasible technology because of the large storage capacities and high permeability [16]. The saline aquifers are estimated to have a storage capacity potential between 2400 to 21000 Gt CO_2 in the United States of America and North America [17]. So far, four kinds of trapping mechanism are proposed for explaining how CO_2 is stored in saline aquifers: structural and stratigraphic trapping, capillary trapping, solubility trapping and mineral trapping [16].

2). Depleted oil and gas reservoirs: oil and gas fields which have been considered uneconomical for further production of hydrocarbons are suitable candidates for CO_2 geological sequestration. First, the depleted oil and gas reservoirs have been extensively investigated before and during the oil exploitation stage. That is to say, the properties of reseviors have been adequately characterized including the mineral compositions, porosity, permeability and so on. On the other hand, the underground and surface infrastructure are already available and could be directly used for CO_2 storage injection. More importantly, the injection of CO_2 is favorable for enhancing oil or gas recovery which compensate the capital investment during CO_2 sequestration. The estimated CO_2 storage capacity in depleted oil and gas reservoir is around 200 Gt in the United States of America and North America [17].

3). Unminable coal beds. CO_2 has been employed for the recovery of methane from coal seams during the enhanced coal bed methane (ECBM) recovery process [18]. Coal beds have very large fracture networks through which CO_2 molecules can diffuse into the matrix and displace tightly adsorbed methane. Estimation of CO_2 storage in global unminable coal seams lie in the range of 3-200 Gt [19].

1.1.1 CO_2 sequestration in depleted shale reservoirs

Recently, CO_2 sequestration in shale reservoirs [12, 14, 20] has attracted worldwide attention thanks to thanks to the well-developed nanoscale pore structures. Different from the conventional reservoirs, small pores with the pore size ranging from several to hundreds of angstroms are widely distributed in the shale formations [21, 22]. Fluid-surface interaction is significant in these nanopores [23-25] which results in strong adsorption and provides substantial adsorption sites for CO_2 sequestrations. Meanwhile, shale reservoir has heterogeneous rock compositions consisting of organic and inorganic matters [26, 27]. Organic matter is mainly composed of kerogen while

the clay minerals account for most of the inorganic parts. In addition, shale formation can be partially saturated with water generated in early sediment deposition and subsequent hydraulic fracturing process and the water content in shale reservoir ranges from 10% to 30% of the pore volume [28, 29]. Kaolinite is a typical 1:1 clay, which has two structurally and chemically distinct basal surfaces known as siloxane and gibbsite surfaces [30, 31] as shown in **Figure 1.1**. It is reported that gibbsite surfaces are quite hydrophilic with a water contact angle (CA) of less than 10° thanks to the strong H-bonding interaction between water and surface -OH groups, while the siloxane surfaces present strongly CO_2-wetting characteristics (water CA>140°) [32]. The distinct surface properties would result in quite different interfacial phenomena and significantly influence the water structures. Xiong *et al*. [33] and Hao *et al*. [34] reported that water in partially water-saturated clay nanopores can form either thin film on the surfaces or bridge depending on surface properties which can greatly influence gas-water coexistence and hydrocarbon transport behaviors. As a result, the distinguished surfaces of kaolinite are predicted to significantly influence the CO_2 sequestration in kaolinite nanopores, especially in the presence of water. Therefore, the fundamental understanding and knowledge about the CO_2 adsorption and moisture effects in different kaolinite nanopores can provide important insights into CO_2 storage estimation in depleted shale formations.

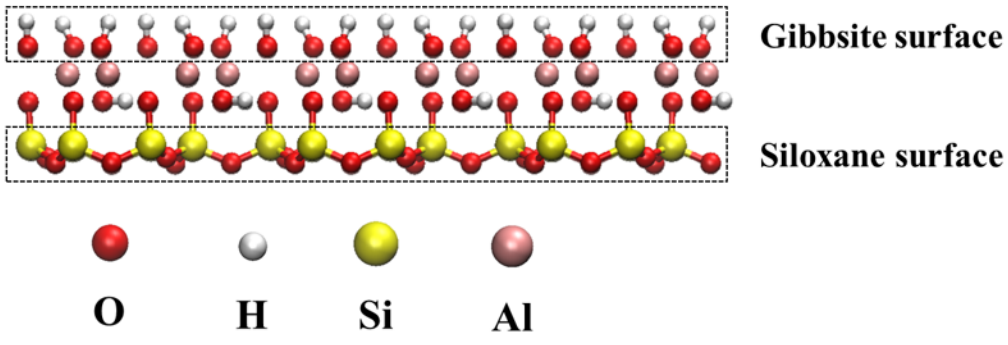

Figure 1.1 Schematic strucure of kaolinite mineral.

1.1.2 CO_2 huff-and-puff for enhancing gas recovery

To alleviate the economic pressure of captical investment during CCS process, CO_2 utilization [35, 36] for enhanced gas and oil recovery has also been implemented in practice. Strong surface adsorption in shale nanopores results in a great amount of adsorbed gas (up to 85% of total gas content) [37] making it difficult to be recovered just relying on pressure drop. CO_2 huff-and-puff in shale formation has been proved to be an effective method to enhance gas recovery thanks to the competitive adsorption [38-40]. The huff-n-puff process is generally operated by three different stages: huff (CO_2 injection), soaking, and puff (pressure drawdown). Different recovery mechanisms would occur for different opreation stages during CO_2 huff-and-puff.

Shale has heterogeneous rock compositions consisting of organic and inorganic matters [26, 41-46]. Organic matter is mainly composed of kerogen, which provides a significant contribution to gas sorption in shale [42, 47-50]. Inorganic matters, such as illite which is a kind of typical clay mineral, can contain extensive amount of nanoscale pores and also greatly contribute to the gas-in-place (GIP) in shale [48, 51-53]. While methane (C1) accounts for most of the gas component in shale gas reserviors, some shale formations contain extensive amount of heavier alkanes [26, 54], such as ethane (C2) and propane (C3), which are important energy supplies and industrail raw materials for our daily life. Therefore, understanding the competitive sorption between hydrocarbon mixtures (C1-C2-C3) and CO_2 in organic and inorganic nanopores may provide key insights into the gas recovery mechanism during CO_2 huff-n-puff process in shale reserviors.

1.1.3 CO_2 responsive surfactants

The application of CO_2 responsive surfactants is another type CO_2 utilization in oil production [55, 56]. As an effective enhanced oil recovery (EOR) technique [57], surfactant flooding has been widely used to further recover residual oil [58, 59]. One of the working mechanisms for surfactant

flooding is to reduce oil-water interfacial tension (IFT) thanks to the amphiphilic characteristics of surfactants [60, 61], which is favorable for the formation of stable oil-in-water (O/W) emulsions. While the formation of stable oil-in-water (O/W) emulsions is favorable for improving both microscopic displacement and macroscopic sweep efficiencies [62], it is not welcomed during oil-water seperation stages due to the increasing difficulties in breaking up the stable emulsions. In this regard, CO_2-responsive surfactants have attracted great attention among scientists and engineers in recent years due to their reversible conversions between emulsification and demulsification [61, 63]. The switching process can be achieved by purging CO_2 or N_2, during which the surface activity of CO_2-responsive surfactants can be switched on or off due to the pH change [56]. Understanding the microscopic structural properties and interface hydration structures related to CO_2 switching mechanisms is critical for designing and picking high performance CO_2 responsive surfactants.

1.2 Problem Statement

CO_2 adsorption amount in kaolinite is a crucial parameter for the estimation of CO_2 sequestration in shale reservoirs. It is well-known that kaolinite has two distinct surfaces exhibiting quite different wettability and surface structure, which would significantly influence the interfacial behaviors. While previous experimental work can measure the CO_2 adsorption capacity with pure kaolinite samples, due to the complicated surface properties and pore structures, it is practically impossible to distinguish the contributions from two distinct kaolinite surfaces. In addition, it is reported that the presence of water plays an important role in regulating CO_2 adsorption in clay minerals, however to the best of our knowledge, the effect of moisture on CO_2 adsorption in kaolinite has been rarely reported.

Shale reservoir has heterogeneous rock compositions consisting of organic and inorganic matters. Organic matter is mainly composed of kerogen, which provides a significant contribution to gas sorption in shale. Inorganic matters, such as clay minerals (i.e., illite, montmorillonite, and kaolinite, etc.), can contain extensive amount of nanoscale pores. Distinguishing the gas adsorption in different minerals is of great importance for the comprehensive evaluation of gas-in-place (GIP) in shale and provide important insights into shale gas production. The CO_2 huff-n-puff process is proved to be an effective way to extract more shale gas from reservoir. Unfortunately, the competitive sorption between hydrocarbon mixtures (C1-C2-C3) and CO_2 remain unclear.

CO_2-responsive surfactants can undertake different tasks (emulsification and demulsification) in different production stages through CO_2 injection or removal, which make oil production economically viable and environmentally sustainable. While the experimental work can design or pick a promising CO_2-responsive surfactant formula for efficient O/W emulsification and demulsification processes, the microscopic structural properties and interface hydration structures related to CO_2 switching mechanisms from molecular perspectives still remain unclear.

Therefore, the unsolved issues mentioned above all is summarized as below

- Considering the different surface types of kaolinite, which surface contributes more to the CO_2 sequestration in kaolinite nanopores in the absence of water?
- Kaolinite nanopores usually contain a great amount of water making it partially saturated with water, how surface property influences the water structure and accordingly affect the following CO_2 adsorption?
- Shale consists of organic and inorganic matters and contains a fraction of the heavier components such as ethane and propane. How CO_2 displace the hydrocarbon from different

nanopores and does it work for the heavy component? What's the recovery difference between CO_2 huff, CO_2 puff and pressure drop process?

- CO_2 responsive surfactants demonstrate excellent emulsification ability before injecting CO_2 while a rapid demulsification is observed after CO_2 purging. What's the driving forces and mechanisms to explain their CO_2 responsiveness?

1.3 Objectives

This research has two main objectives. i) is to investigate CO_2 adsorption characteristics in different shale nanoporous medias containing water or hydrocarbons from statistical thermodynamics approaches. ii) interfacial properties in the O/W systems before and after CO2 purging related to CO_2 responsive mechanisms. To achieve this, the objectives are listed as follows:

- To investigate the CO_2 adsorption in kaolinite nanopores devoid of any fluids with different pore surfaces at various pressures by molecular simulation and compare the difference between siloxane and gibbsite pores.
- To study the CO_2 adsorption behaviors in different kaolinite nanopores over a wide range of pressures with a water concentration of 0.2 g/cm^3 and consider the pore size effects.
- To explore C1-C2-C3 and CO_2 competitive adsorption in shale organic (graphene) and inorganic (illite) nanopores and figure out the recovery mechanisms between CO_2 huff and CO_2 puff process.
- To study the interfacial properties and hydration structure at oil and water interface in the presence of CO_2 responsive surfactants before and after purging CO_2.

1.4 Thesis Structure

This thesis is divided into 6 chapters. **Chapter 1** includes the research background, the problem statement, and the major research objectives. **Chapter 2** describes the fundamental principle and

several basic calculation methods of molecular simulations. **Chapter 3** interprets the effect of surface properties on CO_2 adsorption in dry and water-partially saturated kaolinite nanopores. We explicitly discussed the water structure in different pores and analyzed the effect of water on CO_2 distributions and CO_2 sequestration amount. **Chapter 4** studies the CO_2 competitive adsorption with C1-C2-C3 mixtures in graphene and illite nanopores and reveals distinct recovery mechanisms in these two medias. Furthermore, it demonstrates that the CO_2 huff and puff process presents different recovery mechanisms and CO_2 puff is similar to the pressure drop which cannot displace heavy component from the nanopores. **Chapter 5** switches to CO_2 responsive surfactants**.** The interfacial properties and hydration structure at oil-water interface of the O/W emulsion droplets are carefully studied and the CO_2 responsive mechanisms are disclosed. **Chapter 6** lists the key findings and the limitations of this study and makes a plan for the future work. All the supporting information for helping understand the main text are combined and presented in the Appendices section after **Chapter 6**. Likewise, all the references appearing in the main text and Appendices are combined and listed after Appendices**.**

Chaper 2 Methodology

While it is challenging for experiments to directly reveal adsorption mechanism and observe interfacial phenomona in nano length, statistical thermodynamic approaches such as Monte Carlo (MC) simulation [64], molecular dynamics (MD) simulation [65] are capable of exploring the interfacial phenomena on the nanoscale and allow for the investigation of the specific mineral surface with the full control of computing conditions, thus providing fundamental understandings about the underlying physics. In this section, some basic concepts as well as their calculation principles are briefly illustrated.

2.1 Overview

Molecular simulations are powerful tools in science and engineering, widely adopted in applications ranging from drug discovery to materials design from molecular level. It can be applied to explore the interfacial properties in the scale of nanometers, which are hardly accessible for experiments. In this regard, molecular simulation can help reveal the underlying mechanisms from molecular level and predict the molecular structure, which can be used to explain the macroscopic phenomena and material or drug design. Therefore, molecular simulation holds its unique merits as a potent alternative and supplement to experiments. In addition, molecular simulation can be easily carried out under extreme conditions (e.g., high temperature, high pressure and poison environments) which must be taken seriously in lab conditions.

Generally, molecular simulation methods can be classified as quantum mechanics (QM) methods [66], which treat electrons as the fundamental interactive particles of the system, and classical mechanics (CM) methods treating individual atoms or groups of atoms as the fundamental interactive particles of the system. Since QM calculation is out of the scope of this thesis, we won't give much discussions on this method. In this thesis paper, we mainly focus on the classical

molecular simulation including molecular dynamics (MD) simulation and Monto Carlo (MC) simulation, which have been broadly used to investigate the gas adsorption in nanopores and interfacial behaviors of emulsion droplets.

2.2 Statistical Ensemble

The system can be described using an ensemble [67], which is an idealization consisting a large number of possible states that the real system might be in. Molecular simulations calculate the properties of a chosen system based on the principles of statistical mechanics by averaging over all possible states. Different ensembles are defined depending on interaction between the studied system and its surroundings, from completely isolated (e.g., microcanonical ensemble) to completely open to outside environments (e.g., grand canonical ensemble). Microcanonical ensemble (also called NVE ensemble) stands for an isolated system with fixed number of particles (N), volume (V), and energy (E). There is no transfer of energy or matter between the system and the surroundings. Canonical ensemble (also called NVT ensemble) presents a system in which energy can transfer between system and surroundings, but matter cannot. This system is described as being immersed in a quiet large heat bath with a temperature of T. In this way, it has constant number of particles (N), volume (V), and temperature (T). Similar to the NVT ensemble, in the isothermal-isobaric ensemble (also called NPT ensemble), energy can transfer across the boundary, while matter cannot, which leads to a fixed particle number. The volume of the system can change with internal pressure of the system to match the pressure exerted on the system by its surroundings. Grand canonical ensemble (μVT ensemble) describes a system allowing to exchange mass and energy with surroundings with a fixed chemical potential (μ), volume (V), and temperature (T), which is widely used to study the adsorption behaviors in nanopores. While different ensembles

should obtain the equivalent thermodynamic properties, it is better to choose a proper ensemble according to different simulation system settings.

Statistical mechanics usually deals with ensemble average that can be compared with the macroscopic property observed in experiments. An ensemble average is an average taken over a large number of replicas of the system considered simultaneously, for example, in the canonical ensemble:

$$\langle A \rangle_{ensemble} = \frac{\iint A e^{-\frac{H}{k_B T}} d\boldsymbol{p}_1 \ldots d\boldsymbol{p}_N d\boldsymbol{r}_1 \ldots d\boldsymbol{r}_N}{\iint e^{-\frac{H}{k_B T}} d\boldsymbol{p}_1 \ldots d\boldsymbol{p}_N d\boldsymbol{r}_1 \ldots d\boldsymbol{r}_N}, \tag{2-1}$$

where H is the Hamiltonian energy, $\boldsymbol{p}_i$ is momentum of *i*th atom, $\boldsymbol{r}_i$ is the position of *i*th atom, k_B is the Boltzmann constant, T is the temperature and A is the targeted quantity. In fact, it is impossible to obtain the real ensemble average because it is extremely difficult to capture all the possible states over the entire phase space within a finite time period. In the MD simulations, time average is often calculated with an approximation:

$$\langle A \rangle = \lim_{\tau \to \infty} \frac{1}{\tau} \int_{t=0}^{\tau} A(t) dt \approx \frac{1}{N} \sum_{n=1}^{N} A(n), \tag{2-2}$$

where τ is the simulation time, $A(t)$ is the instantaneous value of A at certain time point and N is the number of time steps, and. Base on the ergodic hypothesis, the time average of MD simulations can be considered an approximation of ensemble average if the MD is run long enough so that the system effectively explores all possible states. In this regard, MD simulations should be run for a quite long time to obtain sufficient samplings for data analysis.

2.3 MD simulations

MD simulation is a computational method allowing for the prediction of time evolution of an interacting system involving the generation of atomic trajectories of a system. The forces between the particles and their potential energies are often calculated using interatomic potentials known as the force fields. In typical MD, the forces $\boldsymbol{F}$ on the ith atom can be calculated by taking the derivative of given the potential function U

$$\boldsymbol{F}_i = -\nabla_{\boldsymbol{r}_i} U \,, \tag{2-3}$$

where $\boldsymbol{r}_i$ is the position vector of the ith atom. The motion of all particles can be obtained by numerically solving of the Newtonian equations of motions. In this dissertation, the MD simulations were mainly integrated using the leap-frog algorithm [68]. Leapfrog integration is equivalent to updating positions and velocities at interleaved time points, staggered in such a way that they "leapfrog" over each other. A simple expression is given below to explain how it works for solving the motion equation to get the updated atom position and velocity and at different time:

$$\boldsymbol{r}_i(t+\Delta t) = \boldsymbol{r}_i(t) + \boldsymbol{v}_i(t)\Delta t + \frac{1}{2}\frac{\boldsymbol{F}_i(t)}{m_i}\Delta t^2 \tag{2-4}$$

$$\boldsymbol{v}_i(t+\Delta t) = \boldsymbol{v}_i(t) + \frac{\boldsymbol{F}_i(t) + \boldsymbol{F}_i(t+\Delta t)}{2m_i}\Delta t \tag{2-5}$$

The trajectories recording the information of the position coordinates for each atom at different time are saved and analyzed by statistical mechanics theory to obtain equilibrated and transport properties. The typical procedure of running a MD simulation is described in **Figure 2.1**.

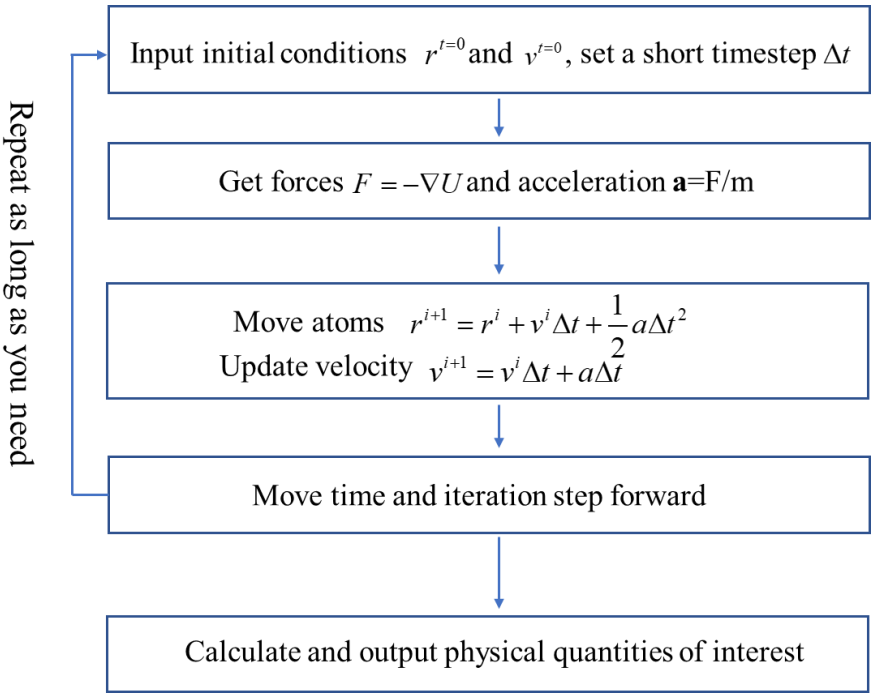

Figure 2.1 Schematic of molecular dynamic simulation procedure.

2.4 MC simulations

Monte Carlo Methods [69] are stochastic techniques that use random numbers to sample conformation space. A Monte Carlo simulation starts from a given conformation; then random numbers will generate a new trial conformation. This trial conformation will be determined whether to be accepted or rejected [70]. If it is accepted, this conformation will become the current conformation and the next iteration will start from this conformation. Sampling of phase space is achieved through a variety of trial moves, such as displacement, and molecule insertion and deletion. Because Grand Canonical Monte Carlo (GCMC) allows for the simulation of an open system, it has been used extensively to study the adsorption of gases in porous materials [71-74]. In the GCMC simulation, temperature, volume, and chemical potential of the system is kept fixed, while the number of particles is allowed to fluctuate through the steps of insertion and deletion [67]. The method considers the simulation box as being coupled with an infinite thermodynamic reservoir. At equilibrium, the simulation box system has the same temperature and chemical

potential is equal to that of the reservoir. Similar to MD simulations, the accurate force field is also needed for GCMC simulations to describe the interaction potential between various atoms.

The greatest challenge with GCMC simulations is how to achieve a sufficient number of accepted molecular insertion/deletion moves to ensure adequate sampling of phase space. The trial operations of the guest molecules in the nanopores become increasingly unlikely to satisfy the acceptance criteria when the molecular size increases as there is a far higher probability that part of the guest molecule will overlap unfavorably with the pore surfaces. The configurational-biased Monte Carlo method [75] was developed to improve the acceptance rate for molecule insertions and deletion which is also adopted in this project. Instead of randomly inserting molecules into the host, the guest molecule is "grown" atom by atom within the host in a way that avoids unfavorable overlap with the surface atoms. This growth procedure introduces a bias which should be compensated by considering a weight factor for each new position chosen (or a product of these factors for a new chain). A similar weight corresponding to reconstructing the old configuration from the new one has also to be calculated. The probability ratios are corrected by introducing the ratio between the new and the old configurational weight factors.

2.5 Force Field

The force field typically consist of bonded interaction parameters and non-bonded interaction parameters. In details, bonded interactions involve with bond stretching, angle bending, and proper dihedrals. The bond stretching between two covalent atoms i and j is usually represented by a harmonic potential:

$$V_b = \frac{1}{2} k_{ij}^b (r_{ij} - b_{ij})^2 , \tag{2-6}$$

Where k_{ij}^b is the force constant, kJ/(mol·nm2); r_{ij} and b_{ij} are, respectively, the bond length and

the balanced bond length between atoms i and j, nm.

The bond-angle vibration between a triplet of atoms $i-j-k$ can also be described by harmonic potential:

$$V_a(\theta_{ijk}) = \frac{1}{2} k_{ijk}^{\theta} (\theta_{ijk} - \theta_{ijk})^2 , \tag{2-7}$$

where k_{ijk}^{θ} is the force constant, kJ/(mol·rad2); θ_{ijk} and θ_{ijk}^{0} are the angle and equilibrated angle formed by atoms *i*, *j*, *k* in sequence, where atom *j* is in the middle, and *i* and *k* are at the ends, with the unit as degree.

The proper dihedral potential is given as the first four cosine terms of a Fourier series

$$V_d(\phi_{ijkl}) = c_1[1+\cos\phi] + c_2[1-\cos(2\phi)] + c_3[1+\cos(3\phi)] + c_4[1-\cos(4\phi)] , \tag{2-8}$$

where c_1, c_2, c_3, and c_4 are constants, kJ/mol; ϕ is the dihedral angle formed by atoms *i*, *j*, *k*, and *l*.

The interactions between atoms are modeled as pairwise additive potentials including coulomb potentials and Lennard-Jones (LJ) 12-6 potential,

$$V\left(r_{ij}\right) = 4\varepsilon_{ij}\left[\left(\frac{\sigma_{ij}}{r_{ij}}\right)^{12} - \left(\frac{\sigma_{ij}}{r_{ij}}\right)^{6}\right] + \frac{q_i q_j}{4\pi\varepsilon_0 r_{ij}} , \tag{2-9}$$

Where r_{ij}, σ_{ij}, and ε_{ij}, q_i are the separation distance, LJ well depth, and LJ size, the partial charge of atom i, respectively. The Lorentz-Berthelot mixing rule [76] is used to calculate interactions between atoms with different LJ parameters.

2.6 Important parameters for analysis

2.6.1 Radial Distribution Function

The radial distribution function (RDF) $g(r)$ is used to describe the probability to find an atom in a shell dr at the distance r of another atom selected as the reference point [77, 78]. The basic calculation procedure of RDF can be summarized as follows:

1). Select one atom as refence point (red point) and divide the system volume into spherical shells with a radius of dr as shown in **Figure 2.2**;

2). Count the number of atoms $dn(r)$ at a distance between r and $r+dr$ with respect to the reference atom;

3). Based on the relationship between $dn(r)$ and $g(r)$, it is easy to get the following equation

$$dn(r) = \frac{4}{3}\pi[(r+dr)^3 - r^3] \times \frac{N}{V} \times g(r), \tag{2-10}$$

where N represents the total number of atoms, V is the system volume, then we can obtain the formula of $g(r)$ according to eq (2-10)

$$g(r) = \frac{\frac{4}{3}\pi[(r+dr)^3 - r^3] \times \frac{N}{V}}{dn(r)}, \tag{2-11}$$

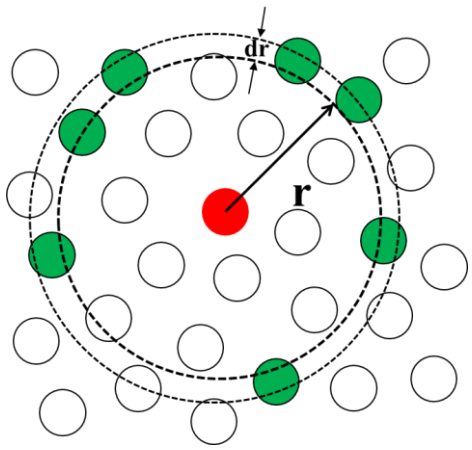

Figure 2.2 Space discretization for the calculation of the radial distribution function

2.6.2 Potential Mean Force

Free energy is an important parameter characterizing various chemical or physical processes. The change in free energy governs the directionality and extent of binding and unbinding kinetics. Potential of mean force (PMF) calculation method has long been used to explore how a system's energy changes as a function of some specific reaction coordinate which can be a geometrical coordinate or a more general energetic (solvent) coordinate [79, 80].

Take the canonical ensemble for example, the Helmholtz free energy F is given as

$$F = -k_B T \times \ln(Z_{can}), \tag{2-12}$$

where Z_{can} is the configurational partition function and it can be calculated as

$$Z_{can} = \int e^{-\frac{U}{k_B T}} d\boldsymbol{r}, \tag{2-13}$$

where U is potential energy of the system, k_B is Boltzmann constant, and T denotes the temperature. If we define a reaction coordinate as x, the probability distribution of the system along x is

$$P(x) = \frac{\int \delta(x - x(\boldsymbol{r})) e^{-\frac{U}{k_B T}} d\boldsymbol{r}}{e^{-\frac{U}{k_B T}} d\boldsymbol{r}}, \tag{2-14}$$

$\delta(x - x(\boldsymbol{r}))$ will always give a value of zero except when $x = x(\boldsymbol{r})$. The PMF potential $W(x)$ can be obtained from $P(x)$

$$W(x) = -k_B T \ln P(x), \tag{2-15}$$

when sampling over the configurational space, the system prefers to stay in the states with low potential energy resulting in poor sampling. As a result, PMF simulations are usually used in

conjunction with umbrella sampling, because typically the PMF simulation will fail to adequately sample the system space as it proceeds.

Umbrella sampling method is used to improve sampling of a system where ergodicity is hindered by the form of the system's energy landscape, which is first proposed by Torrie and Valleau in 1977 [80]. It is one of the most widely used approaches to overcome free energy barriers in free energy calculation. In a general umbrella sampling scheme, multiple windows were set with initial structures with different reaction coordinate values. A bias potential is applied to each window according to a harmonic bias function or an adaptive bias function. The potential energy U of a biased system is given as:

$$U_{\text{bias}} = U_0 + \omega_i(x), \tag{2-16}$$

where U_0 is the potential energy of the unbiased system, $\omega_i(x)$ is the added bias potential at *i*th window. The unbiased distribution of the reaction coordinate can be obtained as:

$$P_i^u(x) = \frac{\int \delta(x - x(\boldsymbol{r}))e^{-\frac{U_{bias}}{k_B T}} d\boldsymbol{r}}{e^{-\frac{U_{bias}}{k_B T}} d\boldsymbol{r}}, \tag{2-17}$$

Furthermore, the unbiased probability could be determined by:

$$P_i^u(x) = P_i^b(x)\exp[\beta\omega_i(x)]\exp[-\beta\omega_i(x)], \tag{2-18}$$

From the simulation in each window, the biased probability $P_i^b(x)$ is known, and the free energy of the window thus could be induced by:

$$U_0 = -\frac{1}{\beta}\ln P_i^b(x) - \omega_i(x) + F_i, \tag{2-19}$$

where F_i is a constant which could be solved by self-iteration until a convergence is reached [81].

Chaper 3 CO_2 Adsorption in Partially Water-Saturated Kaolinite Nanopores from Molecular Perspectives in Relation to Carbon Geological Sequestration

Abstract

Continuously growing atmospheric CO_2 concentration has caused a series of environmental problems. CO_2 geological sequestration in depleted gas and oil reservoirs is regarded as a promising strategy to mitigate the emission of CO_2 thanks to the well-developed nanoscale pore structures providing substantial available adsorption spaces. Therefore, the fundamental understanding and knowledge about CO_2 adsorption in shale nanopores can provide important insights into CO_2 sequestration in shale formations. In this work, we used molecular dynamic (MD) and Grand canonical Monte Carlo (GCMC) simulations to investigate the CO_2 adsorption in two kinds of kaolinite nanopores with different basal surfaces and evaluate the effects of the connate water. In the absence of water, CO_2 presents a stronger adsorption ability on gibbsite surfaces indicating a higher CO_2 sequestration capacity in gibbsite pores. In gibbsite pores, the water tends to spread out on the surface forming a thin film that largely screens the CO_2 adsorption on the kaolinite surface. While CO_2 is driven to the middle of the pore, an enrichment of CO_2 is observed at the water-CO_2 interface. Water bridges are observed in siloxane pores due to the significant reduction of H-bonding between water and kaolinite surfaces. In mesopores, the shape of water clusters gradually turns to be spherical ones as pressure increases suggesting a more CO_2-wet surface, while the deformation of water in micropores is not obvious because of stronger confinement effects. The CO_2 distributions are divided into six regions based on the counter map density and we found that the highest CO_2 density appears in the three-phase contact areas and

CO_2 has a high tendency to accumulate in two-phase regions. In general, the presence of water will result in the reduction of CO_2 sequestration in both gibbsite and siloxane pores, while a slight enhancement is observed in siloxane mesopores when the pressure is quite low. Overall, the connate water has a more detrimental influence on CO_2 sequestration in gibbsite pores. Our work should provide important insights into CO_2 adsorption in kaolinite nanopores and reveal the CO_2 sequestration mechanisms in the presence of connate water.

3.1 Introduction

As the major greenhouse gas (GHG), CO_2 emission has attracted widespread attention worldwide in the recent decade [2, 82, 83]. Atmospheric CO_2 concentration has increased gradually since the industrial revolution from ~280 ppm [3, 84] to ~420 ppm [4] by 2022, resulting in severe greenhouse effects which adversely impact the global climate [85, 86] and natural ecosystem [87]. Consequently, it is vital to mitigate CO_2 emissions. Carbon capture and storage (CCS) [9-11] is widely regarded as a very promising strategy to control CO_2 emission, in which CO_2 is captured and then transported to appropriate storage sites for permanent sequestration [20, 88]. The depleted shale oil/gas reservoirs [88-90] are one of the primary target storage sites for geological CO_2 sequestration (GCS) thanks to the well-developed nanoporous structures with extremely low permeability [91, 92] in which CO_2 has a substantial adsorption capacity. In addition, CO_2 sequestration in shale reservoirs holds distinct advantages in terms of economic profits thanks to the enhanced oil/gas recovery [10, 88, 93] compared to other geological sequestration sites such as deep saline aquifers, deep coal seams, and salt caverns [20, 94].

Shale rocks typically consist of organic and inorganic matters which contain a considerable number of nano-scale pores with their sizes ranging from several to hundreds of angstroms [95-97]. Organic matters mainly refer to kerogen [98], while clay minerals account for most of the

inorganic matters. On the other hand, connate water can exist in the shale formations, occupying 10% to 30% of the total pore volume [28, 29]. As a typical clay mineral in shale media [99, 100], kaolinite exhibits two structurally and chemically distinct basal surfaces known as siloxane and gibbsite surfaces [31, 101]. The siloxane surface is relatively hydrophobic, while the gibbsite one is hydrophilic [32, 101, 102]. The distinct surface properties result in drastically-different interfacial phenomena [103], which can significantly affect CO_2 adsorption in kaolinite nanopores, especially in the presence of water. Therefore, the fundamental understanding and knowledge about CO_2 adsorption and the moisture effect in different kaolinite nanopores can provide important insights into GCS in depleted shale formations.

Several experimental measurements have been carried out on CO_2 adsorption in kaolinite. Heller *et al*. [104] measured CO_2 adsorption isotherms at 313 K in illite and kaolinite samples. The reported CO_2 adsorption isotherm can be described by the Langmuir model, while kaolinite has a higher adsorption capacity than illite. Chen *et al*. [105] evaluated the CO_2 adsorption capacity in kaolinite using a thermogravimetric analyzer and concluded that kaolinite can be considered a potential adsorbent for CO_2 capture. Du *et al*. [106] conducted isothermal adsorption of pure CO_2, N_2, and CH_4 in kaolinite clay. They found that the uptakes of these three gases all decrease monotonically with temperature, and the order of the adsorption capacity is $N_2<CH_4<CO_2$. Nevertheless, due to the complicated surface properties and pore structures, it is practically impossible to distinguish the contributions from two distinct kaolinite surfaces. In addition, while the presence of water plays an important role in regulating CO_2 adsorption in clay minerals [52, 106-108], to the best of our knowledge, the effect of moisture on CO_2 adsorption in kaolinite has been rarely reported from experimental perspectives.

On the other hand, molecular simulations can explore CO_2 adsorption behaviors from a molecular scale, explicitly considering specific mineral surfaces and moisture content [32, 95, 101, 103, 108]. A number of molecular simulation studies [109-113] have been reported on the CO_2-CH_4 competitive adsorption in kaolinite nanopores, finding that CO_2 has a much stronger adsorption capability than CH_4 which is favorable for the enhanced gas recovery. While these studies provide some insights into CO_2 adsorption in kaolinite, they typically use one kaolinite basal surface (either siloxane or gibbsite) and do not systematically elaborate on the effect of specific basal surface types. On the other hand, Lainé *et al*. [114] performed density functional theory (DFT) calculations to compare the interaction energy of kaolinite surfaces with pure CO_2 and H_2O. They reported that the adsorption energy of water is lower than that of CO_2. In addition, Xiong *et al*. [33] and Hao *et al*. [34] reported that water in partially water-saturated clay nanopores can form either thin film on the surfaces or bridge depending on surface properties which can greatly influence gas-water coexistence and hydrocarbon transport behaviors. Nevertheless, how water structures in partially water-saturated kaolinite pores affect CO_2 adsorption remains unanswered.

In this work, we use grand-canonical Monte Carlo (GCMC) and molecular dynamics (MD) simulations to investigate CO_2 adsorption in partially water-saturated kaolinite slit pores with two distinct basal surfaces at 333.15 K. We find that without water, CO_2 adsorption layer is stronger on gibbsite surface than that on siloxane surface, suggesting that more CO_2 can be adsorbed in gibbsite kaolinite nanopores. In gibbsite kaolinite nanopores, water is spread over the surface thanks to the formation of hydrogen-bonding (H-bonding) between water and surface -OH groups, forming thin water films. As a result, while CO_2 molecules fill in the middle of the pore, they can accumulate at water-CO_2 interfaces. On the other hand, in siloxane kaolinite nanopores, thanks to

the weaker water-surface interaction, water forms bridges. The highest CO_2 density takes place at the liquid-gas-solid (water-CO_2-kaolinite) contact areas, and it has a strong tendency to accumulate at the solid-gas (kaolinite-CO_2) and liquid-gas (H_2O-CO_2) interfaces. Generally, CO_2 adsorption in both kaolinite nanopores is reduced in the presence of water, while moisture has a more adverse impact in gibbsite kaolinite pores. Collectively, our work provides some important insights into CO_2 adsorption behaviors in partially water-saturated kaolinite nanopores in relation to GCS in depleted shale gas/oil formations.

The rest of this paper is organized as follows. In **Section 3.2**, we introduce the molecular model and force fields. We also present the simulation methods. In **Section 3.3**, CO_2 adsorption in partially water-saturated siloxane and gibbsite kaolinite nanopores are analyzed. In **Section 3.4**, the potential implications and key findings are summarized.

3.2 Molecular Model and Simulations

3.2.1 Molecular Models

Kaolinite models are created according to Bish [30] by cleaving along with the (0 0 1) plane. Kaolinite is a 1:1 type of aluminosilicate clay consisting of one Al-O octahedral sheet and one Si-O tetrahedral sheet with the unit cell formula of $Al_2Si_2O_5(OH)_4$. The unit cell of kaolinite has the following lattice parameters as a = 0.51535 nm, b = 0.89419 nm, c = 0.73906 nm, α = 91.926°, β = 105.046°, and γ = 89.797°. Each kaolinite model is constructed by 12 × 6 × 1 unit cell, resulting in a clay patch of ~6.18 nm × 5.65 nm ($L_x \times L_y$) in the *x*-*y* dimension with a thickness of 0.739 nm in the *z*-direction. Then, two clay layers are stacked parallelly to build two distinct slit-like kaolinite pores (gibbsite and siloxane) with the Al-O or Si-O plane facing each other as shown in **Figure 3.1**. To see whether the number of clay layers has a significant influence on the adsorption behaviors, we also test the cases using two-layer clay patches as the kaolinite surfaces

and compare with the single-layer model as shown in **Figure A.1**. We find that CO_2 and water distributions are generally independent of the number of clay layers. The pore size of kaolinite slit pores is defined as the shortest vertical distance between the innermost surface O atoms. It is well-known that micropores (*i.e.*, pore size less than 2 nm) and mesopores (*i.e.*, pore size between 2 nm and 50 nm) [115] dominate in shale formations [96, 109]. Thus, in this work, we design two pore sizes (2 nm and 4 nm). To explore the moisture effect on CO_2 adsorption, we adopt a water concentration of 0.2 g/cm^3 (corresponding to 880 and 440 water molecules in mesopores and micropores, respectively) which is within the water saturation range in shale reservoirs [116, 117].

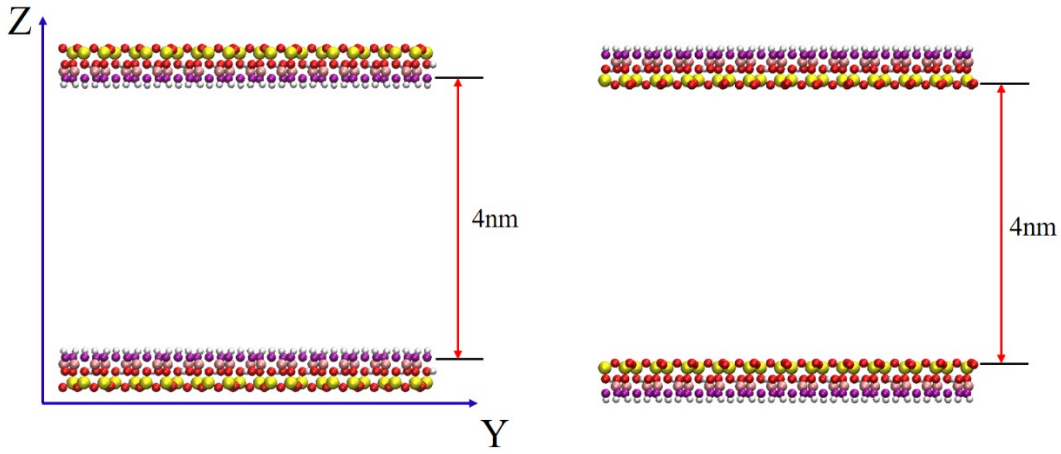

(a) (b)

Figure 3.1 Kaolinite (a) gibbsite; (b) siloxane nanopores with a pore size of 4 nm. Color scheme: pink, Al; yellow, Si; purple, O in surface -OH groups; red, other O atoms.

We use the CLAYFF force field [118] to describe kaolinite which has been widely used to study gas adsorption [95, 107, 109, 112] in clay and water-clay interfaces [103, 118, 119]. We use the flexible three-point SPC model to simulate water, as CLAYFF is optimized with SPC [118, 120]. While most simulation works on gas adsorption use the rigid clay model [107-109], CLAYFF is a flexible model allowing atoms to move freely, and the -OH group is described by a

simple harmonic term. Therefore, in this work, we adopt a flexible kaolinite model by considering the stretching potential of surface -OH groups. In addition, to avoid undesirable translation and rotation of the clay layer, the middle Al atoms are frozen while all other atoms are allowed to move without any restrictions. The rigid TraPPE force field [121] is applied to describe CO_2 molecules. The combination of TraPPE CO_2 and CLAYFF has shown excellent performance in terms of CO_2 adsorption behaviors in various clay nanopores [95, 122]. The Lorentz-Berthelot mixing rules [123] are employed to calculate the interactions between non-bonded atoms. The non-bonded interactions are represented by pairwise Coulomb potential and Lennard-Jones (LJ) potential which are truncated at a distance of 12 Å with the tail correction. The long-range electrostatic potential is computed using the PPPM methods [124] with a precision value of 10^{-4}. Three-dimensional (3-D) periodic boundary conditions are applied in all the simulations. To avoid the influence of the periodic images in the *z*-direction, a vacuum space is placed with a length much larger than L_x or L_y.

3.2.2 Simulation Details

Two distinct simulation scenarios are designed in this work: **Scenario I** represents CO_2 adsorption in kaolinite nanopores without water; **Scenario II** represents CO_2 adsorption in kaolinite nanopores with pre-adsorbed water. **Scenario I** is conducted with the GCMC simulation using MCCCS Towhee software [125]. The chemical potentials of CO_2 under various pressure conditions are obtained by Widom's insertion method [126] based on the bulk CO_2 phase in the *NVT* ensemble. During GCMC simulations, insertion/deletion, rotation, and translation are implemented for CO_2, while for kaolinite only translational moves are applied except for Al atoms which remain fixed all the time. 20000 MC cycles per CO_2 molecule are carried out to achieve equilibrium and 50000 MC cycles are conducted for sampling. In **Scenario II**, due to the low

acceptance ratio of MC moves for water [127, 128], water molecules are first randomly placed in kaolinite nanopores which are equilibrated by a subsequent 20-ns MD simulation in the *NVT* ensemble (performed in GROMACS software (version 2019.6) [129]) to obtain the initial water configurations. Then, GCMC simulations are conducted with the same MC moves for CO_2 and kaolinite as adopted in **Scenario I**. On the other hand, we only apply transitional and rotational moves to water molecules as in the previous works [108, 130]. In other words, we assume that water molecules are not displaced out of kaolinite nanopores during CO_2 adsorption. 50,000 MC cycles per fluid molecule are carried out for each pressure condition with the last 10,000 MC cycles used to obtain the average number of CO_2 molecules, $N_{CO_2}^{ave}$. Then, we perform 20-ns MD simulations for water-CO_2 mixtures in the *NVT* ensemble with the number of CO_2 molecules as $N_{CO_2}^{ave}$ to achieve equilibrium followed by 40-ns production runs for data analysis. The temperature in MD simulations is controlled by using the Nośe−Hoover thermostat algorithm [131], which is set as 333.15 K for all the simulations. All snapshots are visualized by visual molecular dynamics (VMD) software [132].

3.3 Results and discussion

In this section, we first analyze CO_2 density distributions in two different kaolinite nanopores in the absence of water (**Scenario I**). Then, CO_2 adsorption behaviors in partially water-saturated kaolinite nanopores are presented (**Scenario II**).

3.3.1 Scenario I: CO_2 Adsorption in Kaolinite Nanopores without Water

The CO_2 density profiles along the *z*-direction without water in gibbsite and siloxane kaolinite mesopores (4 nm) under different pressure conditions are presented in **Figure 3.2.** While CO_2 can form strong adsorption layers in both pores, the peaks of the first adsorption layer in gibbsite pores are more prominent than those in siloxane pores. The differences are more

pronounced at low pressures. Similar results are also observed in micropores as shown in **Figure A.2**. In addition, we also compare the results to those from the rigid clay models in which all kaolinite atoms are kept frozen as shown in **Figure A.3.** In siloxane kaolinite nanopores, the CO_2 density profiles from flexible and rigid models are comparable, while the rigid model underestimates the CO_2 adsorption layer in gibbsite kaolinite nanopores. As discussed in **Section 2.2**, the CLAYFF force field is developed as a flexible model [118], which can reflect a more realistic clay surface. Our study indicates that the flexible and rigid models might result in different gas adsorption behaviors for certain cases.

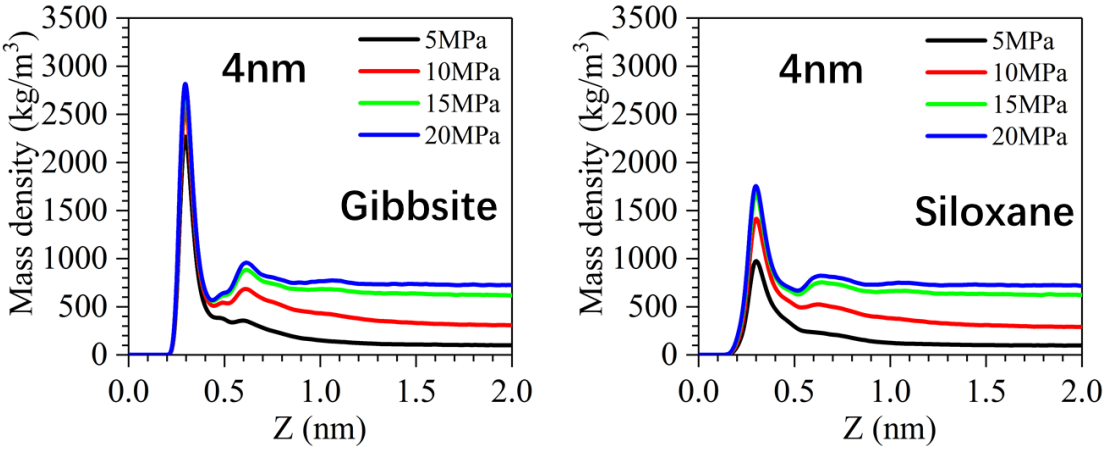

(a) (b)

Figure 3.2 CO_2 density profiles in (a) gibbsite; (b) siloxane kaolinite mesopores under different pressure conditions and 333.15 K.

3.3.2 Scenario II: CO_2 Adsorption in Kaolinite Nanopores with Water

3.3.2.1 Gibbsite Kaolinite Nanopores

In **Figure 3.3**, we present the schematic representations of CO_2 and water molecular configurations in gibbsite kaolinite mesopores and micropores at 5 MPa and 333.15 K. Water tends to spread over the gibbsite surfaces to form water films due to strong H-bonding interaction with surface -OH groups [133], which is in line with the previous simulation findings [108, 130]. In

mesopores, water molecules completely occupy the surface region, while some areas remain exposed to CO_2 in micropores. It is probably because there are more water molecules in mesopores than in micropores with the same cross-sectional surface areas ($L_x \times L_y$). CO_2 and water molecules have similar distributions at higher pressures as depicted in **Figure A.4** and **Figure A.5**. To better understand CO_2 and water distributions, we present their density profiles along the *z*-direction in gibbsite kaolinite nanopores in **Figure 3.4**. In mesopores, water dominates the surface region repelling CO_2 from the surface to the middle of the pores which corresponds to the complete coverage of water films shown in **Figure 3.3(c)**. On the other hand, CO_2 molecules accumulate at the water-CO_2 interface thanks to strong water-CO_2 interaction, which is in line with the previous studies [108, 134, 135]. In micropores, as water cannot fully cover the entire surface, CO_2 can adsorb on the surfaces where there is no water film as shown in **Figure 3.3(d)**.

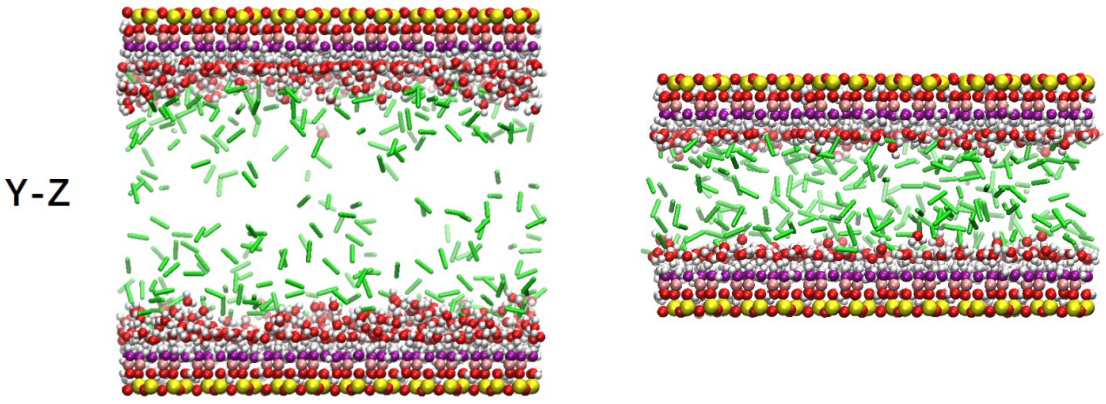

(a) (b)

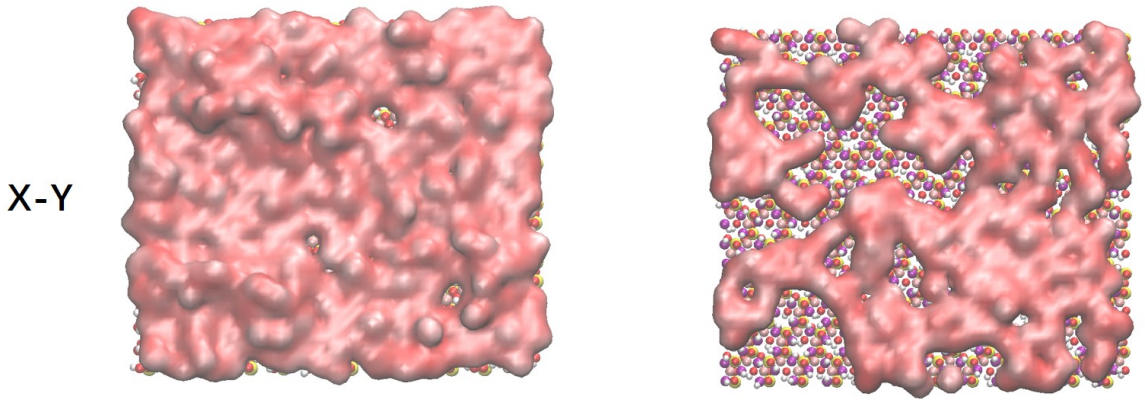

(c) (d)

Figure 3.3 Schematic representations of CO_2 and water molecular configurations in gibbsite kaolinite (a) mesopores; (b) micropores at 5 MPa and 333.15 K from the *y-z* plane view. Water distribution pattern on gibbsite surfaces from the *x-y* plane view in (c) mesopores; (d) micropores. For a better view, water molecules are presented in a quick-surf mode in VMD.

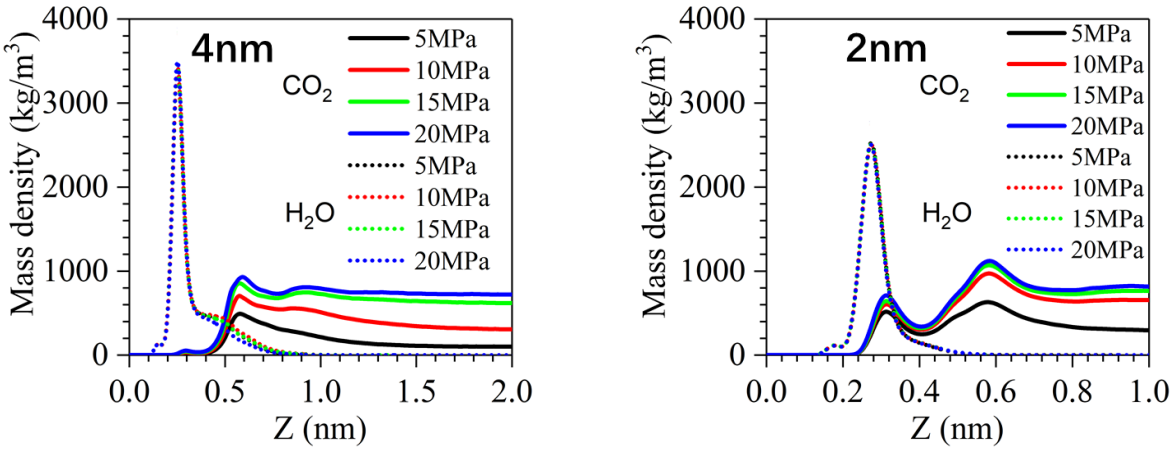

Figure 3.4 CO_2 and water density profile in gibbsite kaolinite (a) mesopores; (b) micropores under different pressure conditions and 333.15 K with a water concentration of 0.2 g/cm^3.

3.3.2.2 Siloxane Kaolinite Nanopores

The schematic representations of CO_2 and water molecular configurations in siloxane kaolinite mesopores and micropores at 5 MPa and 333.15 K are shown in **Figure 3.5**. In contrast to **Figure 3.3**, water and CO_2 molecules exhibit drastically different configurations in siloxane

kaolinite nanopores. Water film is no longer observed in siloxane nanopores, while water bridges form instead. The water bridges have a cylindrical symmetry according to the *y*-*z* and *x*-*y* plane views. The formation of water bridges is also reported in the previous works [33, 34], while they argued that it is due to the electric field induced by different clay surface properties. We also calculated the electric field inside the siloxane nanopores (see **Figure A.6**) with the method used in Xiong's work [33] (see details in **A1**). It shows that the effective electric field zone (> 1V/nm) [33] only influences the water within 0.6nm of the surface while it is negligible in the middle of pores, which indicates that the directional-dependence water structure is not related to the electrical field. The distinct wettability properties of siloxane and gibbsite surfaces [32] might be one possible reason accounting for the different hydration states. It has been reported that gibbsite surfaces are quite hydrophilic with a water contact angle (CA) of less than 10° while the siloxane surfaces present strongly CO_2-wetting characteristics (water CA>140°) [32]. As a result, the water has a high tendency to spread over the gibbsite surfaces and form water films. While in siloxane nanopores, because the water is initially randomly distributed inside the pores, the water spontaneously assembles into spherical ones on both top and bottom surfaces to minimize the contact area with surfaces. During this process, the water droplets will encounter each other on both sides and are connected to form the unique water bridge structures. Once the water bridges are formed, it is difficult to transform into other conformations due to free energy barriers. The detailed discussion of local energy minimum for water bridges and energy barrier required from water bridge to an intermediate state is provided in **A2.** Furthermore, we also tried another initial configuration by placing water on one side of the nanopores and finally the water clusters evolve into the shape of semi-cylinder as shown in **Figure A. 7**. However, this work mainly targets on the

water bridge structure and the initial configuration effects on water structure will be discussed in future work.

Additionally, we found that the shape of water clusters gradually transforms from the cylinder (at 5 MPa in **Figure 3.5(a)**) into the sphere frustum as pressure increases (see **Figure A.8)** indicating that kaolinite surfaces become more CO_2 wet. The dependence of surface wettability on CO_2 pressure is also reported by Zhou *et al*. [136] and *Pan et al*.[137]. On the other hand, the deformation of water bridges is not obvious in micropores (see **Figure A.9**). It is probably because the water in micropores has a stronger interaction with the kaolinite surface due to stronger confinement effects [138-140] which are in accordance with the higher H-bonding numbers in micropores (see **Table 3.1**). In this work, the hydrogen bonds are identified using a geometrical criterion, according to which a hydrogen bond is determined if r O···H< 3.5 Å and ∠O···O−H ≤ 30° [133].

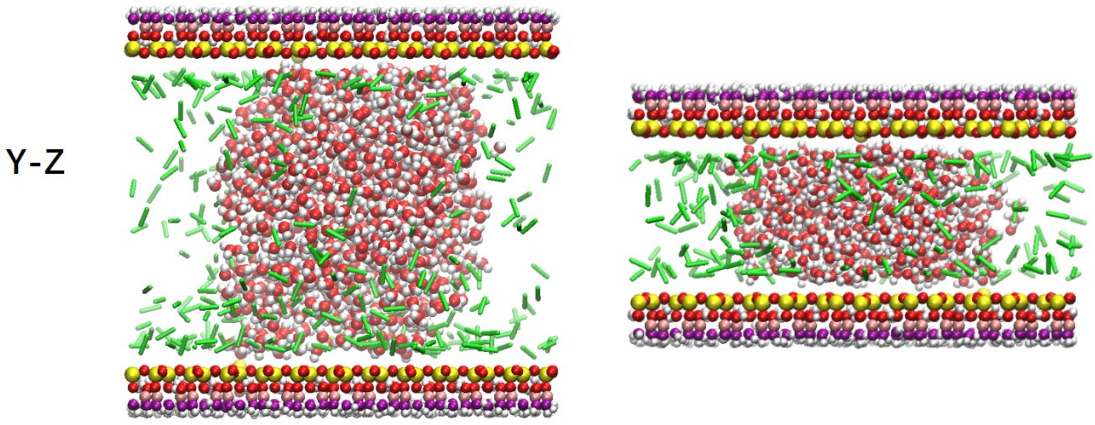

(a) (b)

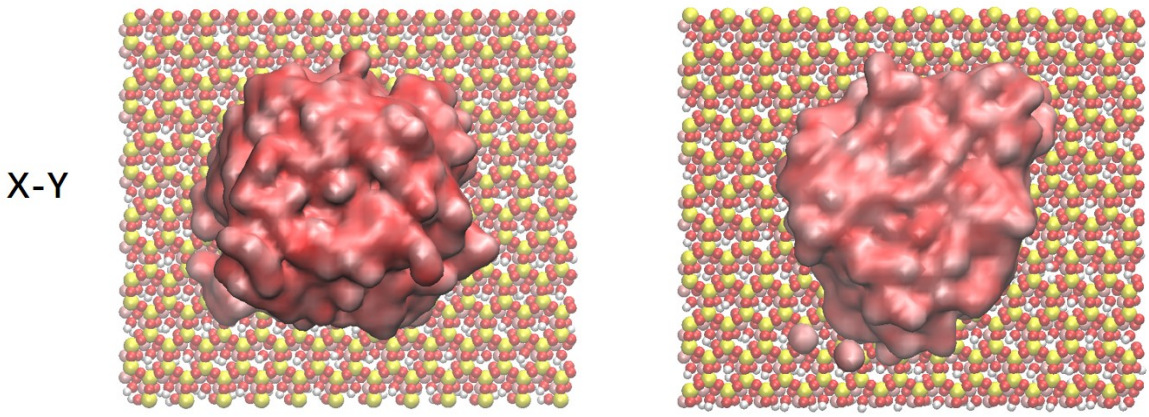

(c) (d)

Figure 3.5 Schematic representations of CO_2 and water molecular configurations in siloxane kaolinite (a) mesopores; (b) micropores at 5 MPa and 333.15 K from the *y*-*z* plane view. Water distribution pattern on siloxane surfaces from the *x*-*y* plane view in (c) mesopores; (d) micropores. For a better view, water molecules are presented in a quick-surf mode in VMD.

Table 3.1 H-bonding number between water and kaolinite surfaces under various pressure conditions and 333.15 K.

H-bonding Number	5 MPa	10 MPa	15 MPa	20 MPa
Siloxane Mesopore	12.3	11.6	9.2	8.6
Siloxane Micropore	18.3	16.1	14.8	14.9

Thanks to the cylindrical symmetry of water bridges, we present the two-dimensional (2D) density contour plots of CO_2 and water using the cylindrical coordinates in **Figure 3.6**. CO_2 distributions in the middle of pores and the near-surface regions (highlighted by red dotted line) can be divided into six different zones as shown in **Figure 3.6(a)**: Zone I (liquid phase), Zone II (liquid-gas contact area), Zone III (gas phase), Zone IV (liquid-solid contact area), Zone V (liquid-solid-gas contact area), and Zone VI (solid-gas contact area). The one-dimensional (1D) density profiles of CO_2 and water along the radius of the cylinder in the middle of pores ($1.75 \leq z \leq 2.25$

nm) and the near-surface regions ($0.2 \le z \le 0.4$ nm) at different pressure conditions are plotted in **Figure 3.7**. CO_2 density in Zone I is negligible as its solubility in water is small, while the highest CO_2 density value appears in Zone V. CO_2 has a strong adsorption layer in Zone VI with its density value higher than that in Zone II. The peak density values in Zone II and Zone VI are higher than the CO_2 bulk density (Zone III). Due to the competitive adsorption of water, the CO_2 density in Zone IV is lower than its bulk value (Zone III). As pressure increases, the CO_2 peak value difference between Zone II and Zone III, Zone V as well as Zone VI becomes less significant, which is in line with the previous observations [103, 136, 141]. In addition, the profile of the water droplet front (dashed black line) at the CO_2-water interface (see **Figure 3.6**) gradually turns to be a more spherical one when pressure increases from 5 MPa to 20 MPa, which is in line with the shift of water density profiles to the right side shown in **Figure 3.7(a)**. Here, the water front is defined as the position where the water density equals to 90% of the bulk water in Zone I.

To quantitatively illustrate the shape deformation, we calculate the shape factor $\lambda = R_s / R_m$ which is defined as the ratio between the radius of cross section for the water clusters close to surface (R_s) and in the middle of the pore (R_m) as listed in **Table A.1**. If λ equals to 1, the water clusters can be regarded to have a cylinder geometry and a larger λ value indicates the transformation of water front to the spherical ones. We find that λ in siloxane mesopores at 5 MPa is close to 1 indicating a roughly cylindrical geometry of water clusters while a more spherical front is observed at higher pressures. While similar phenomena are observed in micropores, the shape alteration of the CO_2-water interface is not obvious as shown in **Figure A.10** and **Table A.1**. Therefore, compared with the results in **Figure 3.7(a)**, water distribution only presents a minor shift to the right side in **Figure A.11(a).**

While Zhou *et al*. [74] argued that the CO_2 dissolution in water can account for up to 20% of total CO_2 adsorption amount in kerogen nanopores, our results show that the contribution of dissolved CO_2 in Zone I and IV is less than 2%. The differences can be mainly attributed to the different water contents and distribution patterns. They placed 0.451 g/cm^3 of water (0.2 g/cm^3 in our work) in kerogen pores which results in more dissolved CO_2 and water occupies more available pore spaces. In addition, the primary contribution of dissolved CO_2 in Zhou *et al*. [74] is from the water-solid surface region. In their work, the water clusters extend infinitely along one direction creating a broad water-solid surface. However, water bridges form in this work with limited contacting areas between water and kaolinite surfaces.

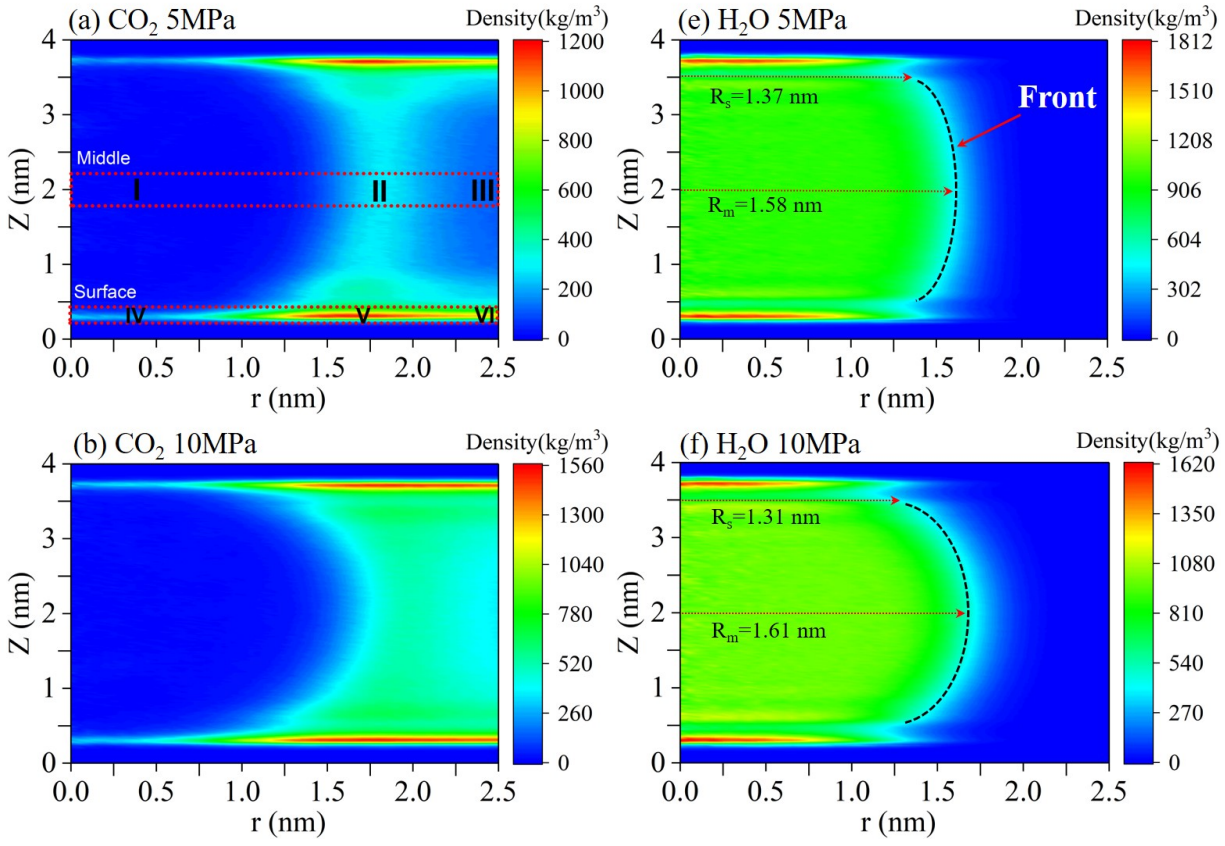

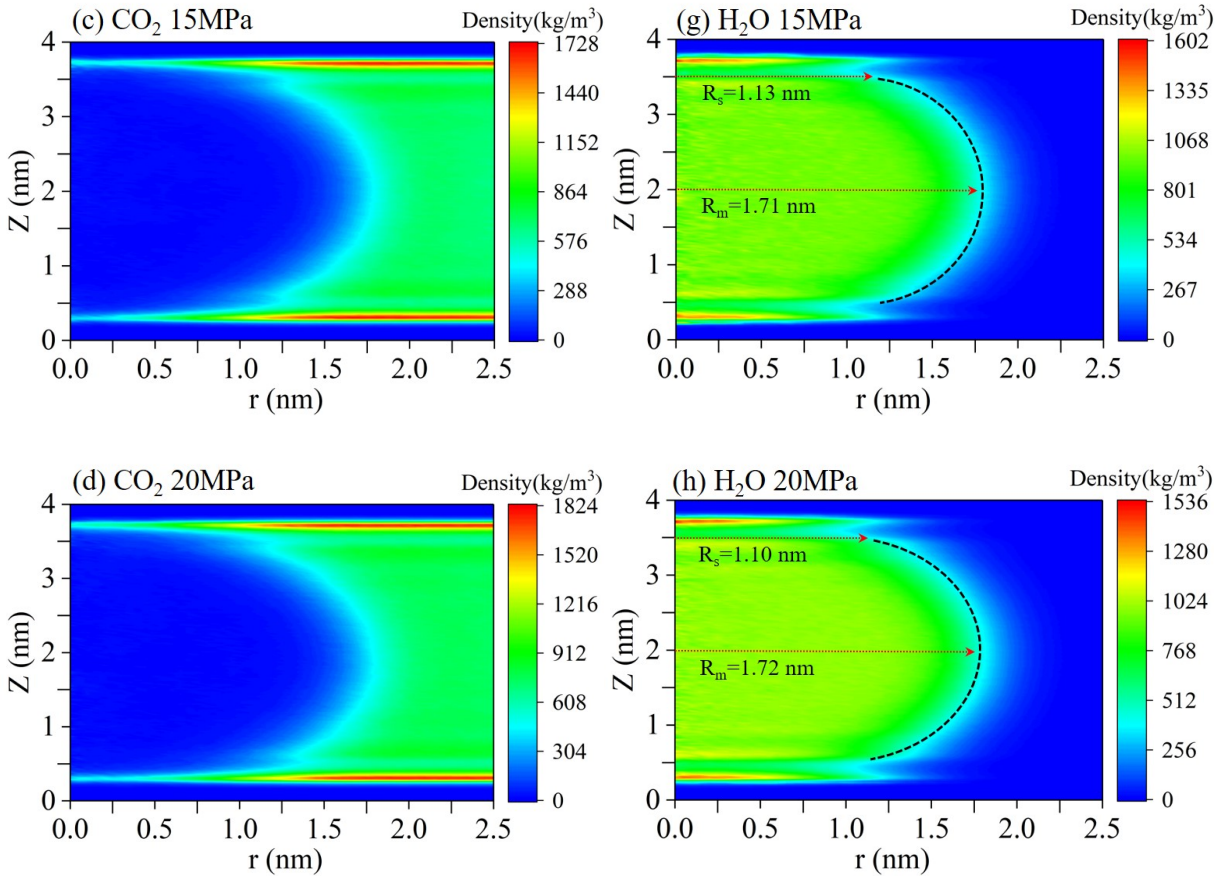

Figure 3.6. 2D density contour plots for CO_2 and H_2O using the cylindrical coordinate with the cylinder generatrix crossing the mass center of water clusters in kaolinite siloxane mesopores at different pressure conditions and 333.15 K. The black dashed lines represent the contour line with the water density equals to 90% of the bulk water. R_s and R_m denote the radius of cross section for the surface and middle part of the water clusters.

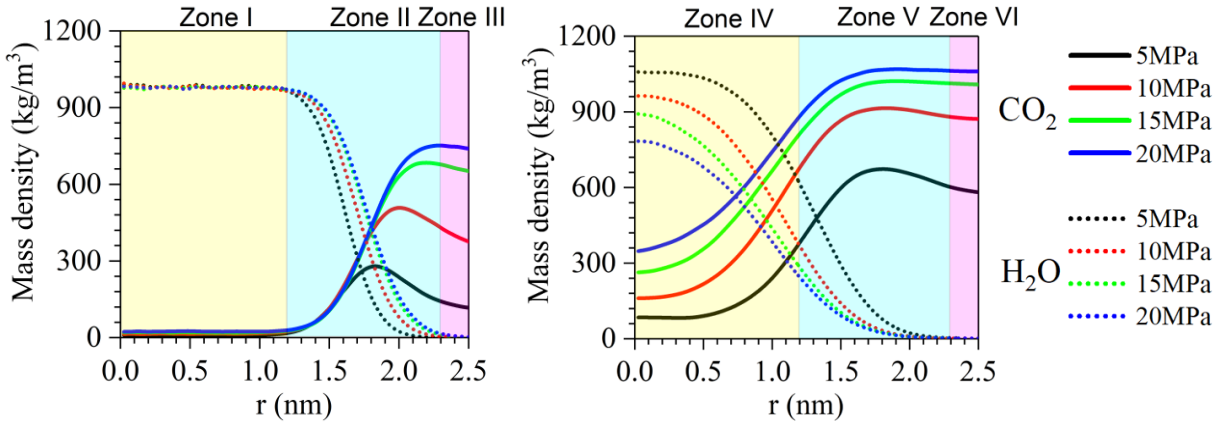

(a) (b)

Figure 3.7 1D density profile of CO_2 and water along the radius of cylinder in (a) the middle of pores; (b) the near-surface regions of siloxane mesopores at different pressure conditions and 333.15 K.

3.4 Implications for CO_2 storage

In the above sections, we elucidated CO_2 adsorption behaviors in different kaolinite nanopores. To provide a better insight into CO_2 sequestration, we presented the average densities of CO_2 in **Figure 3.8** which are defined as

$$\bar{\rho} = \frac{\langle N \rangle M}{L_x \times L_y \times w \times N_A}, \tag{3-1}$$

where $\langle N \rangle$ is the ensemble-averaged number of CO_2, M is the molecular weight of CO_2, L_x and L_y represents the length of box size in x and y direction, respectively, w is the pore height, and N_A is the Avogadro constant.

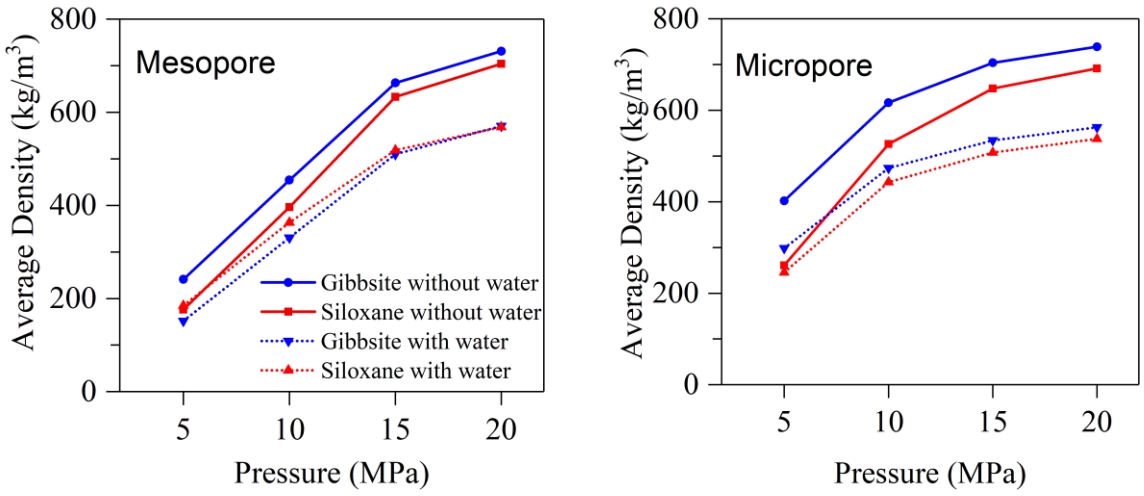

(a) (b)

Figure 3.8. Average density of CO_2 in kaolinite (a) mesopores and (b) micropores under various conditions.

In the absence of water, more CO_2 can be sequestrated in gibbsite nanopores (the blue line is over the red line) due to stronger surface adsorption which is already discussed in **Section 3.3.1**. The CO_2 storage amount difference in these two pores becomes smaller as pressure and pore size increase because the surface adsorption effect is weakened at high pressures and large pores. In mesopores, the existence of water leads to a higher CO_2 sequestration amount in siloxane pores than that in gibbsite pores (red dotted line is over the blue dotted line), while in micro-pores more CO_2 can be stored in gibbsite pores (blue dotted line is over the red dotted line).

To quantitively compare the moisture influences on the CO_2 sequestration in different kaolinite nanopores, the storage reduction efficiency η is plotted in **Figure 3.9** which is given as follows

$$\eta = \frac{\langle N_{cw=0.2}^{P_i} \rangle - \langle N_{cw=0}^{P_i} \rangle}{\langle N_{cw=0}^{P_i} \rangle} \times 100\%, \tag{3-2}$$

$\langle N_{cw=0.2}^{P_i} \rangle$ and $\langle N_{cw=0}^{P_i} \rangle$ represent ensemble-averaged CO_2 number in nanopores when the water concentration is 0.2 g/cm^3 and 0 g/cm^3 at different pressure conditions. The negative values mean that the CO_2 sequestrations are reduced while the positive ones indicate the enhancement of CO_2 storage.

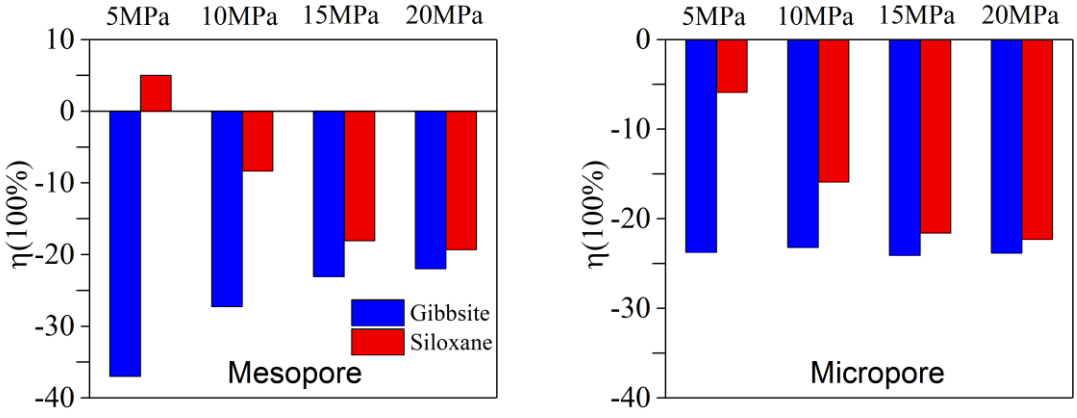

(a) (b)

Figure 3.9 The CO_2 storage reduction efficiency in kaolinite (a) mesopores and (b) micropores under various pressure conditions.

In gibbsite mesopores with water, CO_2 sequestration is reduced in the presence of water. The suppression is alleviated when pressure increases and finally tends to be leveling off. The reason is that water form films on the whole kaolinite surface mainly influencing the surface adsorption of CO_2 which contributes less to the total CO_2 storage amount when the pressure increases. In micropores, the influence of water on CO_2 sequestration is comparable to each other for different pressure conditions. The partial depletion of surface CO_2 and the second adsorption layer in **Figure 3.4(b)** might be responsible for the pressure-independent CO_2 storage reduction. Different from gibbsite pores, CO_2 sequestration reduction is more significant at higher pressures in siloxane pores. As we have mentioned in **Figure 3.7**, the CO_2 can form an adsorption layer in the gas-liquid interface and three-phase contact areas resulting in the surface excess of CO_2 which can compensate for the CO_2 sequestration loss arising from the reduction of available pore space due to water occupation. The increase of pressure leads to the reduction of surface excess of CO_2, thus the compensation effects become weaker at high pressures leading to more significant sequestration reduction. Interestingly, when the pressure is low (5MPa), the CO_2 sequestration is even slightly enhanced in gibbsite mesopores. The influence of pre-adsorbed water on the adsorption of CO_2 involves a competition between the effect of excluded volume by water and the H_2O-CO_2 interactions. At low pressure, the excluded volume effect is not marked thanks to low CO_2 density. As a result, the CO_2 adsorption is enhanced by the surface accumulation of CO_2 in Zone II and Zone V (see **Figure 3.7**) which is over the CO_2 storage loss. A similar phenomenon is also reported in previous simulation work when they studied the CO_2 adsorption in the presence

of water in single-walled carbon nanotubes [142]. Overall, the connate water has a more detrimental influence on CO_2 sequestration in gibbsite pores.

3.5 Summary

In this work, we used MD and GCMC simulations to explore CO_2 adsorption behaviors in dry and partially water-saturated kaolinite nanopores with two distinct basal surfaces. In the absence of water, a stronger CO_2 adsorption layer is observed on gibbsite surfaces which means that more CO_2 can be sequestrated in gibbsite pores. In gibbsite pores, water prefers to form a thin film covering the surfaces due to strong H-bonding interaction between water and surface -OH groups and drive CO_2 to the middle of pores. While CO_2 is depleted from the pore surfaces, it tends to accumulate at the water-CO_2 interface. Unlike the gibbsite pores, water bridges take place in siloxane pores thanks to the initial water configurations and local energy minimum. In mesopores, the water droplets gradually transform into spherical ones as pressure increases, indicating that the surfaces become more CO_2-wet. On the other hand, such phenomena are not pronounced in micropores because of stronger confinement effects. Based on the 2D density contour plots, the CO_2 distributions can be divided into six different zones. The highest CO_2 density is at the three-phase contact areas. Meanwhile, CO_2 presents a stronger tendency to accumulate in the solid-gas contact areas than the liquid-gas contact areas. While the presence of water reduces CO_2 adsorption in kaolinite pores, a slight enhancement is observed in siloxane mesopores when pressure is low thanks to CO_2 adsorption in Zone II and Zone V. Generally, water demonstrates more detrimental effects on CO_2 adsorption in gibbsite pores.

However, in this work, we do not consider the salt effect on the CO_2 sequestration. The formation water usually contains various ions (*e.g.*, Na^+, Ca^{2+}, CL^-, *etc.*) with the salinity up to 35 wt% [143] and the salt concentration is believed to have significant influences on CO_2

sequestration in shale nanopores [74]. In addition, we only consider one possible water content in shale reservoirs while the water configurations depend on their concentrations [33] which would accordingly affect the subsequent CO_2 adsorption. Therefore, it is worthwhile to investigate the effects of water and salt concentration on CO_2 sequestration in future.

Chaper 4 Recovery Mechanisms of Hydrocarbon Mixtures in Organic and Inorganic Nanopores During Pressure Drawdown and CO_2 Injection from Molecular Perspectives

Abstract

Competitive sorption of hydrocarbon mixtures (C_1-C_2-C_3) as well as CO_2 in shale nanopores is of critical importance to CO_2 enhanced shale gas recovery. While experiments can measure mixtures sorption from macroscopic perspective, the underlying mechanisms at nanoscale is still ambiguous. In this work, we use Grand Canonical Monte Carlo (GCMC) simulations to study competitive sorption of C_1-C_2-C_3 and C_1-C_2-C_3-CO_2 mixtures in organic and inorganic pores at reservoir conditions. The dependences of competitive sorption behavior on rock property, pore size, and fluid composition are explicitly examined. We find that while C_1 in the adsorption layer can be readily recovered during pressure drawdown, C_2 and C_3 are trapped in pores, especially in organic micropores. Injected CO_2 can effectively recover each component in the adsorption layer in organic pores, while in inorganic pores, the adsorption layer is dominated by CO_2 molecules, displacing all hydrocarbon components. CO_2 injection is an effective method to displace the heavier hydrocarbons. While pressure drawdown is more effective in inorganic pores, CO_2 injection performs better in organic pores. Our study should provide fundamental understanding about the recovery mechanisms of shale gas mixtures in various rocks and sheds light on the efficiency of CO_2 enhanced recovery in shale gas reservoirs.

4.1 Introduction

Nowadays, shale gas plays an important role in meeting the growing global energy demand [37, 144-146]. Unlike conventional reservoirs, small pores with sizes in the range of a few

nanometers to tens of micrometers are widely distributed in shale [22, 41, 147]. Fluid-surface interaction is significant in nanopores, resulting in strong surface adsorption and adsorbed gas may contribute up to 85% of total gas content [37, 144, 148]. Comparing to the conventional reservoirs, shale has heterogeneous rock compositions consisting of organic and inorganic matters [26, 41-46]. Organic matter is mainly composed of kerogen, which provides a significant contribution to gas sorption in shale [42, 47-50]. Inorganic matters, such as clay minerals (i.e., illite, montmorillonite, and kaolinite, etc.), can contain extensive amount of nanoscale pores and also greatly contribute to the gas-in-place (GIP) in shale [48, 51-53]. In addition to pressure drawdown, gas displacement by CO_2 injection can enhance gas recovery and, in the meantime, sequestrate the green-house-gas (GHG) into underground [149-152]. Recently, CO_2 huff-n-puff has gained extensive attention from engineers and scientists [39, 40, 153-156]. The huff-n-puff process is generally operated by three different stages: huff (CO_2 injection), soaking, and puff (pressure drawdown). Therefore, understanding the competitive sorption between hydrocarbons and CO_2 may provide key insights into the gas recovery mechanism during CO_2 huff-n-puff process.

In the past few decades, there have been a large number of works on the competitive sorption between C_1 and CO_2, mostly indicating that CO_2 is preferentially sorbed over C_1 in shale [157-164]. However, some shale formations [26, 54, 165] contain extensive amount of heavier alkanes, such as C_2 and C_3 [26]. As a result, understanding the sorption characteristics of C_1-C_2-C_3 mixtures in organic and inorganic nanopores is crucial for the accurate estimation of GIP and provide important insights into shale gas production. There have been several experimental measurements on hydrocarbon mixture competitive sorption in various adsorbents [166-169]. Reich *et al*. [166] studied C_1-C_2 binary mixture sorption in active carbons at 212-301 K and pressure up to 35 atm. Cheng *et al*. [167] studied the selective sorption of hydrocarbon gas mixtures in various clays,

activated carbon, coal and shale at temperatures of 299 and 353 K and pressure up to 3 atm, revealing a strong preferential sorption of heavier alkanes over C_1. Li *et al*. [168] measured C_1-C_2 sorption isotherms in shale at temperature from 313 to 373 K and pressure up to 160 bar. They found that C_2 exhibits preferential sorption over C_1. While these measurements provided important insights into hydrocarbon mixture sorption in organic and inorganic matters, the studies on these mixtures and CO_2 competitive sorption are rarely reported. In addition, experimental measurement cannot provide underlying mechanisms of hydrocarbon mixtures and CO_2 competitive sorption in various rocks from molecular perspectives, which play critical roles in nanoscale pores.

In this endeavor, molecular simulations and statistical mechanics based theoretical calculations become a viable and powerful option [39, 71, 170-177]. Pitakbunkate *et al*. [172] performed molecular dynamics (MD) and grand canonical Monte Carlo (GCMC) simulations to study C_1-C_2 mixture sorption in graphite nanopores. They reported that during pressure drawdown, the lighter components are released from the nanopores, while the heavier components are retained. Wang and Jin [176] used an engineering density functional theory (DFT) to study the competitive sorption C_1-C_2-C_3-nC_4 quaternary mixtures in graphite nanopores. They found that as pressure declines, while C_1 and C_2 can be released from the nanopores, large portion of C_3 and nC_4 may be trapped. Similar results are also suggested by Akkutlu and his coworkers [173, 177]. In addition, Sharma *et al*. [71] and Wang *et al*. [39] performed GCMC simulations to study the sorption behavior of C_1-C_2 mixtures in montmorillonite nanopores. They reported the C_1 and C_2 sorption isotherms as well as selectivity. Jin [24] *et al*. investigated nC_4-CO_2 mixture sorption in graphite slit-pores by GCMC simulations, suggesting that CO_2 injection may assist recovering nC_4 only at high pressures. Baek [178] *et al.* reported the stripping effect of CO_2 on capillary-condensed hydrocarbons containing C_1-C_5 in organic pores. They concluded that CO_2 can recover heavier

alkanes, once its mole fraction in bulk mixtures reaches 50%. Le *et al*. [179] conducted MD simulations to study the nC_4-CO_2 binary mixtures confined within slit-shaped silica and observed preferential CO_2 adsorption to the pore walls. To our best knowledge, while much attention has been paid to C_1 and its competitive adsorption with CO_2 in clay minerals [73, 108, 122, 180-183], competitive sorption between hydrocarbon mixtures and CO_2 remain largely unexplored. To some extent, these previous studies can implicate the efficiency of CO_2 injection, but fails to reflect the shale gas recovery process with CO_2 huff-n-puff. Recently, Zhou *et al*. [25] simulated the recovery of C_1 by CO_2 huff-and-puff from kerogen and compare the mechanisms of pressure drawdown and CO_2 injection processes on shale gas recovery. Nevertheless, such method has not been applied to study hydrocarbon mixture recovery in inorganic and organic matters.

In this work, we use GCMC simulations to systematically investigate hydrocarbon mixtures (C_1-C_2-C_3) production from organic and inorganic nanopores with different pore sizes during pressure drawdown and CO_2 injection at 333.15 K and pressure from 50 to 10 MPa. Scanning electron microscope (SEM) images of shale samples suggest widely distributed slit-shaped pores in shale [184-186]. Therefore, we use carbon slit nanopores [187] to study sorption characteristics in organic matter as in previous studies [24, 171, 173, 188-190]. Given that illite is one of the most common clay minerals in shale [26, 43, 46, 52], a full atomistic slit-shaped illite model [191] is used to study sorption in inorganic nanopores [122, 180, 181, 183]. The hydrocarbon molecules are simulated by united atom models and the three-site CO_2 is modeled by explicitly considering the short-range van der Waals and long-range electrostatic interactions. By incorporating these features, our simulations focus on a molecular-level understanding of competitive sorption between CO_2 and hydrocarbon mixtures in various nanopores and the recovery mechanisms.

The remainder of this paper is organized as follows. In **Section 4.2**, we introduce the simulation systems and procedures. In **Section 4.3**, we investigate the recovery characteristics and mechanism of each hydrocarbon component during pressure drawdown and CO_2 injection by considering different pore sizes and types. In **Section 4.4**, we discuss the potential implications for shale gas recovery. Finally, conclusions are drawn in **Section 4.5**.

4.2 Models and method

4.2.1 Molecular Model

In this work, we use the implicit 10-4-3 Steele potentials [187] to describe the fluid-wall interaction along the *z*-direction which is perpendicular to the surfaces for carbon slit nanopores,

$$\varphi_{wf}(z)=2\pi\rho_w\varepsilon_{wf}\sigma_{wf}^2\Delta\left[\frac{2}{5}\left(\frac{\sigma_{wf}}{z}\right)^{10}-\left(\frac{\sigma_{wf}}{z}\right)^{4}-\frac{\sigma_{wf}^4}{3\Delta\left(0.61\Delta+z\right)^3}\right], \tag{4-1}$$

where $\rho_w=114\ \text{nm}^{-3}$, $\Delta=0.335$ nm, $\varepsilon_{wf}=\sqrt{\varepsilon_w\varepsilon_f}$, with $\varepsilon_w=28$ K, $\sigma_{wf}=(\sigma_w+\sigma_f)/2$, with $\sigma_w=0.3345$ nm

We use fixed solid surfaces of illite which is a 2:1 clay mineral with the unit cell formula $Si_2AlO_5(OH)$ and the coordinate of each atom is from the X-ray diffraction of Pyrophyllite-1Tc powder [191, 192]. The parameters of unit cell are $a=0.51602$ nm, $b=0.89663$ nm, $c=0.93476$ nm, $\alpha=91.184^\circ$, $\beta=100.464^\circ$ and $\gamma=89.752^\circ$ [193]. The simulation cell consists of two clay sheets and each sheet contains 32-unit cells by replicating unit cell by 8 × 4 × 1. Owing to the isomorphic substitution in natural illite, one Si^{4+} is substituted by Al^{3+} every 8 Si^{4+} in the tetrahedral sheet so that the clay sheet has a negative charge. The negative charges are compensated by the interlayer K^+ ions [122, 180, 181], forming a unit cell with chemical formula as $K(Si_7Al)Al_4O_{20}(OH)_4$. The pore size W is defined as the distance between the center of mass of

oxygen atoms in silicon tetrahedron of the two sheets. The interactions among atoms in K-illite are described by CLAYFF [118], with potassium cations being mobile in the clay nanopores. Atomic structures of K-Illite with two sheets are shown in **Figure 4.1**.

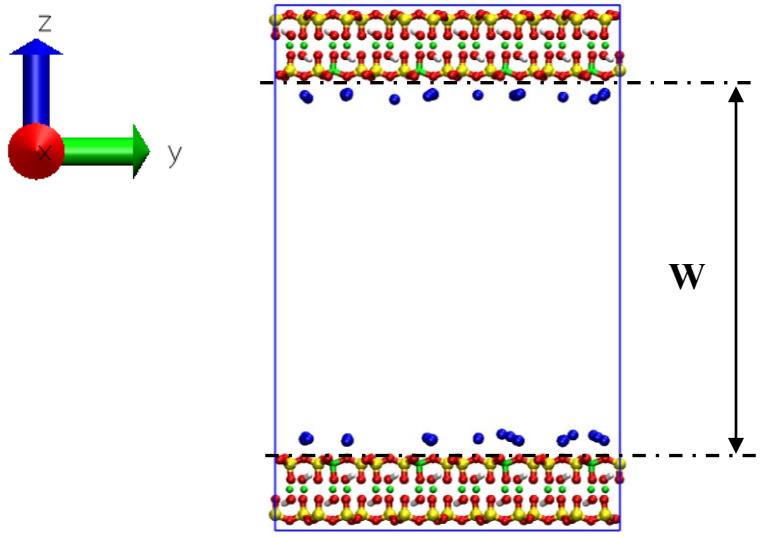

Figure 4.1 Schematic diagram of a K-Illite nanopore with pore size as 5 nm. Color scheme: yellow, Si; green, Al; red, O; white, H; blue, K.

For hydrocarbon and CO_2 molecules, we use the TraPPE force field [121, 194] to describe the non-bonded interactions based on pairwise-additive Lennard Jones (LJ) 12-6 potentials,

$$U\left(r_{ij}\right)=4\varepsilon_{ij}\left[\left(\frac{\sigma_{ij}}{r_{ij}}\right)^{12}-\left(\frac{\sigma_{ij}}{r_{ij}}\right)^{6}\right] \tag{4-2}$$

where r_{ij}, ε_{ij}, and σ_{ij} are the separation distance, LJ well depth, and LJ size, respectively. The cross interactions between the unlike atoms i and j, are computed using the standard Lorentz-Berthelot combining rules [76]. For TraPPE force field, C_1 molecule is modeled as single site atom. The longer alkanes are regarded as united atoms whose bond length and angle are fixed as 1.54 Å and 114°, respectively. The CO_2 molecule is treated as a rigid and linear structure with a fixed

bond length of 1.16 Å and angle of 180°. The Coulomb potentials are used to compute the interactions of clay-CO_2 and CO_2-CO_2,

$$E_{coul} = \frac{e^2}{4\pi\varepsilon_o} \sum_{i \neq j} \frac{q_i q_j}{r_{ij}} \tag{4-3}$$

in which q_i is the partial charge of the site. All the LJ parameters and partial charge are listed in **Table B.1**. The short-range LJ interactions are all truncated at a distance of 1.2 nm. A rectangular box with the dimension of $L_x = L_y = 4$ nm in *x*- and *y*-directions for organic pores, while illite has box length of $L_x = 4.128$ nm and $L_y = 3.584$ nm along *x*- and *y*-directions, respectively. We use the three-dimensional Ewald summation (EW3D) to account for the long-range electrostatic interactions and slab geometry [195]. For a slab geometry system, the conventional Ewald summation method cannot be applied directly, since there is no periodicity in the one of three dimensions which is perpendicular to the surface. A commonly used approach is to create a sufficiently large empty space along the direction vertical to the surface by elongating the simulation cell [196, 197]. Spohr *et al.* [198] suggested that results for EW3D converge to the two-dimensional Ewald summation (EW2D), when the empty distance is large enough. As a result, to avoid the influence from the periodic images in the *z*-direction, an empty space was placed in the simulation cell with a length much larger than L_x or L_y in this work.

4.2.2 Simulation details

The competitive sorption of hydrocarbon mixtures and CO_2 are performed in the grand canonical (μVT) ensemble with MCCCS Towhee [125]. Fluids in the pores are in a chemical equilibrium with those in an external bulk reservoir for given temperature and pressure which denotes that of bulk [164]. The snapshots are presented by Visual Molecular Dynamics (VMD) [199] in CPK model and the size of each atoms in the snapshots is smaller than its real LJ sizes.

According to actual shale gas reservoir conditions [26, 54, 165], we use a bulk mole ratio of 80:15:5 for C_1-C_2-C_3 mixtures at the initial reservoir pressure $P_0 = 50$ MPa, which is a typical pressure for most shale gas formation. To investigate the pore size effect, we use $W = 2$ and 5 nm to represent the micropore and mesopore, respectively.

The recovery of hydrocarbon mixtures can be separated into two different mechanisms: pressure drawdown and CO_2 injection [164]. The simplified recovery process consists of pressure drawdown and CO_2 injections as illustrated in **Figure 4.20**. Firstly, to initiate the gas production by the primary pressure drawdown, we lower the bulk pressure from P_0 to $P_1 = 15$ MPa, assuming that the fluids in nanopores are in chemical equilibrium with an infinite bulk volume of hydrocarbon mixtures. Subsequently, CO_2 is introduced into the bulk volume until its bulk mole fraction reaches 50%. The equilibrium pressure after CO_2 injection are calculated by Peng-Robinson equation of state (PR-EOS) [200]. During this process (huff), we assume a constant volume of the bulk reservoir (fractures). Therefore, the density of each hydrocarbon component in the bulk phase of C_1-C_2-C_3-CO_2 mixtures at an elevated pressure $P_2 = 28.7$ MPa is the same as that in C_1-C_2-C_3 mixtures at P_1. After the system reaches equilibrium, a pressure drawdown process (puff) is applied, starting from P_2 to $P_3 = 10$ MPa, while the bulk composition remains unchanged.

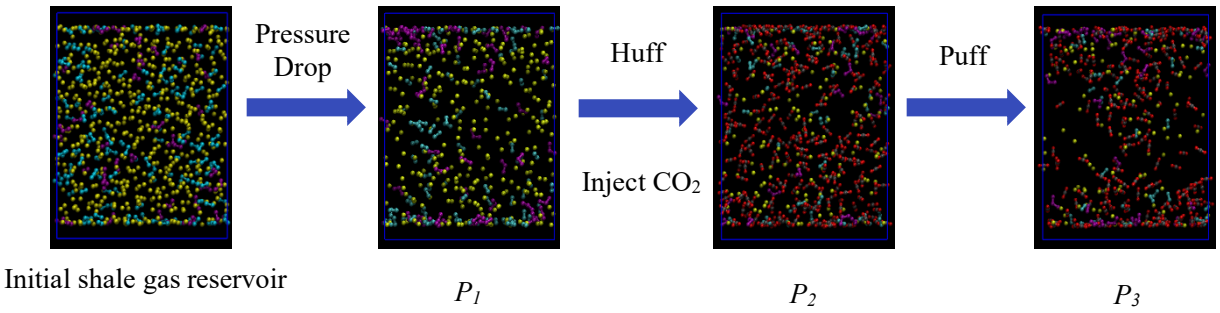

(a) Organic Pores

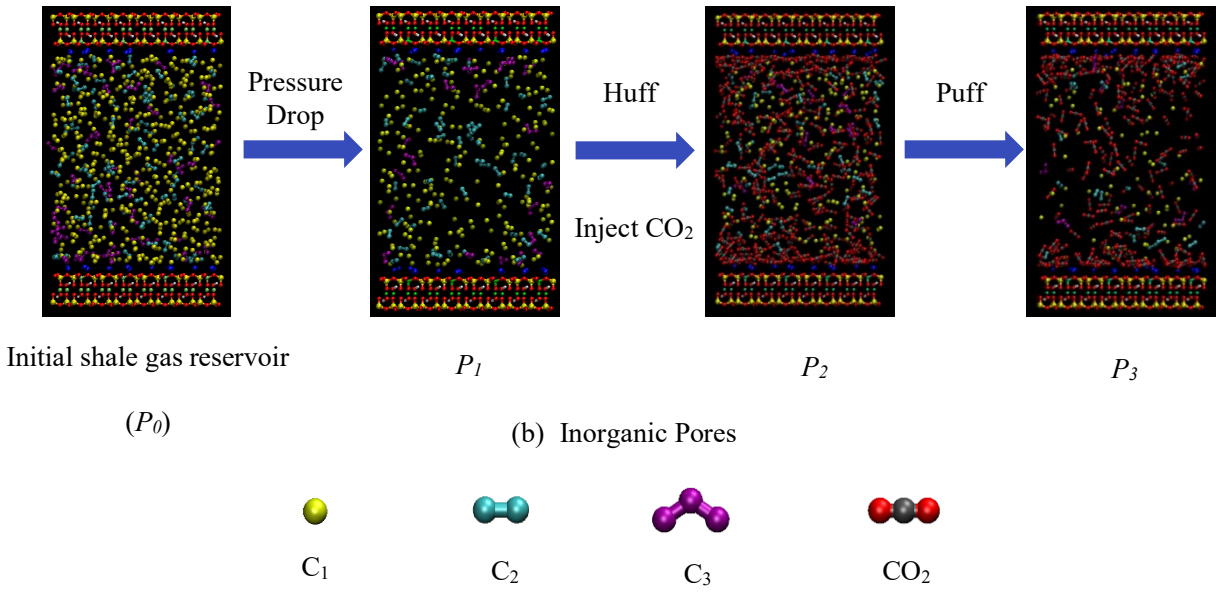

Figure 4.2 Schematic representation of shale gas recovery process in organic (top) and inorganic (bottom) pores.

During MC simulation, K-Illite structure is kept fixed. Transitional move is applied to C_1 molecules and a C_1 molecule is randomly removed from or inserted into the simulation box at equal probability, depending on the C_1 chemical potential in the bulk volume. For simulations of CO_2 and heavier alkanes, in addition to the MC moves mentioned above, a rotational move is applied and we employ a biased MC algorithm to insert/remove these molecules [201, 202]. As for potassium ions, we only perform random displacement move. The simulation consists of 0.15 million MC cycles per adsorbate molecule for equilibrium and 0.5 million MC cycles per adsorbate molecule for sampling the density profiles.

The chemical potentials are obtained by the Widom's insertion method [126] using Monte Carlo simulations with *NVT* ensemble in bulk phase. The bulk densities of mixtures at given pressure and temperature are calculated from the PR-EOS [200]. All simulations are performed at system temperature of $T = 333.15$ K. We should note that the pressure in the simulations represents that of the external bulk reservoir, which is in chemical equilibrium with the nanopores.

4.3 Results and Discussion

4.3.1 Primary production with pressure drawdown from P_0 to P_1

4.3.1.1 Organic pores

The snapshots of C_1-C_2-C_3 mixtures in carbon slit nanopores at P_0 and P_1 are depicted in **Figure 4.3**. In the micropores and mesopores, as pressure declines, the amount of C_1 molecules (yellow) decreases both in the surface adsorption layer and the middle of the pore. For C_2 (cyan) there is no obvious change in the proximity of the surface. However, the propane distribution change (purple) is opposite to C_1, showing an enrichment near the surface at a lower pressure.

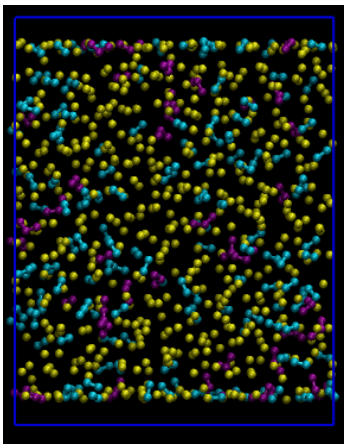

(a) Organic Mesopores, P_0

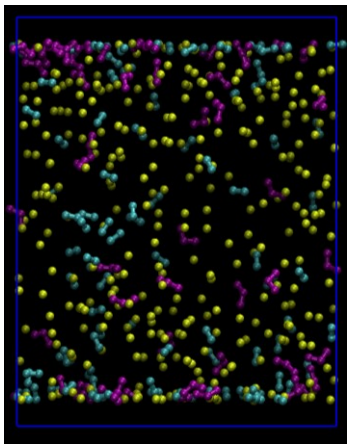

(b) Organic Mesopores, P_1

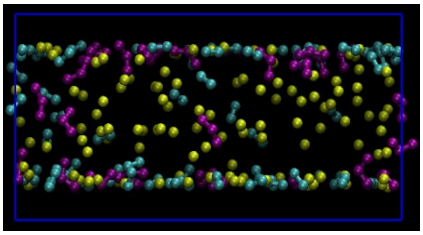

(c) Organic Micropores, P_0

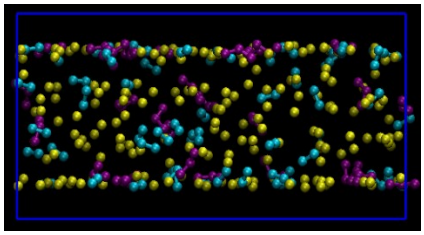

(d) Organic Micropores, P_1

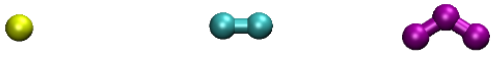

C_1 C_2 C_3

Figure 4.3 Snapshots of C_1-C_2-C_3 mixtures at 333.15 K in organic (a) mesopores at P_0; (b) mesopores at P_1; (c) micropores at P_0; (d) micropores at P_1.

In order to further investigate desorption behavior of each component in organic nanopores, the hydrocarbon density distributions in micropores and mesopores at P_0 and P_1 are shown in **Figure 4.4**. Each hydrocarbon component forms surface adsorption due to strong fluid-surface interaction. The density in the middle of mesopores approaches the bulk, while that of micropores do not converge to the bulk, indicating that there is no free gas region. In mesopores, for C_1, the peak of the first adsorption layer drops as pressure decreases, while there is a negligible change for C_2. Nevertheless, C_3 surface adsorption increases during pressure drawdown, which indicates that in the primary production, as pressure drops, it is the lighter components that are more easily produced, while the heavier components may tend to be trapped within the nanopores. This is because at a lower pressure, the competition from lighter molecules become weaker, so the heavier one is more readily adsorbed on the pore surfaces. Similar behavior has been reported in the study of adsorption of hydrocarbon mixtures in zeolites [203] and graphene nanopores [175, 188]. The changes of density profiles follow similar trends in micropores.

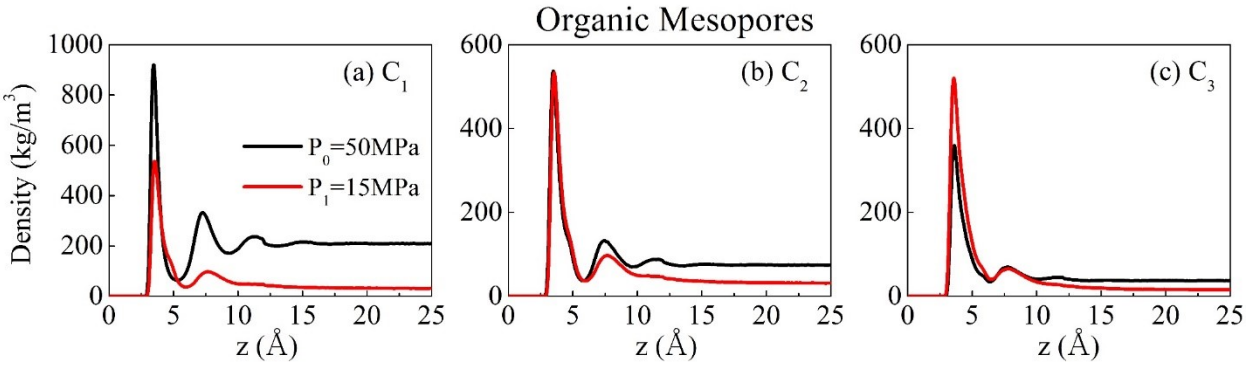

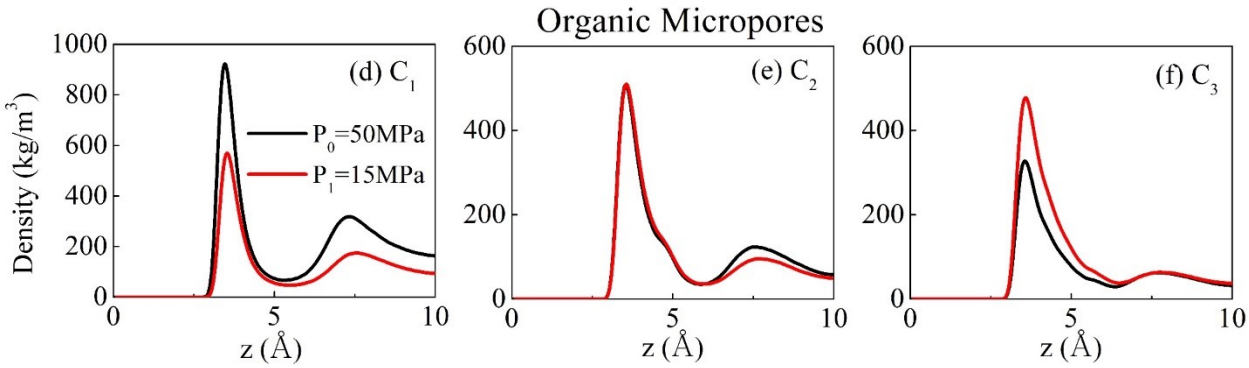

Figure 4.4 Density profile of (a) C_1; (b) C_2; (c) C_3 in organic mesopores and (d) C_1; (e) C_2; (f) C_3 in organic micropores at 333.15 K, respectively.

4.3.1.2 Inorganic pores

The snapshots of C_1-C_2-C_3 mixtures in K-illite at P_0 and P_1 in mesopores and micropores are shown in **Figure 4.50**. The potassium cations align close to the clay surfaces which have negative charges, due to the strong electrostatic interactions, as in previous studies [122, 180, 181]. Similar to organic pores, the number of C_1 molecules decreases dramatically as pressure drops. However, comparing with organic pore, there is no apparent accumulation near the surface for C_3.

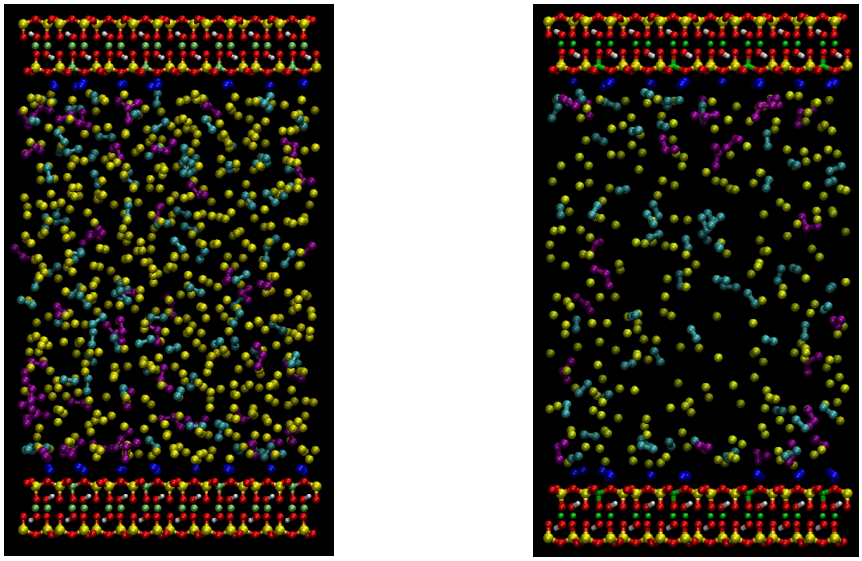

(a) Inorganic Mesopores, P_0 (b) Inorganic Mesopores, P_1

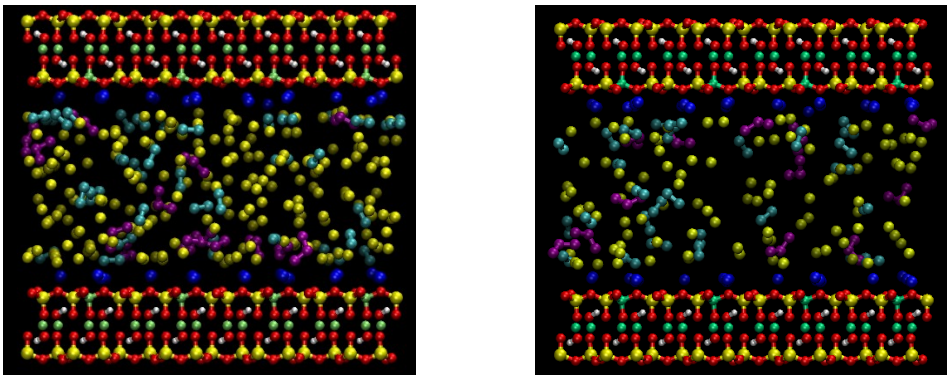

(c) Inorganic Micropores, P_0 (d) Inorganic Micropores, P_1

C_1 C_2 C_3

Figure 4.5 Snapshots of C_1-C_2-C_3 mixtures at 333.15 K in inorganic (a) mesopores at P_0; (b) mesopores at P_1; (c) micropores at P_0; (d) micropores at P_1.

In **Figure 4.6** we show the density distributions of each hydrocarbon component P_0 and P_1 in inorganic mesopores and micropores. Similar to the organic pores, each specie coexists as surface adsorption and free phase in mesopores, while no free region can be observed in micropores. However, the peak value of the adsorption layer in K-illite is much smaller than those in carbon mesopores and micropores, dictating a weaker fluid-surface affinity. The first adsorption layer of C_2 cannot be recovered in organic pores, while in the clay it is removable [39]. For C_3 in K-illite pores, the increase in density distributions during pressure drawdown is insignificant compared to organic pores. Therefore, during pressure drawdown, it is still difficult to recover the heavier components from clay nanopores, especially for C_3.

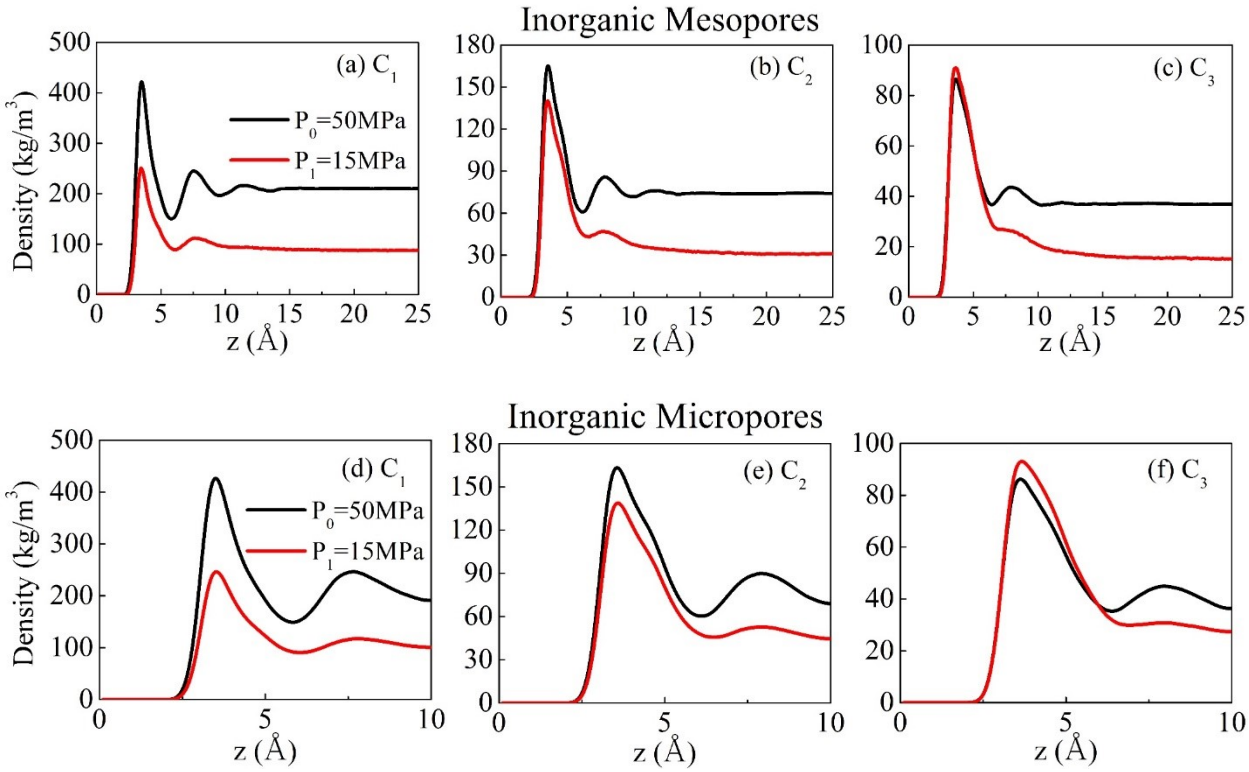

Figure 4.6 Density profile of (a) C_1; (b) C_2; (c) C_3 in inorganic mesopores and (d) C_1; (e) C_2; (f) C_3 in inorganic micropores at 333.15 K, respectively.

4.3.2 CO_2 injection with Huff -n-Puff

During this process, the bulk pressure first increases from P_1 to P_2 (huff), then decreases to P_3 (puff).

4.3.2.1 Organic pores

We present the snapshots of hydrocarbon and CO_2 mixtures at P_1 (before CO_2 huff), P_2 (after CO_2 huff), and P_3 (after puff) in organic mesopores and micropores in **Figure 4.7**. The mesopores and micropores follows the similar trend. During the puff process as shown in **Figure 4.7(b)** and **Figure 4.7(e)**, much more CO_2 molecules are adsorbed on the surfaces than the alkanes. Meanwhile, the amount of the adsorbed hydrocarbon molecules becomes fewer after CO_2 injection. Contrary to the huff process, an obvious increase in the number of C_3 molecules in the surface region can

be observed, which is similar to the pressure drawdown without CO_2 injection. **Figure 4.8** shows the density profile of each component in C_1-C_2-C_3-CO_2 mixtures in organic mesopores and micropores at various pressures. It shows that CO_2 exhibits a higher affinity to the organic pore surfaces compared with hydrocarbons [157, 159, 161]. In addition, the CO_2 distributes closer to the surfaces.

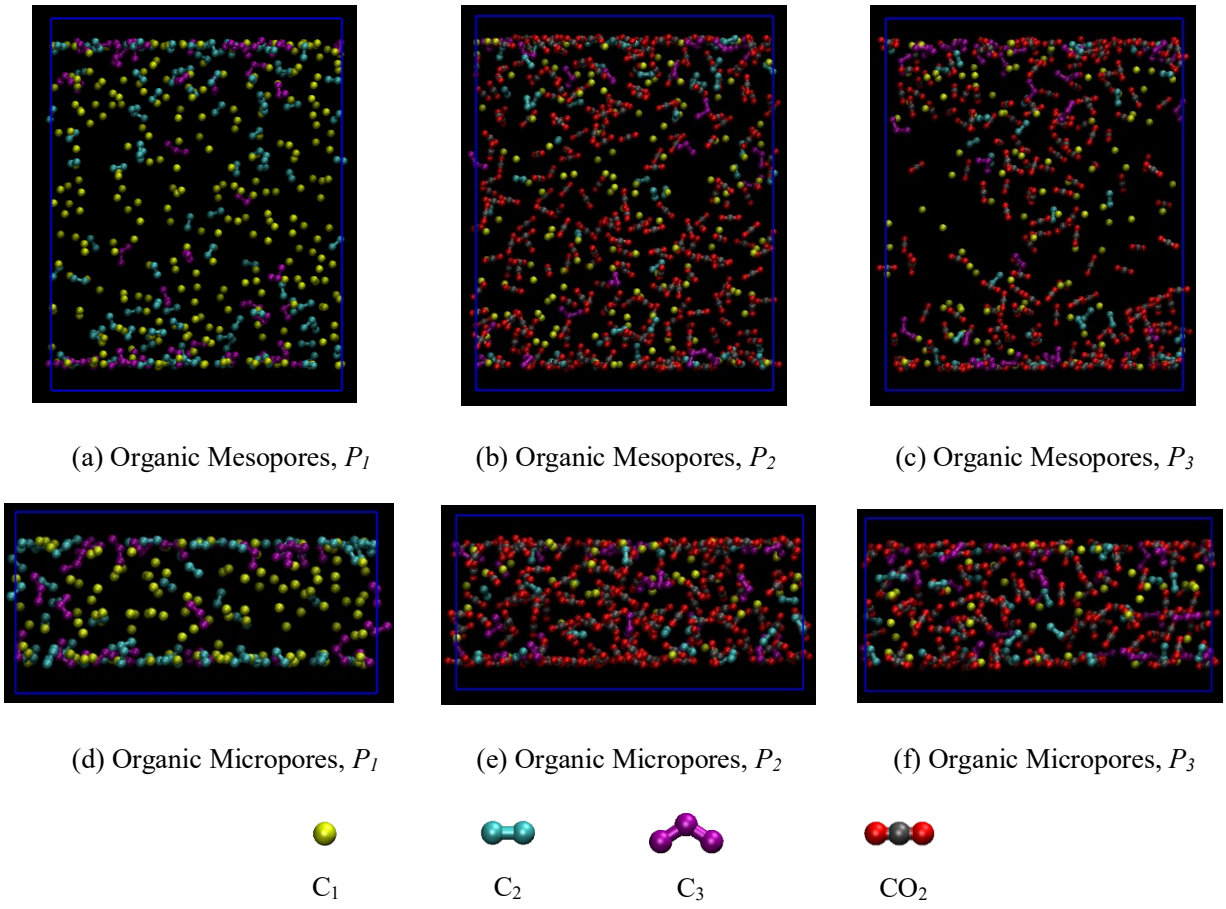

Figure 4.7 Snapshots of (a) C_1-C_2-C_3 mixtures in organic mesopores at P_1 (before CO_2 huff); (b) C_1-C_2-C_3-CO_2 mixtures in organic mesopores at P_2 (after CO_2 huff); (c) C_1-C_2-C_3-CO_2 mixtures in organic mesopores at P_3 (after puff); (d) C_1-C_2-C_3 mixtures in organic micropores at P_1 (before CO_2 huff); (e) C_1-C_2-C_3-CO_2 mixtures in organic micropores at P_2 (after CO_2 huff); (f) C_1-C_2-C_3-CO_2 mixtures in organic micropores at P_3 (after puff) at 333.15 K.

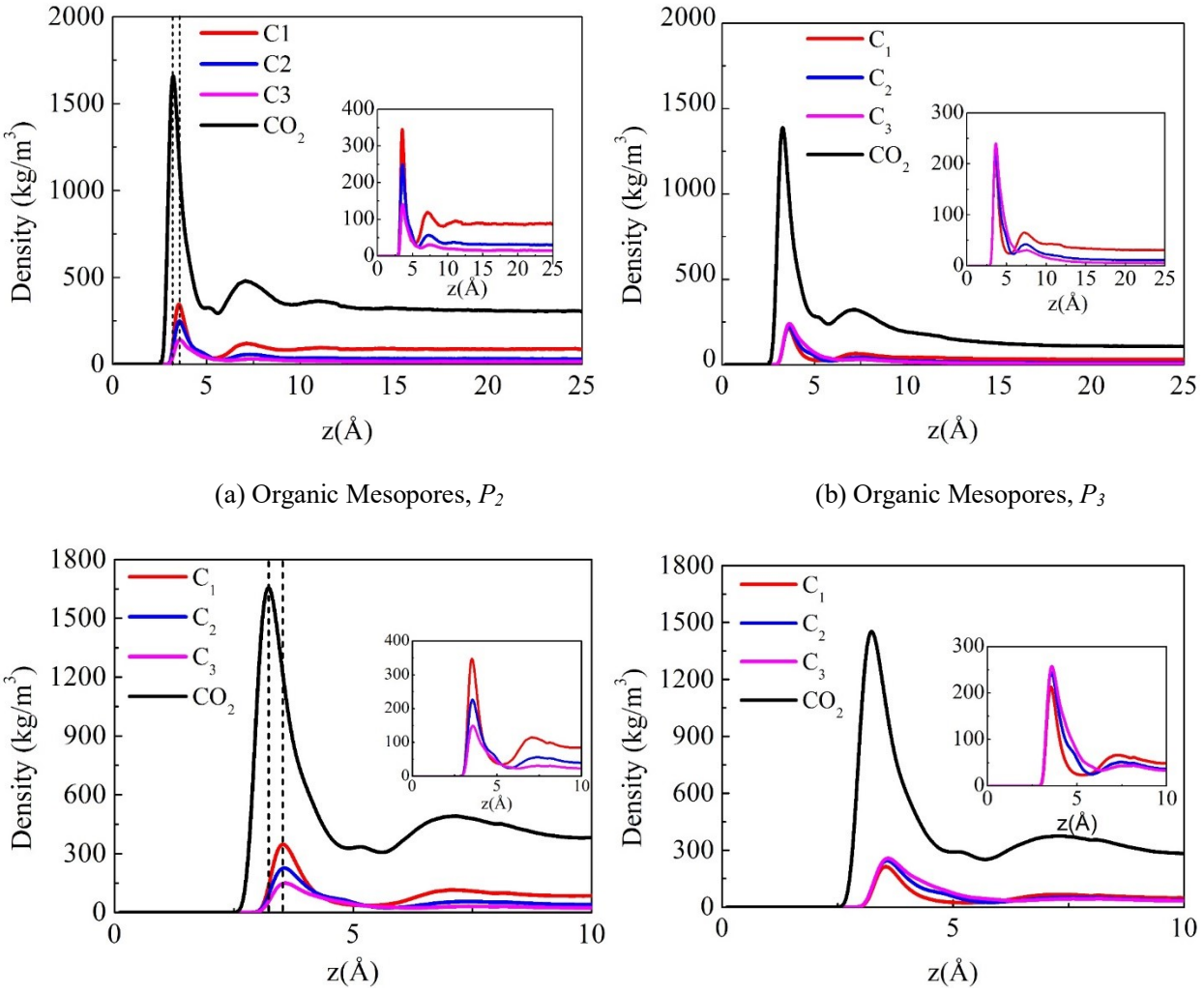

(a) Organic Mesopores, P_2

(b) Organic Mesopores, P_3

(c) Organic Micropores, P_2

(d) Organic Micropores, P_3

Figure 4.8 Density profile of each component in organic (a) mesopores at P_2; (b) mesopores at P_3; (c) micropores at P_2; (d) micropores at P_3. Dashed lines represent the location of the first adsorption layer.

Figure 4.9 displays the density profile of each hydrocarbon component during pressure drawdown and CO_2 injection for organic mesopores and micropores. In mesopores, during the CO_2 huff process (from P_1 to P_2), all hydrocarbon components reveal a drastic decrease in the first adsorption layer due to CO_2 displacement, which is in line with Akuttlu *et al.* [204]. During puff process, while the adsorbed C_1 can be continuously produced, C_2 in the adsorption layer cannot be

readily recovered. On the other hand, C_3 molecules are re-adsorbed on the surfaces, which is similar to **Figure 4.6**. In organic micropores, as hydrocarbon component become heavier, it shows a more severe trapping effect during puff process.

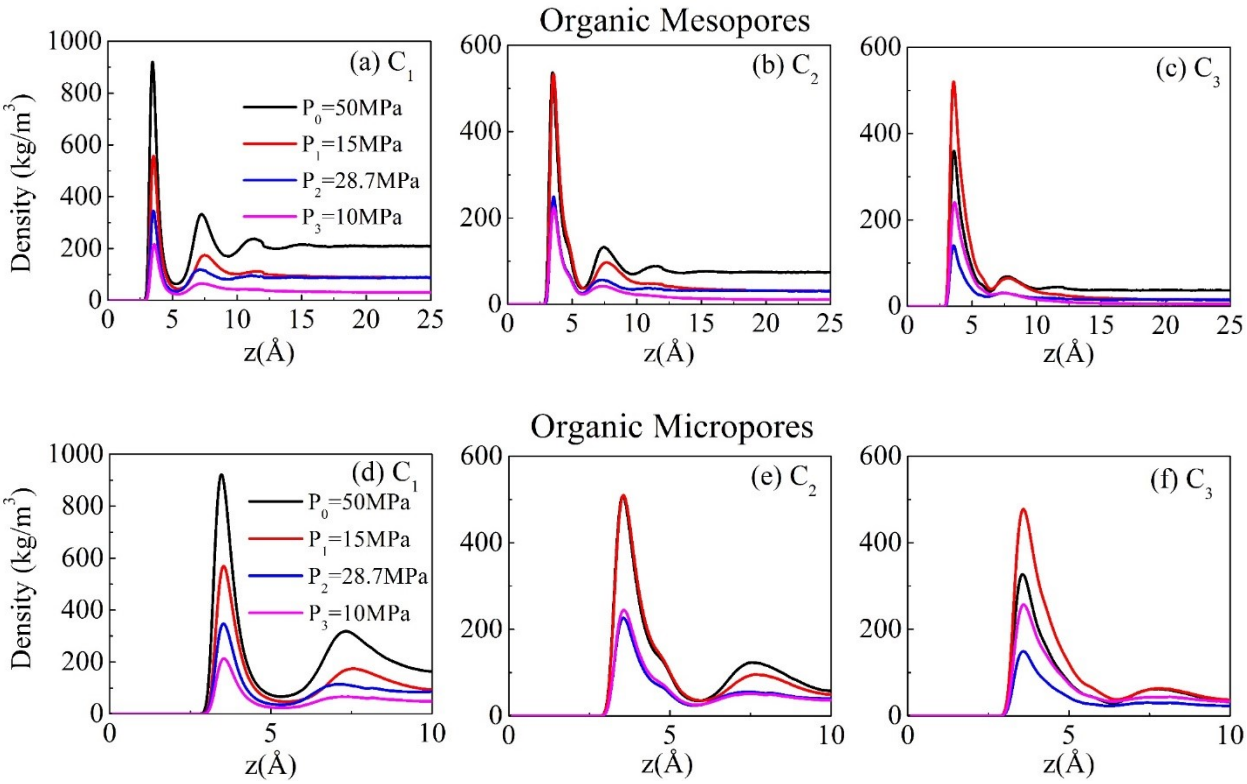

Figure 4.9 Density distributions of (a) C_1; (b) C_2; (c) C_3 in organic mesopores and (d) C_1; (e) C_2; (f) C_3 in organic micropores at 333.15 K.

4.3.2.2 Inorganic pore

We present the snapshots of hydrocarbon and CO_2 mixtures at P_1 (before CO_2 huff), P_2 (after CO_2 huff), and P_3 (after puff) in inorganic mesopores and micropores in **Figure 4.10**. Similar to **Figure 4.5**, the potassium cations are bound closely to the surfaces. Unlike the organic pore with CO_2 injection as shown in **Figure 4.7**, the surface adsorption is dominated by CO_2 molecules and hydrocarbon molecules are depleted from the surfaces. To better understand the molecular distributions during CO_2 huff-n-puff process in inorganic mesopores and micropores, we present

the density profile of each component in **Figure 4.11**. The peak value of CO_2 density distributions in K-illite is about 1.5 times higher than that in organic pores. While CO_2 molecule is charge neutral and has zero dipole moment, it has a strong quadrupole moment [205, 206], which increases sorption coupled with the charged clay atoms. In addition, we find that peaks of hydrocarbon density distributions are shifted towards the middle of the pores. In other words, hydrocarbon molecules form a minor adsorption layer upon the CO_2 adsorption layer at the clay surfaces [183].

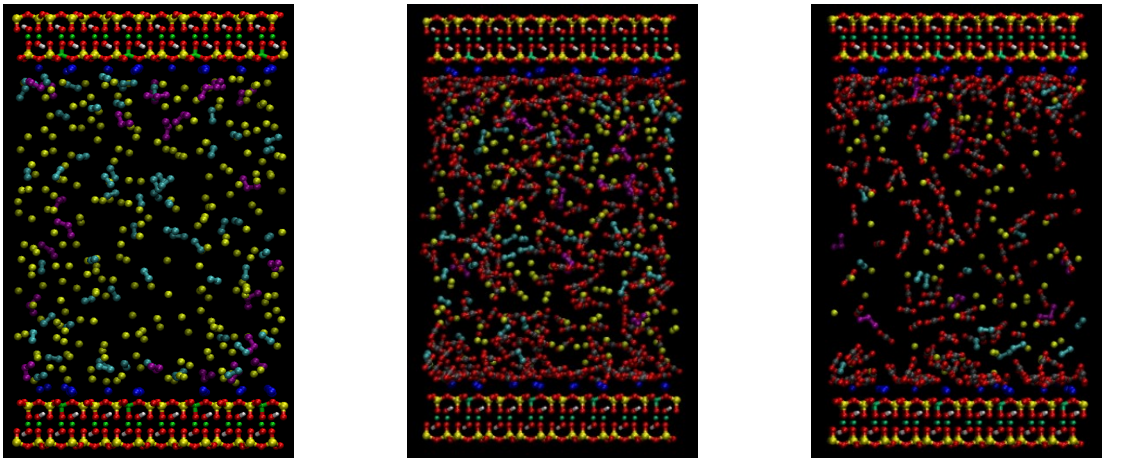

(a) Inorganic Mesopores, P_1 (b) Inorganic Mesopores, P_2 (c) Inorganic Mesopores, P_3

(d) Inorganic Micropores, P_1 (e) Inorganic Micropores, P_2 (f) Inorganic Micropores, P_3

Figure 4.10 Snapshots of (a) C_1-C_2-C_3 mixtures in inorganic mesopores at P_1 (before CO_2 huff); (b) C_1-C_2-C_3-CO_2 mixtures in inorganic mesopores at P_2 (after CO_2 huff); (c) C_1-C_2-C_3-CO_2 mixtures in inorganic mesopores at P_3 (after puff); (d) C_1-C_2-C_3 mixtures in inorganic micropores at P_1 (before CO_2 huff); (e) C_1-C_2-C_3-CO_2 mixtures in inorganic micropores at P_2 (after CO_2 huff); (f) C_1-C_2-C_3-CO_2 mixtures in inorganic micropores at P_3 (after puff) at 333.15 K.

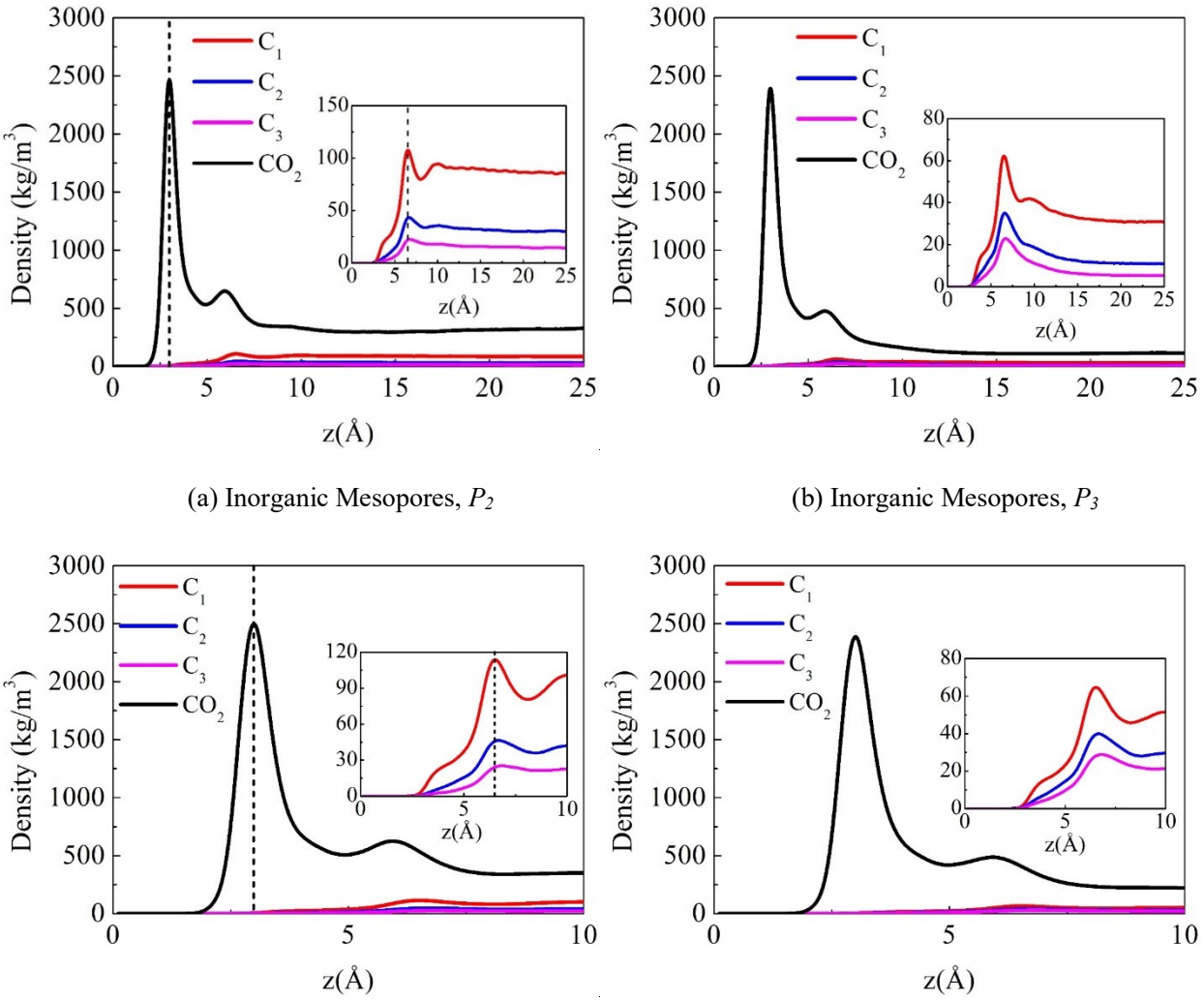

(a) Inorganic Mesopores, P_2

(b) Inorganic Mesopores, P_3

(c) Inorganic Micropores, P_2

(d) Inorganic Micropores, P_3

Figure 4.11 Density profile of each component in inorganic (a) mesopores at P_2; (b) mesopores at P_3; (c) micropores at P_2; (a) micropores at P_3. Dashed lines represent the location of the first adsorption layer.

Figure 4.12 presents the density profiles of each hydrocarbon component during pressure drawdown and CO_2 injection for inorganic mesopores and micropores. In mesopores, CO_2 huff causes a significant reduction of hydrocarbon adsorption layer and shifts it towards the middle of the pores. During puff process, both of C_1 and C_2 can be recovered from the adsorption layer, while

C_3 molecules still reside in its adsorption layer. In micropores, during puff process. the amount of C_3 in adsorption layer slightly increases.

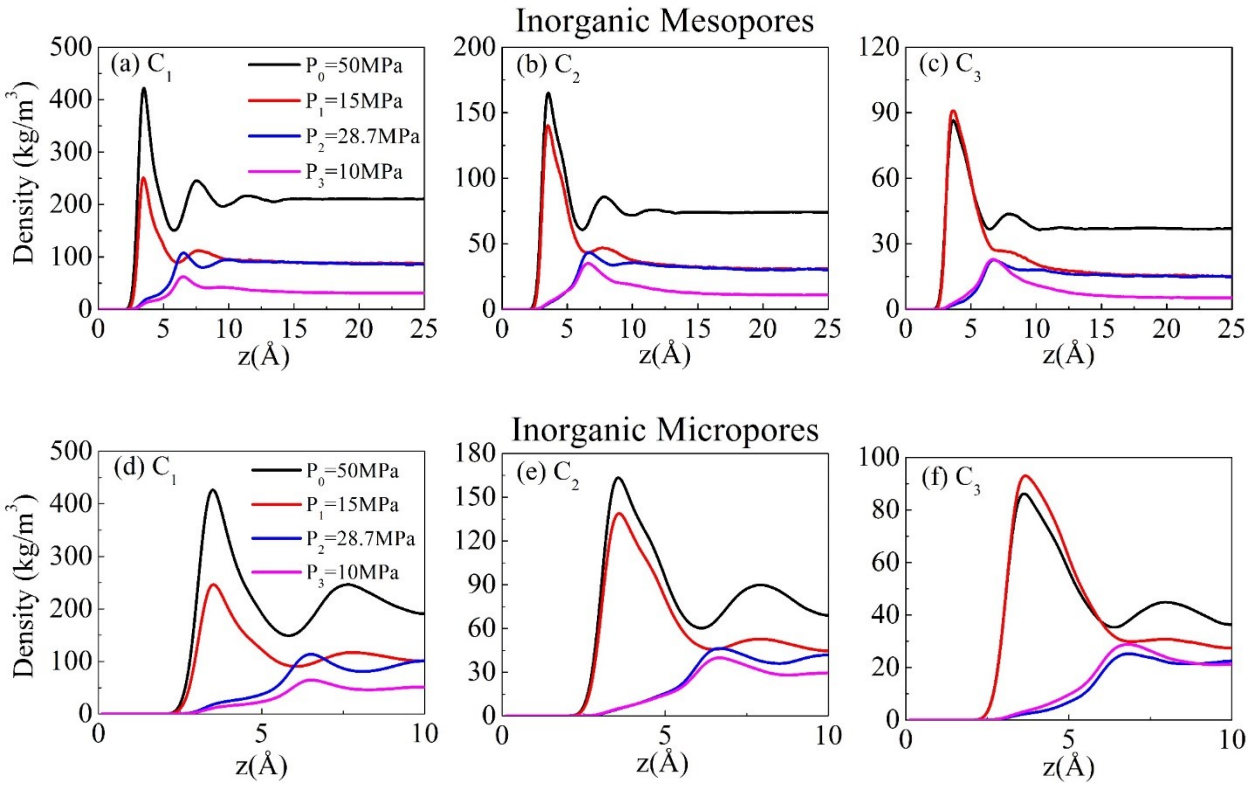

Figure 4.12 Density distributions of (a) C_1; (b) C_2; (c) C_3 in organic mesopores and (d) C_1; (e) C_2; (f) C_3 in organic micropores at 333.15 K.

4.4 Implication for shale gas recovery

In the previous sections, we revealed the hydrocarbon mixtures recovery mechanisms in organic and inorganic pores during pressure drawdown process and CO_2 injection. To provide a better insight for shale gas recovery, we use the average densities in pores to compare the recovery process qualitatively as shown in **Figure 4.13**. The average density of each hydrocarbon component in pores $\bar{\rho}_i$ is given as,

$$\bar{\rho}_i = \frac{\langle N_i \rangle M_i}{V N_A}, \tag{4-4}$$

where $\langle N_i \rangle$ is the ensemble averaged number of component i in the pores, M_i denotes the molecular weight of component i, V represents the pore volume, and N_A is the Avogadro constant.

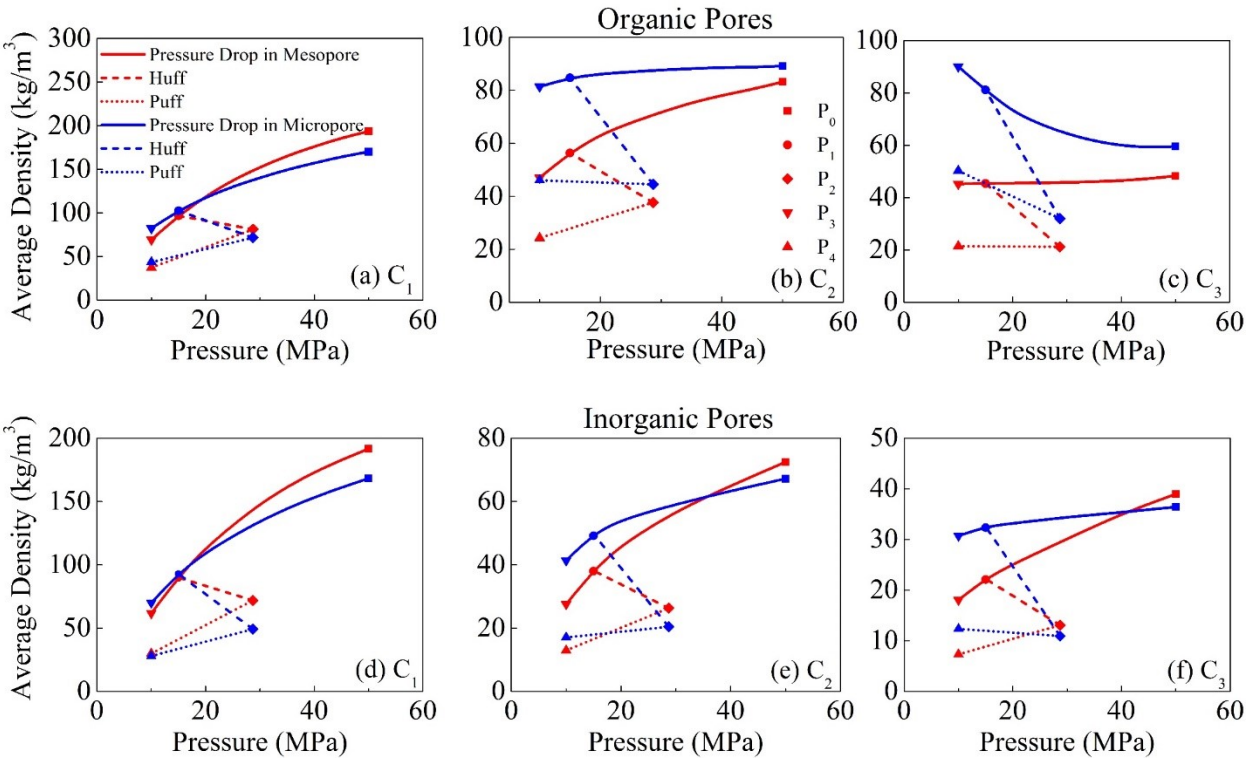

Figure 4.13 Average density of (a) C_1; (b) C_2; (c) C_3 in organic pores and (d) C_1; (e) C_2; (f) C_3 in inorganic pores at 333.15 K. The red lines and symbols represent the mesopores and blue lines and symbols represent the micropores. The pressure drop, huff, and puff process are shown in solid, dashed and short dotted lines, respectively. The solid squares, spheres, diamonds, upper-triangle, and lower-triangle symbols represent P_0, P_1, P_2, P_3, and P_4, respectively.

In this part we design two different scenarios to exploit the shale gas reservoir with the same initial reservoir pressure P_0. For **Scenario I**, we drop the reservoir pressure from P_0 to $P_4 = 10$ MPa without CO_2 injection. In organic pores, most of the C_1 and part of C_2 can be released, while C_3 is prone to be trapped in the pores, indicating that the heavier components may be difficult to

be produced only relying on the natural energy drive. This trapping phenomenon is particularly severe for C_3 as can be seen from **Figure 4.13(c)** and even shows an upward trend in average density with pressure depletion in organic micropores. For inorganic pores, all hydrocarbon components can be released from the nanopores during pressure drawdown. The production potential tends to decrease for the heavier hydrocarbon components and the smaller pore size.

In **Scenario II**, after pressure drawdown from P_0 to P_1, we conduct CO_2 huff-n-puff process until $P_3 = P_4$. For all cases, the CO_2 huff process is very efficient in hydrocarbon displacement. However, the following puff process has adverse effect on the heavier hydrocarbon production, especially in micropores. By comparing the average density at $P_3 = P_4$ in **Scenario I** and **II**, although in some cases, the huff process is detrimental for the recovery of heavier hydrocarbon, the overall huff-n-puff process is favorable for production.

To better explain **Scenario II**, in **Figure 4.14**, we present the recovery efficiency RF_k for component k during different processes, which is defined as

$$RF_{k,i} = \frac{\bar{\rho}_{P_i} - \bar{\rho}_{P_{i+1}}}{\bar{\rho}_{P_0}} \times 100\% \ (i = 0,1,2; k = C_1, C_2, C_3)\,, \tag{4-5}$$

where $\bar{\rho}_{P_i}$ is the average density at pressure P_i. We observe that $RF_{k,0}$ during pressure drop from P_0 to P_1 decreases as pore size becomes smaller and hydrocarbon becomes heavier. Compared with organic pore, $RF_{C_2,0}$ and $RF_{C_3,0}$ are much higher in inorganic pores, while for $RF_{C_1,0}$ in organic and inorganic pores are comparable. Interestingly, we observe that $RF_{C_3,0}$ can be negative in organic micropores. During CO_2 injection and pressure from P_1 to P_2, $RF_{C_3,1}$ is the highest in both organic and inorganic pores, indicating that the huff process is most suitable for the heaviest component recovery. In addition, $RF_{k,1}$ becomes less significant as pore size increases. The huff

process is more efficient in organic pores than inorganic ones. The recovery behavior of puff process from P_2 to P_3 is similar to that from P_0 to P_1. A weaker efficiency of puff process can be observed in micropores and for the heavier hydrocarbons.

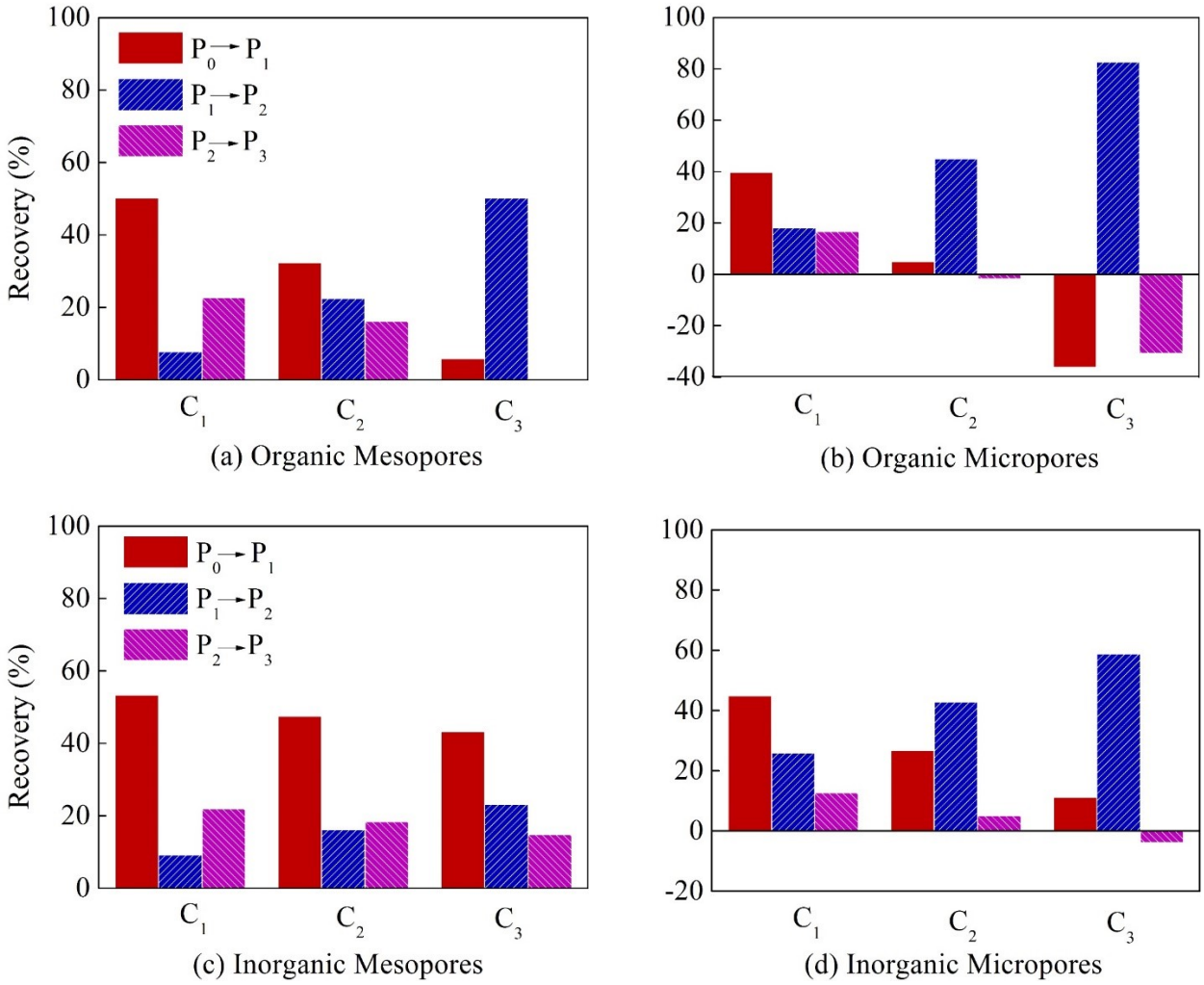

Figure 4.14 Recovery efficiency of each component in organic and inorganic mesopores and micropores in **Scenario II**.

4.5 Summary

In this work, we use GCMC simulations to study the recovery mechanism of hydrocarbon mixtures from organic and inorganic pores during pressure drawdown and CO_2 injection. During primary production with pressure drawdown, C_1 can be easily released from nanopores, while C_2

and C_3 incline to remain in the adsorption layer. Such trapping behavior can be observed in both organic and inorganic pores and is more pronounced in micropores. CO_2 injection (huff) can displace most of hydrocarbons from the surface in organic pores. For inorganic pores, the first adsorption layer is dominated by CO_2 molecules, while hydrocarbon molecules can be hardly observed. For smaller pores and heavier hydrocarbons, the CO_2 displacement becomes more effective. The mechanism of the puff process is similar to the pressure drawdown and may not favorable to stripping the heavier fluids in the smaller pores. We also designed two exploitation scenarios for shale gas production and analyzed the recovery efficiency for various hydrocarbons in organic and inorganic pores. Pressure drawdown is more efficient for the lighter hydrocarbon recovery, while CO_2 injection is an effective method to recovery the heavier ones. Our work should shed lights into the optimization of pressure drawdown and CO_2 injection during shale gas production.

Chaper 5 CO_2-Responsive Surfactant for Oil-in-Water Emulsification and Demulsification from Molecular Perspectives

Abstract

To economically and environmentally recover oil from reserviors and promote the CO_2 utilization (CU) project, CO_2 repsonsive surfactants have been developed to undertake mutiple tasks including emusification and demulsification during different production stages. Understanding the switching mechanims of great importance to the choice and design of high-performance CO_2 responsive surfactants. In this work, we performed molecular dynamics (MD) simulations to study the emulsification and demulsification processes of a heptane/water mixture in the presence a typical CO_2 responsive surfactant-lauric acids (LA). Before injecting CO_2, the deprotonated lauric acids (DLA) can stabilize O/W emulsions in aqueous solution due to strong electrostatic repulsions and high interfacial activity of DLA, wheras the protonation of lauric acid (PLA) arising from CO_2 injection would result in the coalescence of the emulsion droplets thanks to the greatly reduced hydrophilicity of the polar groups of lauric acids and surface charge neutralization, which is unfavorable to stabilize emulsions. The potential mean force (PMF) results shows a high energy barrier preventing the fusion process when two emulsion approach to each other in the absence of CO_2, indicating a high stability of the emulsions. However, when the DLA turn to be PLA, the energy barrier disappeared and an attraction force occur due to entropic effect if two emulsions are close enough. Our study provides important insights into the structural properties of emulsions before and after CO_2-triggered switching and sheds lights on the switching mechanims which may assist in picking and designing efficient CO_2 responsive surfactants.

5.1 Introduction

Following primary and secondary oil recoveries, approximately a third to half of the original

oil in place (OOIP) remains trapped underground resulting in a great amount of residual oil [207, 208]. As an effective enhanced oil recovery (EOR) technique [57], surfactant flooding has been widely used to further recover residual oil [58, 59]. One of the working mechanisms for surfactant flooding is to reduce oil-water interfacial tension (IFT) thanks to the amphiphilic characteristics of surfactants [60, 61], which is favorable for the formation of stable oil-in-water (O/W) emulsions, improving both microscopic displacement and macroscopic sweep efficiencies [62, 209]. In addition, formation of O/W emulsions is an effective approach to reduce crude oil viscosity during pipeline transportation process [210]. Unfortunately, these stable emulsions are unfavorable for a number of downstream operations, due to the increasing difficulties in oil-water separations [211] and oily wastewater treatments [212]. Traditionally, chemical demulsifiers and/or physical forces [211, 213, 214] can be applied to break O/W emulsions. However, these methods often come with high cost and sometimes may lead to a secondary environmental pollution [215]. Therefore, it is necessary to develop smart surfactants which can undertake multiple tasks including emulsification and demulsification to make oil production economically viable and environmentally sustainable.

In this regard, CO_2-responsive surfactants have attracted great attention among scientists and engineers in recent years due to their reversible conversions between emulsification and demulsification [216-220]. The switching process can be achieved by purging CO_2 or N_2 into the mixtures of oil, water, and surfactant formula [219, 221, 222], during which CO_2-responsive surfactants can be switched between protonated and deprotonated forms due to pH change. One notable advantage of using CO_2-responsive surfactants is that their switching trigger, CO_2 gas, is usually available onsite in the flue gas, which enables flue gas utilization to improve process sustainability. Indeed, CO_2-responsive surfactants have been considered as an important theme in

the context of carbon capture, utilization, and storage (CCUS) [55].

To design highly efficient CO_2-responsive surfactants for real application scenarios, it is of critical importance to understand their interfacial behaviors during both emulsification and demulsification processes. While it has been widely accepted that the ability to reduce the IFT significantly benefits the emulsification process, the demulsification mechanism of CO_2-responsive systems varies in literature due to different functions of CO_2-responsive surfactants [56, 219, 221, 223-227]. Based on previous experimental studies, three demulsification mechanisms arising from CO_2 purging have been proposed: I) Increased ionic strength [223, 224]: It has been reported that surfactants can be converted to dissolved salts after purging CO_2, leading to a dramatic increase in ionic strength of aqueous solution which can largely suppress the electrical double layer (EDL) of emulsion particles, reducing repulsion [227]; II) Decreased surfactant concentration [221, 225, 226]: In the presence of CO_2, the protonated surfactants carrying positive charges can bind to negative-charged surfactants through electrostatic interactions neutralizing some surfactants at the interfaces leading to increased IFT. III) Reduced interface activity [56, 219]: Certain acids and bases can form strong interface-active compounds to stabilize emulsions, while purging CO_2 into the solution can destabilize the emulsions by protonating acids to reduce surfactant interface activity. In particular, Lu *et al*. [228] developed a series of CO_2-responsive surfactants consisting of monoethanolamine (MEA) with long-chain fatty acids (LCFAs), which can not only stabilize O/W emulsion thanks to their low IFTs without CO_2, but also can achieve efficient demulsification as LCFAs become protonated by purging CO_2 into aqueous solution [229]. In addition, they designed two different protocols to distinguish the interfacial and solution switching processes of MEA-LCFA surfactants and concluded that the interfacial switching is weaker than solution switching, resulting in a much lower switching pH value. It was hypothesized

that the MEA and deprotonated LCFA pairing at the interface hinders the protonation of LCFA. While their work proposed a promising smart surfactant formula for efficient O/W emulsification and demulsification processes, the microscopic structural properties and interface hydration structures related to CO_2 switching mechanisms from molecular perspectives still remain unclear.

On the other hand, molecular dynamic (MD) simulation can provide important insights into the fundamental understanding about emulsification/demulsification processes in CO_2-responsive surfactant systems from atomic and molecular levels. Zhang *et al*. [230] used MD simulations to analyze the interfacial properties of dodecane-brine system containing dodecyl-N, N-dimethylacetamidinium (DMAA) with a slab model. They found that the protonated DMAA in the presence of CO_2 can greatly reduce IFT, which might be favorable for emulsifications. Liu *et al*. [231] performed MD simulations to investigate emulsification and demulsification processes of hexadecane-water systems induced by DMAA. They reported that the protonated DMAA can stabilize hexadecane-water emulsions in aqueous solution, while the removal of CO_2 leads to the oil-water separation. Sun *et al*. [232] studied demulsification behaviors of octane-in-water emulsions using cetyltrimethylammonium bromide (CTAB) and potassium phthalic acid (PPA) mixtures as emulsifiers by coarse-grained (CG) MD simulations. They found that demulsification takes place as pH increases due to the decrease in electrostatic repulsions among emulsion droplets. While these simulation studies have successfully illustrated some basic mechanisms in the CO_2-responsive surfactant systems, the role of CO_2 in these studies has been limited to the emulsification process only. However, the demulsification process using CO_2 as the trigger is more attractive from scientific and practical perspectives, since it is the highlight feature of CO_2-responsive surfactants which cannot be achieved by conventional non-switchable surfactants. To the best of our knowledge, MD simulation studies on the CO_2-responsive surfactant systems in

which CO_2 acts as a demulsification trigger have been rarely reported.

Therefore, in this work, we perform MD simulations to investigate emulsification and demulsification processes of O/W emulsions before and after purging CO_2 into an aqueous solution with lauric acids (LAs) at 300 K and 1 bar in relation to Lu *et al*. [56]. We use the deprotonated (DLA) and protonated lauric acid (PLA) to represent the cases before and after purging CO_2, respectively. Before purging CO_2, the systems can spontaneously form several stable O/W emulsion droplets due to high interface activity of DLA and strong electrostatic repulsion among negatively-charged emulsion droplets preventing coalescence. We find that all DLA molecules are distributed at the interfacial region with their hydrophobic tails extending into the oil phase and hydrophilic heads immersed in the water phase thanks to the electrostatic interaction with their counter-ions (*i.e.*, MEA in this work) and hydrogen bonding (H-bonding) with H_2O. After purging CO_2, demulsification takes place with emulsion droplets merging into one single droplet spontaneously, due to the protonation of LAs, which greatly suppresses the electrostatic repulsion between emulsion droplets and reduces the interface activity of LAs. While most PLAs still occupy the interfacial region, the H-bonding interaction between PLAs and water is weakened dramatically, resulting in a higher IFT. The potential mean force (PMF) calculations reveal a strong repulsion between the emulsion droplets arising from the long-range electrostatic interactions before purging CO_2, while the short-range entropic effect [233-235] dominates during the demulsification process after purging CO_2. Collectively, our work provides some important insights into the emulsification and demulsification mechanisms in CO_2-responsive surfactant systems which can assist the development of high-performance switchable surfactants and promote CO_2 utilization.

5.2 Molecular Model and Simulations

5.2.1 Molecular Models

In this work, we design two distinct systems consisting of normal heptane (nC_7), water (H_2O), LA, and MEA to study O/W emulsification and demulsification triggered by CO_2. Due to the limitation of computational capabilities, it is difficult to simulate emulsion droplets as large as several micrometers. Therefore, we use cubic simulation boxes with dimensions of ~11 nm × ~11 nm × ~11 nm in this work, resulting in microemulsions [231]. While droplet size might play a role, we hypothesize that the interfacial properties and emulsification/demulsification processes can still be captured by our simulations.

In each system, the nC_7-H_2O molar ratio is fixed at 1:80 as in Lu *et al*. [56], while varying number of LA and MEA molecules are added into the system corresponding to the oil/surfactant (O/S) ratio of 2.0, 1.5 and 1.0, resulting in six scenarios in total (**Scenario I**, **II**, and **III** for the cases before purging CO_2 as well as **Scenario IV**, **V**, and **VI** for the cases after purging CO_2). The surface concentration of surfactants ranges from ~1.4 to ~3.0 nm^{-2} which is in line with experimental measurements (~2.0 nm^{-2}) [56]. For each scenario, we apply 15 different initial configurations to minimize the effect of initial conditions. DLA is used to simulate the cases without CO_2, while its charge is balanced by MEA. On the other hand, we use PLA to study the effect of pH decrease arising from CO_2 injection. In addition, bicarbonate ions (HCO_3^-) are added into the solution to balance the total system charge. We note that as CO_2 solubility in H_2O at 1 bar is negligible [236], we do not explicitly consider the presence of CO_2. Instead, the CO_2 triggering mechanism is achieved by using different LAs according to pH conditions. In other words, in our simulation, we do not characterize the protonation/deprotonation processes of LA molecules, but rather study their interface structural properties and impacts on emulsification/demulsification

processes before/after purging CO_2. The molecular structures of DLA, nC_7, MEA, PLA, HCO_3^- and H_2O are shown in **Figure 5.1** and the number of fluid molecules in each scenario is listed in **Table 5.1.**

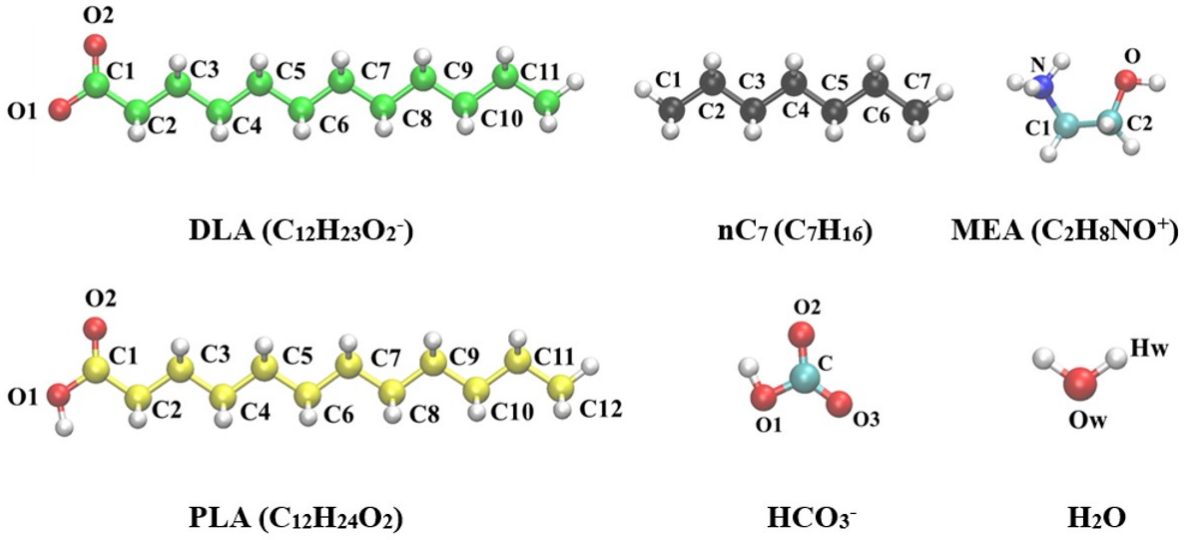

Figure 5.1 Molecular structures and formula of DLA, nC_7, MEA, PLA, HCO_3^- and H_2O. Color scheme: white, H; red, O; cyan, C of MEA; green, C of DLA; yellow, C of PLA; black, C of nC_7.

Table 5.1 Number of fluid molecules in each scenario

Scenario	Before/After Purging CO_2	O/S Ratio	nC_7	DLA	PLA	MEA	H_2O	HCO_3^-
I		2.0	450	225	-	225	36000	-
II	Before	1.5	450	300	-	300	36000	-
III		1.0	450	450	-	450	36000	-
IV		2.0	450	-	225	225	~35300	225
V	After	1.5	450	-	300	300	~35100	300
VI		1.0	450	-	450	450	~34600	450

5.2.2 Force Fields

The Lennard-Jones (LJ) and partial charge parameters of nC_7, LA, MEA and HCO_3^- are obtained from the CHARMM force field [237] and H_2O molecules are simulated by a modified TIP3P force field [238]. The CHARMM force field has shown an excellent performance in terms of oil-water interfacial behaviors [239, 240] and O/W emulsion properties [230, 241]. The non-bonded interactions between atoms are modeled as pairwise-additive potentials including Lennard-Jones (LJ) 12-6 and coulomb potentials,

$$V\left(r_{ij}\right)=4\varepsilon_{ij}\left[\left(\frac{\sigma_{ij}}{r_{ij}}\right)^{12}-\left(\frac{\sigma_{ij}}{r_{ij}}\right)^{6}\right]+\frac{q_i q_j}{4\pi\varepsilon_0 r_{ij}} \tag{5-1}$$

where r_{ij}, σ_{ij}, and ε_{ij}, q_i are the separation distance, LJ size, LJ well depth, and, the partial charge of atom i, respectively. LJ interactions between unlike atoms are obtained from the conventional Lorentz-Berthelot mixing rules [242, 243]. Lennard Jones (LJ) forces are modified to decay smoothly to zero between 1.0 and 1.2 nm [244]. The SETTLE algorithm [245] is used to constrain the bond length and angle of water molecules, while the LINCS algorithm [246] is applied to constrain the bond length for other molecules. The long-range electrostatic interactions are described by the particle-particle particle-mesh (PPPM) method [247] with a Fourier spacing of 0.12 and a 1.2 nm real-space cutoff. Three-dimensional periodic boundary conditions are applied and all the simulations are conducted by GROMACS [129] (version 2019.1) software package. All of the simulated snapshots are visualized by visual molecular dynamics (VMD) software [132].

5.2.3 Simulation Details

We calibrate the force fields by comparing various physical properties (*i.e.*, densities (pure nC_7 and LA) and IFT (nC_7-H_2O and LA-H_2O)) against available experimental data. Our calculation

shows a good agreement with experimental measurements in terms of fluid densities [248, 249] and nC_7-H_2O IFT [250] as shown in **Table C2.1** Gaussian fitting parameter of $P(\alpha)$ in **Scenario I**, **II**, and **III**

Scenario	A	μ	σ	CV
I	0.085	0.065	0.023	0.35
II	0.080	0.067	0.024	0.36
III	0.078	0.071	0.029	0.41

Table C.1. In terms of LA-H_2O IFT, the experimental data is 8.7 mN/m [251], while our simulation result is 15.39±0.36 mN/m. This might be because some LA molecules become protonated in experimental conditions (although the pH condition was not reported in Ref. [251]), while their interfacial concentrations are not available. Therefore, we conduct a few more simulations with varying the number of DLAs at the LA-H_2O interface and the IFT values are within a reasonable range compared to experimental data (see **Table C2.1** Gaussian fitting parameter of $P(\alpha)$ in **Scenario I**, **II**, and **III**

Scenario	A	μ	σ	CV
I	0.085	0.065	0.023	0.35
II	0.080	0.067	0.024	0.36
III	0.078	0.071	0.029	0.41

Table C.1).

For emulsification processes, nC_7, H_2O, and DLA molecules as well as MEAs are initially randomly placed in the simulation box. Then, *NPT* (i.e., fixed number of fluid molecules, constant

pressure, and constant temperature) ensemble simulation is carried out at 1 bar and 300 K for 1000 ns with a time step of 2 fs, followed by 60 ns production runs for data analysis. For demulsification processes, we graft H atoms to $-COO^-$ groups of DLAs in the final configurations of the emulsification processes to represent the protonation process induced by CO_2 purging. We perform 100-ns *NPT* simulations to achieve equilibrium followed by 60-ns production runs for data analysis. Finally, to investigate the emulsion stability, we select the typical emulsion droplets in different scenarios to calculate their PMF by using the umbrella sampling [252] as described in **C1** section.

5.3 Results and Discussion

In this section, we first analyze geometries and sizes of emulsion droplets as well as density profiles of each species within the given emulsion droplets before/after purging CO_2 into solution. Then, we calculate the PMF between emulsion droplets to illustrate their stability. In the end, we test one of the key hypotheses about the interface switching proposed in Lu *et al*. [56].

5.3.1 Before Purging CO_2

In **Figure 5.2**, we present the formation of O/W emulsion droplets and their evolutions before purging CO_2 for one specific initial configuration in **Scenario I**. We note that even with different initial configurations, the emulsification process is generally the same. The snapshots for **Scenario II** and **III** are shown in **Figure C.1** and **Figure C.2**, respectively. In general, DLA and nC_7 molecules aggregate spontaneously forming two or more stable O/W emulsion droplets with all DLA molecules at the interfaces (see DLA density distributions within the emulsion droplet later). We present the evolution of emulsion droplet number in each scenario in **Figure C.3**. nC_7 and DLA molecules are considered to be part of the same emulsion droplet if any of their C atoms are within 0.41 nm of each other [253]. The emulsion droplet number gradually decreases in all cases and finally stabilizes at ~600 ns. We note that after reaching equilibrium, a few loose oil or surfactant

molecules can be detached from the emulsion droplets (see in **Figure C.4**) and then re-merge into the droplets. The average emulsion droplet number (based on the trajectories between 600 ns and 1000 ns) for **Scenario I**, **II** and **III** are ~2.1, ~2.4 and ~3.3, respectively, indicating that a lower O/S ratio leads to more O/W emulsion droplets in the system. This is probably because the averaged surface concentration (SC) of surfactants in the emulsion droplets decreases from 2.7 nm^{-2} to 1.5 nm^{-2} as O/S ratio increases, which leads to the increase of the nC_7-H_2O IFT. Assuming the emulsion droplets as spherical ones (see **C2** section), SC can be determined by

$$\mathrm{SC} = \frac{N_s}{4\pi R_s^2} \tag{5-2}$$

where R_s and N_s represent the radius of emulsion droplets (which is analyzed in the later part) and the number of surfactants in each emulsion droplet, respectively. Furthermore, we study nC_7-H_2O IFT with various numbers of DLAs with MEA as counter-ions. We find that IFT decreases as DLA SC increases (see **Table C.2**).

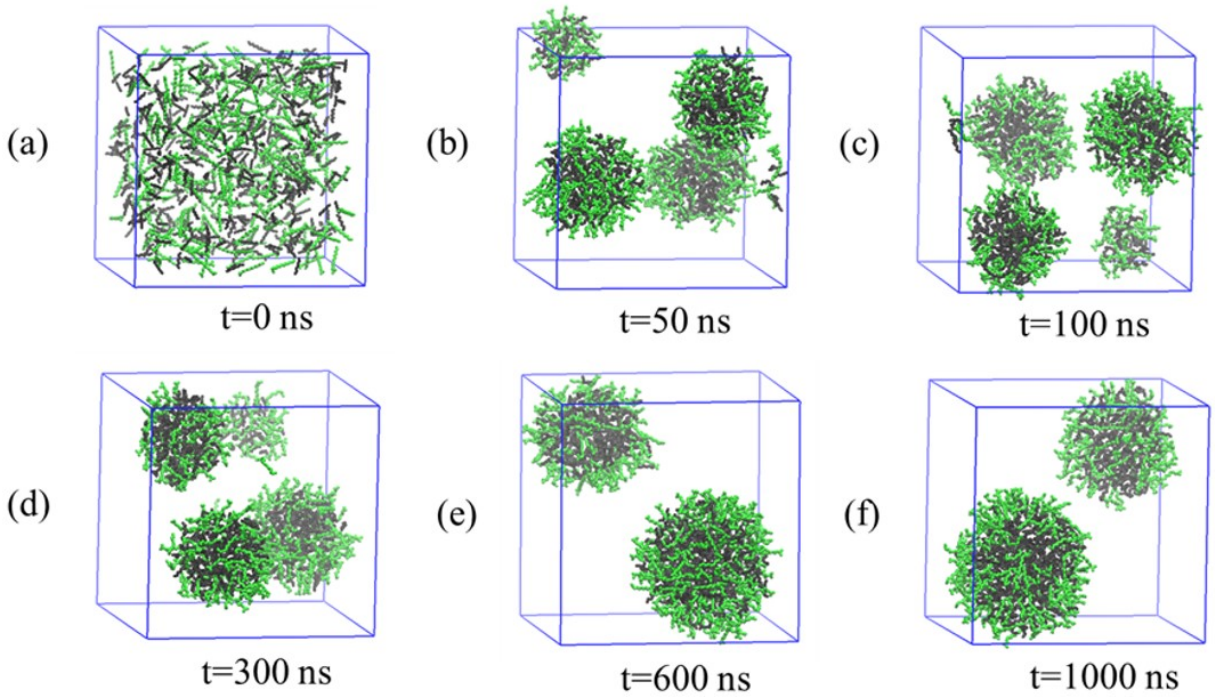

Figure 5.2 Formation of O/W emulsion droplets and their evolution (0, 50, 100, 300, 600, and 1000 ns) for one specific initial configuration in **Scenario I**. We use green and black colors to represent DLA and nC_7, respectively. For clarity, H_2O molecules and MEAs are not shown here.

For spherical emulsion droplets consisting of pure component, their radius R_s can be estimated based on the radius of gyration of that component, R_g, within the droplet [254-256],

$$R_s = \sqrt{\frac{5}{3}} R_g \tag{5-3}$$

In this work, we assume that this simple relation can still be applied to the emulsion droplets consisting of nC_7 and LA molecules, while we use an effective R_g^* of the mixture within a given emulsion droplet given as,

$$R_g^* = w_o \times R_{g,o} + w_{sf} \times R_{g,sf} \tag{5-4}$$

where the w_o and w_{sf} are the weight fraction of nC_7 and LA within the emulsion droplet, $R_{g,o}$ and $R_{g,sf}$ represent the radius gyrations of nC_7 and LA within the emulsion droplet, respectively. By combining Eqs. (4-3) and (4-4), we can obtain R_s which are used in this work. Then, the emulsion droplet radius probability distribution function $P(R_s)$ is given as

$$P(R_s) = \frac{\langle n(R_s) \rangle}{\langle N \rangle} \tag{5-5}$$

in which $\langle n(R_s) \rangle$ is the ensemble averaged number of emulsion droplets with their radius in the range from R_s to $R_s + dR_s$ and $\langle N \rangle$ is the ensemble averaged number of emulsion droplets in the system.

In **Figure 5.3**, we present $P(R_s)$ and the corresponding Gaussian fits (as discussed in **C2**) in **Scenario I**, **II**, and **III**. In addition, the Gaussian fit parameters are listed in **Table C.3**. As O/S ratio

decreases, CV gradually increases, while μ decreases, indicating a more dispersed $P(R_s)$ thanks to the formation of smaller emulsion droplets. Moreover, we also estimate the radius of emulsion droplets based on fluid density profiles (as discussed later): using the location where H_2O density is equal to 90% of its bulk density (the red dotted line in **Figure 5.4 (a)**) and the peak location of $O1_{DLA}$ distributions. We pick four different emulsion droplets in each scenario to calculate their sizes by using different methods as listed in **Table C.4**. It shows that the relative errors among different methods are generally small.

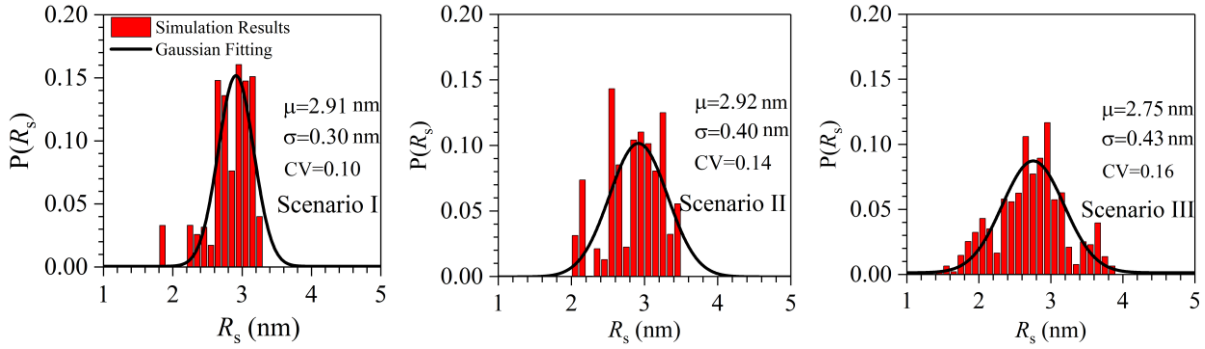

(a) (b) (c)

Figure 5.3 $P(R_s)$ and the corresponding Gaussian fitting in **Scenario** (a) **I**; (b) **II**; (b) **III**.

To investigate the structural properties of emulsion droplets, the number and charge density distributions of fluid molecules within a given emulsion droplet in **Scenario I** as a function of the radial distance from its COM are presented in **Figure 5.4**. The calculation details of the charge density profile can be referred to Ref. [244]. In addition, we also present one typical molecular configuration of the selected emulsion droplet and the surrounding water phase within 4.5 nm of the COM to ensure that the bulk water phase is reached by cleaving the emulsion droplet across its COM in **Figure 5.4(c)**. The R_s of the selected emulsion droplets in each scenario are close to the expected values of $P(R_s)$ shown in **Figure 5.3**. In fact, as shown in **Figure C.5**, R_s of the select emulsion droplet remains unchanged from 600 ns to 1060 ns indicating an excellent stability.

The similar number and charge density distributions in **Scenario II** and **Scenario III** are presented in **Figure C.6**.

We define the interfacial region based on the "90-90" criterion [257, 258], where the densities of nC_7 and H_2O are equal to 90% of their respective bulk densities. We find that all DLA molecules remain at the interfacial region with their COO^- groups facing the water phase while extending their hydrophobic tails toward the oil phase, in line with previous simulation study [259], which is also consistent with the hypothesis proposed in Lu *et al*. [56]. Due to the negative charge of DLA, MEA is also enriched at the interface, which is also observed in **Figure 5.4 (c)** where DLA and MEA molecules pair with each other. We note that there are a considerable number of COO^- groups in the water phase indicating a strong hydration around them. On the other hand, the charge distribution of emulsion droplets (including nC_7 and DLA) reveals a negative peak as shown in **Figure 5.4(b)** thanks to the negative-charged DLA head groups. The negatively charged emulsion droplet is helpful for preventing the coalescence of emulsion droplets and their stability as we discuss later. Interestingly, H_2O charge distribution generally has a positive peak in the interface region indicating that H_2O molecules have an ordered structure at the interface with their H atoms pointing towards the DLA molecules forming H-bonding, which is also reported in previous simulation work studying silica nanoparticles at oil/water interface [260].

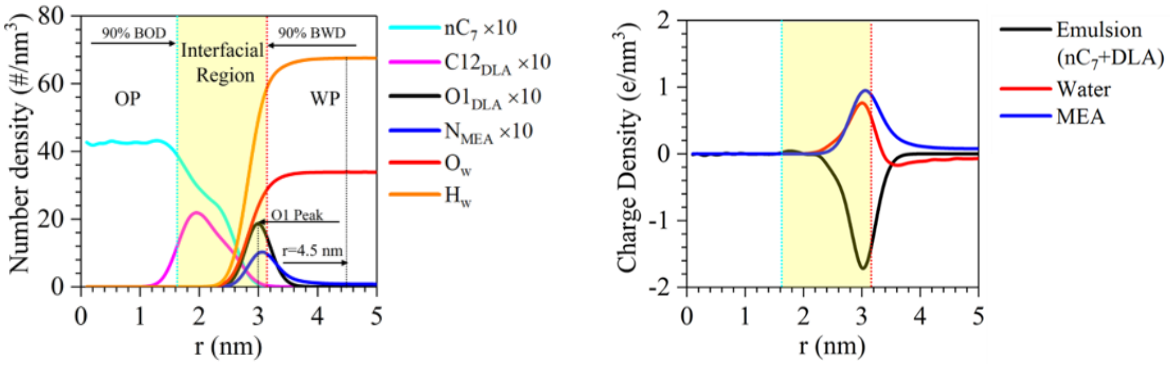

(a) (b)

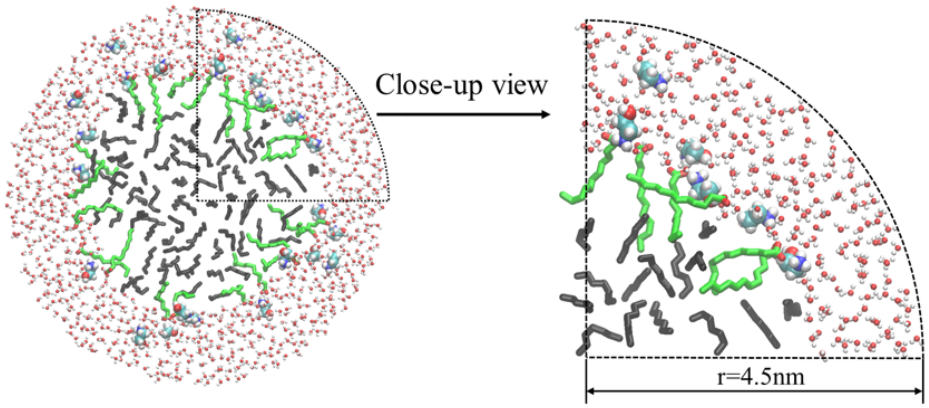

(c)

Figure 5.4 (a) Number density distribution; (b) Charge density distribution of different species within a given emulsion droplet with respect to its COM; (c) Typical molecular configuration of the select emulsion droplet and the surrounding water phase within 4.5 nm of COM of the emulsion droplet in **Scenario I**. OP, WP, BOD and BWD denote oil phase, water phase, bulk oil density and bulk water density, respectively. $C12_{DLA}$, $O1_{DLA}$ and N_{MEA} represent C12 atoms in DLA, O1 atoms in DLA and N atoms in MEA as shown in **Figure. 5.1**, respectively.

The averaged H-bonding number between DLA and H_2O per DLA molecule before purging CO_2 is listed in **Table C.5**. The hydrogen bond is recognized when the donor-acceptor distance is less than 0.35 nm and the angle between the vectors of donor-hydrogen and hydrogen-acceptor is less than 30° [261]. In general, each DLA molecule can form more than five H-bonding with the surrounding H_2O molecules. The high H-bonding number between DLA and H_2O can be attributed to the negative charge of emulsion droplets as well as the accumulation of MEA molecules at the interface which need to be hydrated by H_2O. Similar phenomenon is also observed in our previous study on hydration structures close to the negative-charged silica surface [262].

To better understand the hydration structures around DLA head groups, in **Figure 5.5(a)**, we present the corresponding spatial distribution functions (SDF) of Ow (O atom in H_2O) and N_{MEA}

(N atom in MEA) around the COO^- group of DLA in **Scenario I**. The DLA head group is strongly solvated by H_2O molecules with MEA surrounding it as well, which is line with the radial density distributions (RDDs) of $O1_{DLA}$-Ow and $O1_{DLA}$-N_{MEA} ($O1_{DLA}$ denotes the O1 atom in DLA; see **Figure 5.1**) as depicted in **Figure 5.5(b)**. The hydration number (HN) of Ow around the -COO^- groups can be obtained by integrating the $O1_{DLA}$-Ow RDD curve from $r = 0$ to the first peak as in Ref. [263], which can reflect the hydration ability of the head groups of DLA molecules. The HN values in different scenarios before purging CO_2 are listed in **Table C.6.** Generally, each COO^- group of DLA molecules can coordinate with ~3 water molecules before purging CO_2. The similar RDD distributions for **Scenario II** and **III** are observed in **Figure C.7**.

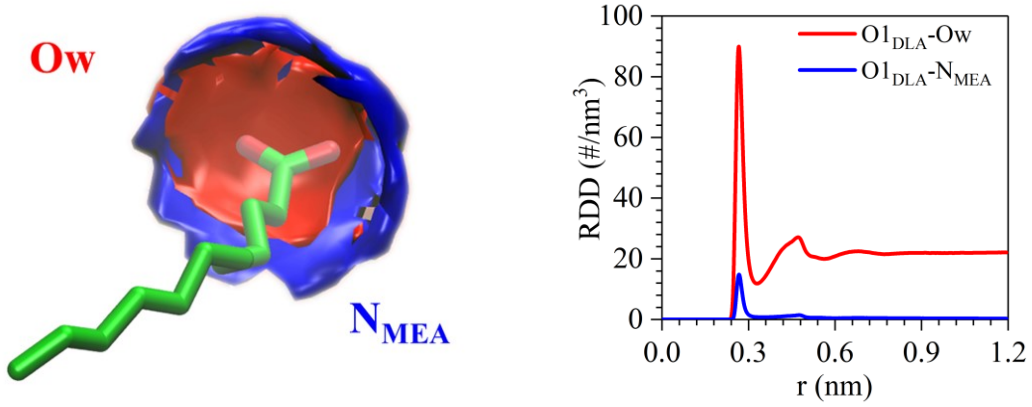

(a) (b)

Figure 5.5 (a) Spatial distribution function (SDF) of Ow (34/nm^3), N_{MEA} (5/nm^3) around -COO^- group of DLA; (b) Radial distribution density of Ow and N_{MEA} around $O1_{DLA}$ in **Scenario I.**

5.3.2 After purging CO_2

In **Figure 5.6**, we present the coalescence of O/W emulsion droplets and their evolutions after purging CO_2 into the solution for one specific initial configuration in **Scenario IV**. The snapshots for other scenarios are shown in **Figure C.8** and **Figure C.9**. The dispersed emulsion droplets gradually approach each other, then merge into a single big droplet in a relatively short period (<30

ns), suggesting an efficient demulsification process. Similar phenomena are observed for all other initial configurations in different scenarios. To determine the shape of the final droplet, the asymmetry parameter probability distributions $P(\alpha)$ and the corresponding Gaussian fittings in each scenario are presented in **Figure C.10.** Similar to the cases before purging CO_2, the expected values of Gaussian fittings are ~0.042 with CV values less than 0.5 (see **Table C.7**), indicating that all final droplets can be regarded to have a spherical shape. On the other hand, as shown in **Figure C.11**, the sizes of the final droplets conform to a single value with their $P(R_s)$ resembling the Dirac delta function (R_s obtained from Eq. (5-3)). The spontaneous emulsion droplet merging is partially aided by the increased nC_7-H_2O IFT after purging CO_2 as listed in **Table C.8**.

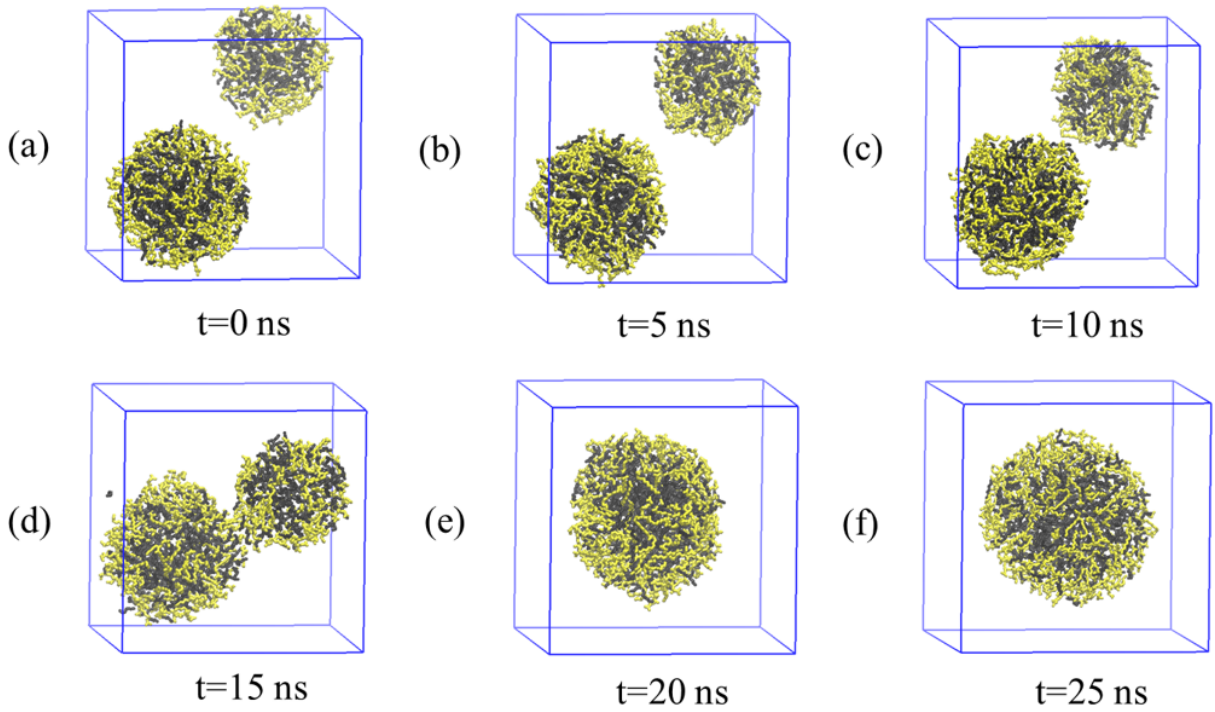

Figure 5.6 Coalescence of O/W emulsion droplets and their evolution (0, 5, 10, 15, 20, and 25 ns) for one specific initial configuration in **Scenario IV**. The yellow color represents PLA molecules, while nC_7 molecules are described by black color. For clarity, H_2O, MEA, and HCO_3^- are not shown here.

The density and charge distributions of different components after purging CO_2 for one select final droplet in **Scenario IV** is presented in **Figure 5.7** and the representative snapshots of emulsions and surrounding species within 4.5 nm of the COM is depicted as well. Similarly, as shown in **Figure C.12**, R_s of the select emulsion droplet remains unchanged for the last 60 ns-production stage demonstrating an excellent stability. In Lu *et al*., they proposed that after CO_2 bubbling, most PLA tend to dissolve into oil phase [56], which is different from our simulation observations. PLA molecules prefer to locate at the oil/water interface with the hydrophobic chains of the surfactants extended into the oil phase and hydrophilic heads pointing toward the water phase. In fact, PLA molecules can also form H-bonding with H_2O. However, as shown in **Table C.5**, the H-bonding number between PLA and H_2O is almost only half of that between DLA and H_2O. As a result, compared to **Figure 5.4(a)**, the head groups of PLA are a bit away from the water phase. Different from **Figure 5.4(b)**, the surface charge of emulsion droplets tends to be neutral after purging CO_2 as shown in **Figure 5.7(b)**, suggesting that the electrostatic repulsion is largely suppressed. The neutralization of emulsion surface might play an important role in breaking up the emulsions. At the same time, unlike the cases before purging CO_2, MEA molecules are depleted from the interface thanks to the neutralization of emulsion surface charge. The depletion of MEA from the nC_7-H_2O interface is also suggested by the SDF results and the disappearance of the peak in the $O1_{PLA}$-N_{MEA} RDD curves as demonstrated in **Figure 5.8(b).**

The SDF distributions of Ow around -COOH groups in PLA as depicted in **Figure 5.8(a)** also indicate that the hydration ability of LAs is significantly weakened after CO_2 purging, which is in line with the decreased HN number (see **Table C.6**) and the drastically-reduced first peak value in the RDD curves shown in **Figure 5.8(b).** As a result, H_2O forms much less ordered structure exhibiting tiny charge distribution peaks after purging CO_2 as shown in **Figure 5.7(b)**. The

decreased hydration ability is responsible for the reduction of the interfacial activity of the surfactant destroying the stability of the emulsions. We also notice that $O1_{PLA}$-$C_{HCO_3^-}$ presents a minor peak in the RDD curves compared to $O1_{PLA}$-N_{MEA}, which is corresponding to the local enrichment of $C_{HCO_3^-}$ (#5/nm^3) around -COOH group of PLA. It is probably because HCO_3^- can form more H-bonding with PLA than MEA. We present the averaged H-bonding number between PLA and HCO_3^-/MEA per PLA molecule in **Table C.9**. It shows that the H-bonding number between PLA and HCO_3^- is almost twice that between PLA and MEA.

Nevertheless, a small amount of the PLA molecules would dissolve into the oil phase as the surfactant/oil ratio increases when PLA molecules are oversaturated at the interface in **Scenario V** and **VI** after purging CO_2, although similar number and charge density distributions (see **Figure C.13**) and RDD distributions (see **Figure C.14**) are observed. Such results suggest that the surfactant depletion from the interface also plays a role during demulsification, especially when the SC of CO_2-responsive surfactants becomes higher.

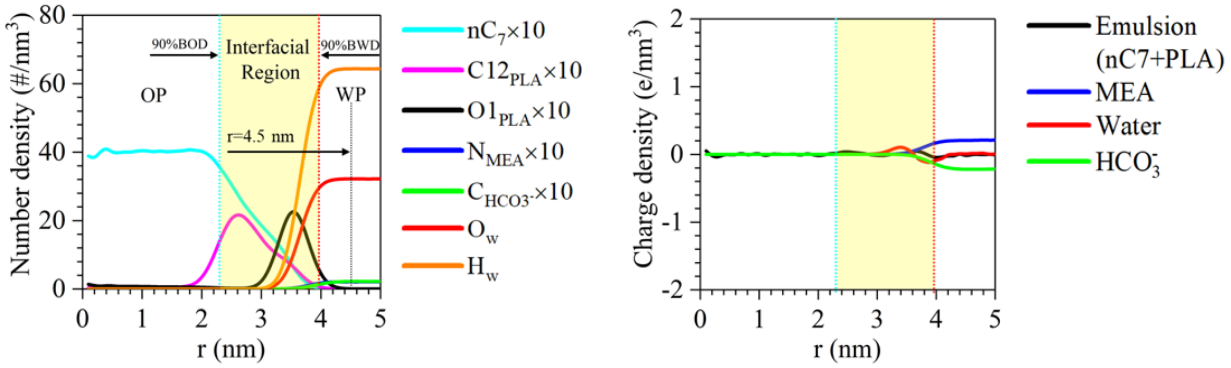

(a) (b)

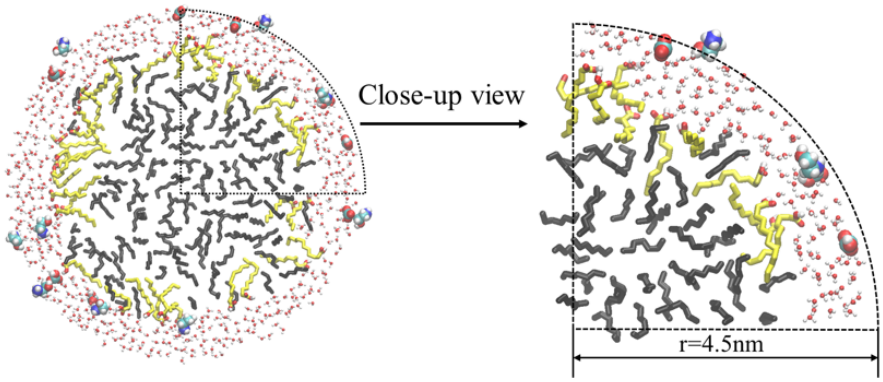

(c)

Figure 5.7 (a) Number density distribution; (b) Charge density distribution of different species within a given emulsion droplet with respect to its COM in **Scenario IV**. Typical molecular configuration of the select emulsion droplet and the surrounding water phase within 4.5 nm of COM of the emulsion droplet in **Scenario IV**. OP, WP, BOD and BWD denote oil phase, water phase, bulk oil density and bulk water density, respectively. $C12_{PLA}$, $O1_{PLA}$, N_{MEA}, $C_{HCO_3^-}$ represent C12 atoms in PLA, O1 atoms in PLA, N atoms in MEA and C atoms in HCO_3^- as shown in **Figure. 5.1**, respectively.

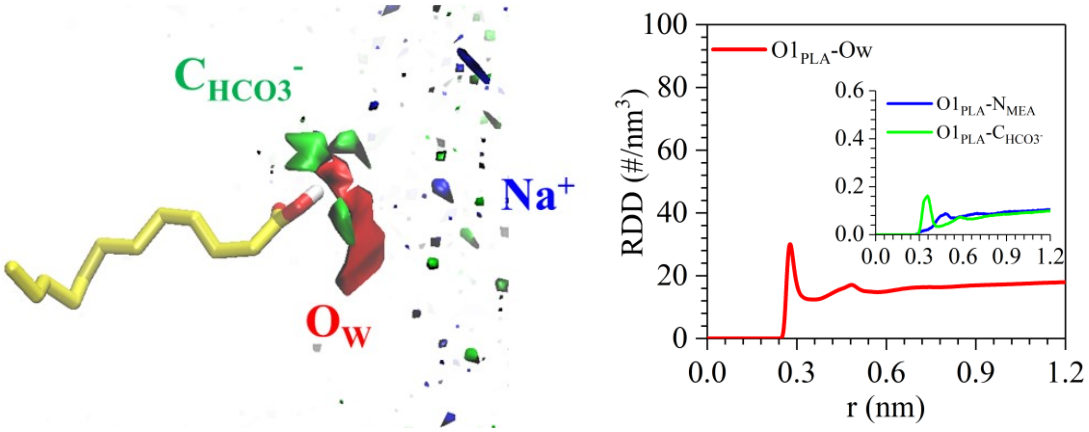

(a) (b)

Figure 5.8 (a) Spatial distribution function (SDF) of O_W (34/nm^3), N_{MEA} (5/nm^3), $C_{HCO_3^-}$ (#5/nm^3) around -COOH group of PLA; (b) Radial distribution density of Ow, N_{MEA} and $C_{HCO_3^-}$ around $O1_{PLA}$ in **Scenario IV**.

5.3.3 Assessment of Emulsion Stability by PMF

In this subsection, we use the PMF between emulsion droplets to assess their stability before/after purging CO_2 [264, 265]. PMF between the selected emulsion droplets with their radii close to the expected values from the Gaussian fitting in different scenarios is obtained by using the umbrella sampling method [80]. **Figure 5.9** shows the PMF between two emulsion droplets with respect to the reduced coordinates $(d-2R_s)/\sigma_w$ before/after purging CO_2, where σ_w donates the LJ size of Ow. Before purging CO_2, as two emulsion droplets approach each other, PMF renders a high potential energy barrier arising from the long-range electrostatic repulsion due to the same charges. Such a high potential energy barrier prevents the emulsion droplets from merging together, which is beneficial to their stability. However, after purging CO_2, the PMF curves display distinct behaviors due to the surface charge neutralization. There is no apparent potential energy barrier as the droplets approach each other and once their separation distance is less than σ_w, all systems exhibit a negative PMF, indicating that their aggregation is thermodynamically favorable due to the entropic effect [233-235]. The spontaneous aggregation is also in line with the coalescence process in **Figure 5.6.** These results clearly indicate that purging CO_2 can demulsify the emulsion droplets by protonating LAs, while these emulsion droplets can be stable before purging CO_2 [56].

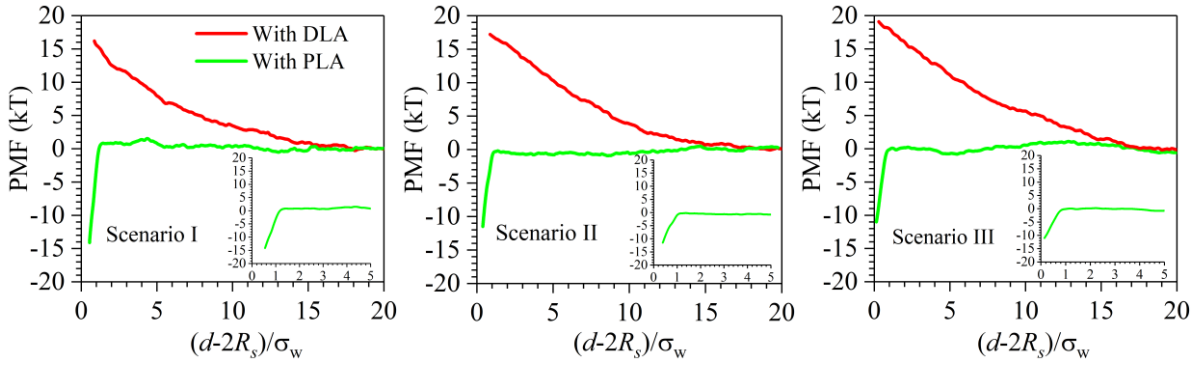

Figure 5.9 PMF between two selected emulsion droplets **Scenario** (a) **I**, (b) ***II*** and (c) ***III***. Green and red lines indicate the emulsion surface is covered with PLA and DLA, respectively.

In addition, Lu *et al*. proposed that the strong pairing between DLA and MEA account for the decreased interface switching pH [56]. To test this hypothesis, we calculate the PMF between the emulsion droplet with DLA at the interface and one single H_3O^+ balanced by Cl^- in different scenarios and investigate their distributions near the emulsion droplet (detailed discussion see **C3 section**). While the protonation of DLA is a chemical reaction, this result can partially explain whether H_3O^+ approach to the emulsion droplet is hindered or not. While our simulation reveals that DLA and MEA can form pairing at the interface as hypothesized in Lu *et al*. [56], it cannot prevent the adsorption of H_3O^+. Nevertheless, there is possible competitive adsorption between MEA and H_3O^+ at the interface. The role of counter-ions and additional salt ions in aqueous solution needs to be explored in future studies. In addition, the decreased surface pH mechanism proposed in Lu *et al*. [56] may be related to the dynamic chemical reaction processes which cannot be fully captured in our MD simulations. However, the interface structural properties and hydration structures revealed in this work may play an important role in the switching mechanisms of CO_2-responsive surfactant systems, which needs to be unlocked by the multi-disciplinary multi-scale quantum/statistical mechanical calculations.

5.4 Summary

In this work, we use MD simulations to explore the nC_7-H_2O emulsification and demulsification processes with LAs and MEA before/after purging CO_2. The shape, size and interfacial properties of emulsion droplets are investigated before/after purging CO_2. We find that before purging CO_2, the system can form a few O/W emulsion droplets which remain stable throughout the simulation, which is line with the experimental observations [56]. All DLA

molecules stay at nC_7-H_2O interface with their hydrophobic tails inserted into the oil phase and head groups pointing toward the water phase [259] leading to a negative-charged emulsion surface which can effectively stabilize the emulsion droplets via electrostatic repulsion. MEA molecules are also enriched at the interface by forming pairing with DLA head groups. In addition, H_2O has an ordered hydration structure near the interface [260] and forms a considerable number of H-bonding with DLA, which is also aided by the accumulation of MEA molecules at the interface.

After purging CO_2, all emulsion droplets merge into one big droplet spontaneously indicating an efficient demulsification process. While PLA molecules still prefer to stay at the nC_7-H_2O interface, the H-bonding number between PLA and H_2O is much smaller than that between DLA and H_2O, which leads to the increase in IFT. Consequently, the reduction of surfactant interfacial activity is considered as one of the main driving mechanisms of the demulsification process [56, 219], whereas the depletion of surfactants from the interface [266] also plays an important role at high surfactant surface concentration. Due to the protonation of $-COO^-$ groups in LAs, the surface charge of the emulsion droplet becomes neutral and MEA molecules are depleted from the interface. As a result, the electrostatic repulsion between emulsion droplets is greatly suppressed, which also contributes to the demulsification [214, 267].

PMF calculations between two emulsion droplets before purging CO_2 display a high potential energy barrier arising from the long-range electrostatic repulsion between two negatively charged emulsion droplets, which can explain the excellent emulsion stability. When DLA is deprotonated to become PLA, the potential energy barrier disappears and the PMF becomes negative if the emulsion droplets are close enough, resulting in the spontaneous aggregation. Such an attraction is due to the short-ranged entropic effect [233-235]. While our simulation observes strong DLA-MEA pairings at the interface, the PMF between emulsion droplet and H_3O^+ shows that the

presence of DLA-MEA pairs cannot prevent the H_3O^+ adsorption at the interface.

Collectively, our work unveils the structural and thermodynamic properties of O/W emulsion aided by CO_2-responsive surfactant formula before/after purging CO_2 and discloses the underlying mechanisms of emulsification and demulsification processes. While this work targets the LA-MEA system, the fundamental understanding from this work is helpful for design and optimization of CO_2-responsive surfactant system consisting of LCFAs-amine which has broad applications in effective CO_2 utilization.

However, in this work, we do not consider the salt effect on the CO_2-responsive surfactants. The formation water (so-called brine), which is ubiquitous in oil reservoirs, contains various mono-valent and di-valent ions (*e.g.*, Na^+, Ca^{2+}, CL^-, *etc.*) with the salinity up to 35 wt % [143]. Wu *et al*. [268] has shown that the like-charged colloid spheres can attract each other in the presence of di-valent ions. Obviously, such a counter-intuitive phenomenon may have important implications in emulsion stability. In addition, salt ion valence and concentration play an important role in surfactant functionalities [269, 270]. Therefore, it is worthwhile to investigate the robustness of CO_2-responsive surfactant formulas in the presence of various salt ions in future.

Chaper 6 Conclusions, Limitations and Future Plan

6.1 Conclusions

In this dissertation, the CO_2 competitive adsorption with water or hydrocarbon mixtures in different shale nanopores including organic and inorganic ones are carefully investigated by using molecular simulations, which provides important insights for the CO_2 geological sequestration and CO_2 enhanced gas recovery mechanism in shale reservoirs. Additionally, the interfacial properties at oil-water interface with CO_2-responsive surfactants are explored to reveal CO_2 responsive mechanism. The key findings and potential applications are summarized below:

1) The CO_2 adsorption capacity in different kaolinite nanopores varies depending on surface types and more CO_2 can be sequestrated in gibbsite nanopores. Based on this information, a more accurate estimation of CO_2 sequestration amount in kaolinite minerals can be predicted by taking the surface type effects into considerations.
2) The water exhibits distinct configurations (water film and bridge) in different kaolinite nanopores and it is proved to influence the subsequent CO_2 sequestration behaviors. Interestingly, it is not always the case that the presence of water reduces CO_2 storage amount while the enhancement also appears in siloxane mesopores when the pressure is low.
3) The siloxane surfaces gradually turn to a CO_2-wet ones as pressure increases indicating the wettability transition under different pressure conditions, which provides important insights for the prediction of capillary trapping capacity during CO_2 sequestration by using a pressure-dependent contact angle. In siloxane nanopores, the largest CO_2 density occur in the three-phase regions and the CO_2 presents a higher tendency to accumulate in two-phase regions. It is suggested to create larger three-phase and two-phase region areas to achieve a maximum CO_2 storage.

4) During primary production with pressure drawdown, the adsorbed lighter component is easily to be recovered while the heavier ones tend to be trapped inside nanopores. As a result, the pressure-driven recovery method is unfavorable for extracting heavier components, which requires further efforts to take them out.
5) CO_2 huff process present distinct differences in organic and inorganic nanopores. CO_2 can displace most of hydrocarbons from the surface in organic pores while all the hydrocarbons are totally depleted from surface area due to stronger interaction between CO_2 and negatively charged surfaces. It is indicated that the CO_2 huff can work better for the illite-rich shale gas reservoirs than kerogen-rich ones. The mechanisms of the CO_2 puff are similar to the pressure drawdown and it is not favorable for stripping the heavier hydrocarbons.
6) Before purging CO_2, the systems can spontaneously form several stable O/W emulsion droplets due to high interface activity of DLA and strong electrostatic repulsion among negatively-charged emulsion droplets preventing coalescence. After purging CO_2, demulsification takes place with emulsion droplets merging into one single droplet spontaneously, due to the protonation of LAs, which greatly suppresses the electrostatic repulsion between emulsion droplets and reduces the interface activity of LAs. In this regard, the switching mechanism are revealed by carefully analyzing the interfacial properties.
7) The potential mean force (PMF) calculations reveal a strong repulsion between the emulsion droplets arising from the long-range electrostatic interactions before purging CO_2, while the short-range entropic effect dominates during the demulsification process after purging CO_2. The PMF calculation is helpful for predicting and screening high-performance CO_2 responsive surfactants.

6.2 Limitations

In the work of **Chapter 3**, we use the pure water to investigate the moisture effects on CO_2 adsorption in kaolinite nanopores and do not consider the salt effect on the CO_2 sequestration. In addition, we only consider one possible water content in shale reservoirs while the water configurations depend on their concentrations [33], which would accordingly affect the subsequent CO_2 adsorption.

In the work of **Chapter 4**, we use the graphene model to represent the kerogen in shale reservoirs which is a very simplified model. The kerogen molecules developed by Ungerer et al. [271] based on the experimental indexes can reflect the realistic kerogen chemical structure which should be considered in the future work when studying kerogen. Moreover, in this work, we adopt a fixed illite model described by CLAYFF force field while the CLAYFF should be a flexible model allowing the free movement of surface atoms.

In the work of **Chapter 5**, we study the interfacial properties of O/W emulsion at the ambient conditions (300 K and 1bar) which is far away from the reservoir conditions with high temperature and pressure.

6.3 Future Works

1) The formation water usually contains various ions with the salinity up to 35 wt% [143] and the salt concentration is believed to have significant influences on CO_2 sequestration in shale nanopores [74]. Therefore, in the future, we plan to investigate the salt concentration effects on CO_2 adsorption. In addition, the water structure varies with the water content in nanopores, as a result, water concentration influences is also suggested to be studied in the future.
2) The kaolinite presents an electrically neutral surfaces without any counter-ions inside while other clay minerals such as montmorillonite and illite always carry negative charge due to the

isomorphous substitution, which is balanced by Na^+ or K^+. The charged surfaces is expected to result in distinct interfacial phenomena and significantly influence the distribution of the fluids. The CO_2 sequestration in these clay nanopores in the presence of water would be a very interesting work which is not well explored in previous work.

3) Most of the previous work focus on the CO_2 or water competitive adsorption with hydrocarbons while the study on three components co-adsorption is rarely reported. Thus, it is suggested to investigate the coexistence of CO_2-water-hydrocarbons in shale nanopores.
4) At present, the design and test of CO_2 responsive surfactants are only limited to the ambient conditions and deionized solutions which failed to match with the reservoir conditions with high pressure and temperature. The interfacial properties and robustness of systems need to be explored in the future.

Bibliography

[1] B. Franta, Early oil industry knowledge of CO_2 and global warming, Nature Climate Change 8(12) (2018) 1024-1025.

[2] T.J. Crowley, Causes of climate change over the past 1000 years, Science 289(5477) (2000) 270-277.

[3] W.G. Sunda, W.-J. Cai, Eutrophication induced CO_2-acidification of subsurface coastal waters: interactive effects of temperature, salinity, and atmospheric P_{CO2}, Environmental science & technology 46(19) (2012) 10651-10659.

[4] B. Ji, C. Liu, CO_2 improves the microalgal-bacterial granular sludge towards carbon-negative wastewater treatment, Water research 208 (2022) 117865.

[5] V. Iyakaremye, G. Zeng, G. Zhang, Changes in extreme temperature events over Africa under 1.5 and 2.0° C global warming scenarios, International Journal of Climatology 41(2) (2021) 1506-1524.

[6] S.C. Raper, R.J. Braithwaite, Low sea level rise projections from mountain glaciers and icecaps under global warming, Nature 439(7074) (2006) 311-313.

[7] J.M. Pandolfi, S.R. Connolly, D.J. Marshall, A.L. Cohen, Projecting coral reef futures under global warming and ocean acidification, science 333(6041) (2011) 418-422.

[8] M. Collins, S.-I. An, W. Cai, A. Ganachaud, E. Guilyardi, F.-F. Jin, M. Jochum, M. Lengaigne, S. Power, A. Timmermann, The impact of global warming on the tropical Pacific Ocean and El Niño, Nature Geoscience 3(6) (2010) 391-397.

[9] M.E. Boot-Handford, J.C. Abanades, E.J. Anthony, M.J. Blunt, S. Brandani, N. Mac Dowell, J.R. Fernández, M.-C. Ferrari, R. Gross, J.P. Hallett, Carbon capture and storage update, Energy & Environmental Science 7(1) (2014) 130-189.

[10] M. Bui, C.S. Adjiman, A. Bardow, E.J. Anthony, A. Boston, S. Brown, P.S. Fennell, S. Fuss, A. Galindo, L.A. Hackett, Carbon capture and storage (CCS): the way forward, Energy & Environmental Science 11(5) (2018) 1062-1176.

[11] S. Roussanaly, N. Berghout, T. Fout, M. Garcia, S. Gardarsdottir, S.M. Nazir, A. Ramirez, E.S. Rubin, Towards improved cost evaluation of Carbon Capture and Storage from industry, International Journal of Greenhouse Gas Control 106 (2021) 103263.

[12] T. Ajayi, J.S. Gomes, A. Bera, A review of CO_2 storage in geological formations emphasizing modeling, monitoring and capacity estimation approaches, Petroleum Science 16(5) (2019) 1028-1063.

[13] N. Spycher, K. Pruess, J. Ennis-King, CO_2-H_2O mixtures in the geological sequestration of CO_2. I. Assessment and calculation of mutual solubilities from 12 to 100 C and up to 600 bar, Geochimica et cosmochimica acta 67(16) (2003) 3015-3031.

[14] S. Bachu, CO_2 storage in geological media: Role, means, status and barriers to deployment, Progress in energy and combustion science 34(2) (2008) 254-273.

[15] S. Bachu, Sequestration of CO_2 in geological media: criteria and approach for site selection in response to climate change, Energy conversion and management 41(9) (2000) 953-970.

[16] P.N.K. De Silva, P. Ranjith, A study of methodologies for CO_2 storage capacity estimation of saline aquifers, Fuel 93 (2012) 13-27.

[17] S. Kumar, J. Foroozesh, K. Edlmann, M.G. Rezk, C.Y. Lim, A comprehensive review of value-added CO_2 sequestration in subsurface saline aquifers, Journal of Natural Gas Science and Engineering 81 (2020) 103437.

[18] M. Mukherjee, S. Misra, A review of experimental research on Enhanced Coal Bed Methane (ECBM) recovery via CO_2 sequestration, Earth-Science Reviews 179 (2018) 392-410.

[19] B. Metz, O. Davidson, H. De Coninck, M. Loos, L. Meyer, IPCC special report on carbon dioxide capture and storage, Cambridge: Cambridge University Press2005.

[20] Z. Li, M. Dong, S. Li, S. Huang, CO_2 sequestration in depleted oil and gas reservoirs—caprock characterization and storage capacity, Energy Conversion and Management 47(11-12) (2006) 1372-1382.

[21] X. Wu, Z. Ning, R. Qi, Q. Wang, L. Huang, Pore characterization and inner adsorption mechanism investigation for methane in organic and inorganic matters of shale, Energy Fuels 34(4) (2020) 4106-4115.

[22] K. Liu, M. Ostadhassan, J. Zhou, T. Gentzis, R. Rezaee, Nanoscale pore structure characterization of the Bakken shale in the USA, Fuel 209 (2017) 567-578.

[23] G. Chen, S. Lu, K. Liu, Q. Xue, C. Xu, S. Tian, J. Li, Y. Zhang, M. Tong, X. Pang, Investigation of pore size effects on adsorption behavior of shale gas, Mar. Pet. Geol. (2019).

[24] Z. Jin, A. Firoozabadi, Phase behavior and flow in shale nanopores from molecular simulations, Fluid Phase Equilib. 430 (2016) 156-168.

[25] J. Zhou, Z. Jin, K.H. Luo, Effects of Moisture Contents on Shale Gas Recovery and CO_2 Sequestration, Langmuir (2019).

[26] X. Tang, J. Zhang, X. Wang, B. Yu, W. Ding, J. Xiong, Y. Yang, L. Wang, C. Yang, Shale characteristics in the southeastern Ordos Basin, China: Implications for hydrocarbon accumulation conditions and the potential of continental shales, International Journal of Coal Geology 128 (2014) 32-46.

[27] H. Yu, J. Fan, J. Xia, H. Liu, H. Wu, Multiscale gas transport behavior in heterogeneous shale matrix consisting of organic and inorganic nanopores, J. Nat. Gas Sci. Eng. 75 (2020) 103139.

[28] W. Li, M. Zhang, Y. Nan, W. Pang, Z. Jin, Molecular Dynamics Study on CO_2 Storage in Water-Filled Kerogen Nanopores in Shale Reservoirs: Effects of Kerogen Maturity and Pore Size, Langmuir 37(1) (2020) 542-552.

[29] Z. Tao, J.M. Bielicki, A.F. Clarens, Physicochemical factors impacting CO_2 sequestration in depleted shale formations: The case of the Utica shale, Energy Procedia 63 (2014) 5153-5163.

[30] D.L. Bish, Rietveld refinement of the kaolinite structure at 1.5 K, Clays and Clay Minerals 41(6) (1993) 738-744.

[31] F.J. Huertas, L. Chou, R. Wollast, Mechanism of kaolinite dissolution at room temperature and pressure: Part 1. Surface speciation, Geochimica et Cosmochimica Acta 62(3) (1998) 417-431.

[32] C.M. Tenney, R.T. Cygan, Molecular simulation of carbon dioxide, brine, and clay mineral interactions and determination of contact angles, Environmental science & technology 48(3) (2014) 2035-2042.

[33] H. Xiong, D. Devegowda, L. Huang, Water bridges in clay nanopores: mechanisms of formation and impact on hydrocarbon transport, Langmuir 36(3) (2020) 723-733.

[34] Y. Hao, X. Jia, Z. Lu, D. Lu, P. Li, Water film or water bridge? Influence of self-generated electric field on coexisting patterns of water and methane in clay nanopores, Phys. Chem. C 123(36) (2019) 22656-22664.

[35] Q. Zhu, Developments on CO_2-utilization technologies, Clean Energy 3(2) (2019) 85-100.

[36] R. Safi, R.K. Agarwal, S. Banerjee, Numerical simulation and optimization of CO_2 utilization for enhanced oil recovery from depleted reservoirs, Chemical Engineering Science 144 (2016) 30-38.

[37] J.B. Curtis, Fractured shale-gas systems, AAPG bulletin 86(11) (2002) 1921-1938.

[38] C. Chen, M. Gu, Investigation of cyclic CO_2 huff-and-puff recovery in shale oil reservoirs using reservoir simulation and sensitivity analysis, Fuel 188 (2017) 102-111.

[39] X. Meng, Z. Meng, J. Ma, T. Wang, Performance Evaluation of CO_2 Huff-n-Puff Gas Injection in Shale Gas Condensate Reservoirs, Energies 12(1) (2019) 42.

[40] P. Nguyen, J.W. Carey, H.S. Viswanathan, M. Porter, Effectiveness of supercritical-CO_2 and N_2 huff-and-puff methods of enhanced oil recovery in shale fracture networks using microfluidic experiments, Appl. Energy 230 (2018) 160-174.

[41] H. Zhao, Z. Lai, A. Firoozabadi, Sorption hysteresis of light hydrocarbons and carbon dioxide in shale and kerogen, Sci. Rep. 7(1) (2017) 16209.

[42] Y. Wu, T. Fan, S. Jiang, X. Yang, H. Ding, M. Meng, D. Wei, Methane adsorption capacities of the lower paleozoic marine shales in the Yangtze Platform, South China, Energy Fuels 29(7) (2015) 4160-4167.

[43] D.H. Yaaton, Mineral composition of the average shale, Clay Minerals Bulletin 5(27) (1962) 31-36.

[44] S. Wang, Z. Song, T. Cao, X. Song, The methane sorption capacity of Paleozoic shales from the Sichuan Basin, China, Mar. Pet. Geol. 44 (2013) 112-119.

[45] F. Xiong, Z. Jiang, P. Li, X. Wang, H. Bi, Y. Li, Z. Wang, M.A. Amooie, M.R. Soltanian, J. Moortgat, Pore structure of transitional shales in the Ordos Basin, NW China: effects of composition on gas storage capacity, Fuel 206 (2017) 504-515.

[46] W.D. Keller, Clay minerals as influenced by environments of their formation, AAPG Bull. 40(11) (1956) 2689-2710.

[47] L. Huang, Z. Ning, Q. Wang, R. Qi, Y. Zeng, H. Qin, H. Ye, W. Zhang, Molecular simulation of adsorption behaviors of methane, carbon dioxide and their mixtures on kerogen: Effect of kerogen maturity and moisture content, Fuel 211 (2018) 159-172.

[48] F. Chen, S. Lu, X. Ding, Y. Ju, Evaluation of the density and thickness of adsorbed methane in differently sized pores contributed by various components in a shale gas reservoir: A case study of the Longmaxi Shale in Southeast Chongqing, China, Chem. Eng. J. 367 (2019) 123-138.

[49] F. Hao, H. Zou, Y. Lu, Mechanisms of shale gas storage: Implications for shale gas exploration in China, AAPG Bull. 97(8) (2013) 1325-1346.

[50] T. Zhang, G.S. Ellis, S.C. Ruppel, K. Milliken, R. Yang, Effect of organic-matter type and thermal maturity on methane adsorption in shale-gas systems, Org. Geochem. 47 (2012) 120-131.

[51] D.J. Ross, R.M. Bustin, The importance of shale composition and pore structure upon gas storage potential of shale gas reservoirs, Mar. Pet. Geol. 26(6) (2009) 916-927.

[52] L. Ji, T. Zhang, K.L. Milliken, J. Qu, X. Zhang, Experimental investigation of main controls to methane adsorption in clay-rich rocks, Appl. Geochem. 27(12) (2012) 2533-2545.

[53] M. Gasparik, A. Ghanizadeh, P. Bertier, Y. Gensterblum, S. Bouw, B.M. Krooss, High-pressure methane sorption isotherms of black shales from the Netherlands, Energy Fuels 26(8) (2012) 4995-5004.

[54] R.J. Hill, D.M. Jarvie, J. Zumberge, M. Henry, R.M. Pollastro, Oil and gas geochemistry and petroleum systems of the Fort Worth Basin, AAPG bulletin 91(4) (2007) 445-473.

[55] Z. Yang, C. He, H. Sui, L. He, X. Li, Recent advances of CO_2-responsive materials in separations, Journal of CO_2 Utilization 30 (2019) 79-99.

[56] Y. Lu, D. Sun, J. Ralston, Q. Liu, Z. Xu, CO_2-responsive surfactants with tunable switching pH, Journal of colloid and interface science 557 (2019) 185-195.

[57] L.W. Lake, Enhanced oil recovery, (1989).

[58] J.J. Sheng, Status of surfactant EOR technology, Petroleum 1(2) (2015) 97-105.

[59] O. Massarweh, A.S. Abushaikha, The use of surfactants in enhanced oil recovery: a review of recent advances, Energy Reports 6 (2020) 3150-3178.

[60] M.A. Ahmadi, Y. Arabsahebi, S.R. Shadizadeh, S.S. Behbahani, Preliminary evaluation of mulberry leaf-derived surfactant on interfacial tension in an oil-aqueous system: EOR application, Fuel 117 (2014) 749-755.

[61] Y. Lu, R. Li, R. Manica, Q. Liu, Z. Xu, Enhancing oil–solid and oil–water separation in heavy oil recovery by CO2-responsive surfactants, AIChE J. 67(1) (2021) e17033.

[62] W. Pu, C. Yuan, W. Hu, T. Tan, J. Hui, S. Zhao, S. Wang, Y. Tang, Effects of interfacial tension and emulsification on displacement efficiency in dilute surfactant flooding, RSC advances 6(56) (2016) 50640-50649.

[63] D. Liu, Z. Huang, Y. Suo, P. Zhu, J. Tan, H. Lu, CO_2-Responsive surfactant-free microemulsion, Langmuir 34(30) (2018) 8910-8916.

[64] E. Zio, Monte carlo simulation: The method, The Monte Carlo simulation method for system reliability and risk analysis, Springer2013, pp. 19-58.

[65] A. Hospital, J.R. Goñi, M. Orozco, J.L. Gelpí, Molecular dynamics simulations: advances and applications, Advances and applications in bioinformatics and chemistry: AABC 8 (2015) 37.

[66] E. Merzbacher, Quantum mechanics, Jones & Bartlett Publishers1961.

[67] J.W. Gibbs, Elementary principles in statistical mechanics: developed with especial reference to the rational foundations of thermodynamics, C. Scribner's sons1902.

[68] B.J. Leimkuhler, S. Reich, R.D. Skeel, Integration methods for molecular dynamics, Mathematical Approaches to biomolecular structure and dynamics, Springer1996, pp. 161-185.

[69] J. Hammersley, Monte carlo methods, Springer Science & Business Media2013.

[70] D. Frenkel, B. Smit, Understanding molecular simulation: from algorithms to applications, Elsevier2001.

[71] A. Sharma, S. Namsani, J.K. Singh, Molecular simulation of shale gas adsorption and diffusion in inorganic nanopores, Molecular Simulation 41(5-6) (2015) 414-422.

[72] Z. Xiang, D. Cao, J. Lan, W. Wang, D.P. Broom, Multiscale simulation and modelling of adsorptive processes for energy gas storage and carbon dioxide capture in porous coordination frameworks, Energy & Environmental Science 3(10) (2010) 1469-1487.

[73] Z. Jin, A. Firoozabadi, Methane and carbon dioxide adsorption in clay-like slit pores by Monte Carlo simulations, Fluid Phase Equilib. 360 (2013) 456-465.

[74] J. Zhou, Z. Jin, K.H. Luo, The role of brine in gas adsorption and dissolution in kerogen nanopores for enhanced gas recovery and CO_2 sequestration, Chemical Engineering Journal 399 (2020) 125704.

[75] J.I. Siepmann, D. Frenkel, Configurational bias Monte Carlo: a new sampling scheme for flexible chains, Molecular Physics 75(1) (1992) 59-70.

[76] H. Lorentz, Ueber die Anwendung des Satzes vom Virial in der kinetischen Theorie der Gase, Annalen der physik 248(1) (1881) 127-136.

[77] J.G. Kirkwood, E.M. Boggs, The radial distribution function in liquids, The Journal of Chemical Physics 10(6) (1942) 394-402.

[78] J. Ortega, J.P. Lewis, O.F. Sankey, First principles simulations of fluid water: The radial distribution functions, The Journal of chemical physics 106(9) (1997) 3696-3702.

[79] W. You, Z. Tang, C.-E.A. Chang, Potential mean force from umbrella sampling simulations: What can we learn and what is missed?, Journal of chemical theory and computation 15(4) (2019) 2433-2443.

[80] G.M. Torrie, J.P. Valleau, Nonphysical sampling distributions in Monte Carlo free-energy estimation: Umbrella sampling, Journal of Computational Physics 23(2) (1977) 187-199.

[81] N.K. Banavali, B. Roux, Free energy landscape of A-DNA to B-DNA conversion in aqueous solution, Journal of the American Chemical Society 127(18) (2005) 6866-6876.

[82] S. Wang, Y.-R. Lee, Y. Won, H. Kim, S.-E. Jeong, B.W. Hwang, A.R. Cho, J.-Y. Kim, Y.C. Park, H. Nam, Development of high-performance adsorbent using KOH-impregnated rice husk-based activated carbon for indoor CO_2 adsorption, Chem. Eng. J. (2022) 135378.

[83] S.A. Montzka, E.J. Dlugokencky, J.H. Butler, Non-CO_2 greenhouse gases and climate change, Nature 476(7358) (2011) 43-50.

[84] M. Possell, C. Nicholas Hewitt, D.J. Beerling, The effects of glacial atmospheric CO_2 concentrations and climate on isoprene emissions by vascular plants, Global Change Biology 11(1) (2005) 60-69.

[85] B. Verheggen, B. Strengers, J. Cook, R. van Dorland, K. Vringer, J. Peters, H. Visser, L. Meyer, Scientists' views about attribution of global warming, Environmental science & technology 48(16) (2014) 8963-8971.

[86] J.F. Mitchell, The "greenhouse" effect and climate change, Reviews of Geophysics 27(1) (1989) 115-139.

[87] T.P. Hughes, J.T. Kerry, A.H. Baird, S.R. Connolly, A. Dietzel, C.M. Eakin, S.F. Heron, A.S. Hoey, M.O. Hoogenboom, G. Liu, Global warming transforms coral reef assemblages, Nature 556(7702) (2018) 492-496.

[88] O. Ozotta, M. Ostadhassan, K. Liu, B. Liu, O. Kolawole, F. Hadavimoghaddam, Reassessment of CO_2 sequestration in tight reservoirs and associated formations, J. Pet. Sci. Eng. 206 (2021) 109071.

[89] R. Shukla, P. Ranjith, A. Haque, X. Choi, A review of studies on CO_2 sequestration and caprock integrity, Fuel 89(10) (2010) 2651-2664.

[90] A. Firoozabadi, P.C. Myint, Prospects for subsurface CO_2 sequestration, AIChE J. 56(6) (2010) 1398-1405.

[91] R. Yang, Q. Hu, S. He, F. Hao, X. Guo, J. Yi, X. He, Pore structure, wettability and tracer migration in four leading shale formations in the Middle Yangtze Platform, China, Mar. Pet. Geol. 89 (2018) 415-427.

[92] M. Sun, B. Yu, Q. Hu, R. Yang, Y. Zhang, B. Li, Pore connectivity and tracer migration of typical shales in south China, Fuel 203 (2017) 32-46.

[93] M.D. Aminu, S.A. Nabavi, C.A. Rochelle, V. Manovic, A review of developments in carbon dioxide storage, Appl. Energy 208 (2017) 1389-1419.

[94] R. Khosrokhavar, S. Griffiths, K.-H. Wolf, Shale gas formations and their potential for carbon storage: opportunities and outlook, Environmental Processes 1(4) (2014) 595-611.

[95] M. Zhang, S. Zhan, Z. Jin, Recovery mechanisms of hydrocarbon mixtures in organic and inorganic nanopores during pressure drawdown and CO_2 injection from molecular perspectives, Chem. Eng. J. 382 (2020) 122808.

[96] C. Liang, Z. Jiang, C. Zhang, L. Guo, Y. Yang, J. Li, The shale characteristics and shale gas exploration prospects of the Lower Silurian Longmaxi shale, Sichuan Basin, South China, J. Nat. Gas Sci. Eng. 21 (2014) 636-648.

[97] W. Ding, C. Li, C. Li, C. Xu, K. Jiu, W. Zeng, L. Wu, Fracture development in shale and its relationship to gas accumulation, Geoscience Frontiers 3(1) (2012) 97-105.

[98] C. Bousige, C.M. Ghimbeu, C. Vix-Guterl, A.E. Pomerantz, A. Suleimenova, G. Vaughan, G. Garbarino, M. Feygenson, C. Wildgruber, F.-J. Ulm, Realistic molecular model of kerogen's nanostructure, Nature materials 15(5) (2016) 576-582.

[99] W. Ding, D. Zhu, J. Cai, M. Gong, F. Chen, Analysis of the developmental characteristics and major regulating factors of fractures in marine–continental transitional shale-gas reservoirs: A case study of the Carboniferous–Permian strata in the southeastern Ordos Basin, central China, Mar. Pet. Geol. 45 (2013) 121-133.

[100] J. Xiong, X. Liu, L. Liang, Q. Zeng, Adsorption behavior of methane on kaolinite, Ind. Eng. Chem. Res. 56(21) (2017) 6229-6238.

[101] R. Šolc, M.H. Gerzabek, H. Lischka, D. Tunega, Wettability of kaolinite (001) surfaces—molecular dynamic study, Geoderma 169 (2011) 47-54.

[102] B. Pan, X. Yin, S. Iglauer, A review on clay wettability: From experimental investigations to molecular dynamics simulations, Advances in Colloid and Interface Science 285 (2020) 102266.

[103] W. Li, Y. Nan, Z. Zhang, Q. You, Z. Jin, Hydrophilicity/hydrophobicity driven CO_2 solubility in kaolinite nanopores in relation to carbon sequestration, Chemical Engineering Journal 398 (2020) 125449.

[104] R. Heller, M. Zoback, Adsorption of methane and carbon dioxide on gas shale and pure mineral samples, Journal of unconventional oil and gas resources 8 (2014) 14-24.

[105] Y.-H. Chen, D.-L. Lu, Amine modification on kaolinites to enhance CO_2 adsorption, Journal of colloid and interface science 436 (2014) 47-51.

[106] X. Du, D. Pang, Y. Zhao, Z. Hou, H. Wang, Y. Cheng, Investigation into the adsorption of CO_2, N_2 and CH_4 on kaolinite clay, Arabian Journal of Chemistry 15(3) (2022) 103665.

[107] Q. Wang, L. Huang, Molecular insight into competitive adsorption of methane and carbon dioxide in montmorillonite: Effect of clay structure and water content, Fuel 239 (2019) 32-43.

[108] Z. Jin, A. Firoozabadi, Effect of water on methane and carbon dioxide sorption in clay minerals by Monte Carlo simulations, Fluid Phase Equilib. 382 (2014) 10-20.

[109] W. Zhou, H. Wang, Y. Yan, X. Liu, Adsorption mechanism of CO_2/CH_4 in kaolinite clay: insight from molecular simulation, Energy Fuels 33(7) (2019) 6542-6551.

[110] X. Hu, H. Deng, C. Lu, Y. Tian, Z. Jin, Characterization of CO_2/CH_4 competitive adsorption in various clay minerals in relation to shale gas recovery from molecular simulation, Energy Fuels 33(9) (2019) 8202-8214.

[111] G. Kang, B. Zhang, T. Kang, J. Guo, G. Zhao, Effect of Pressure and Temperature on CO_2/CH_4 Competitive Adsorption on Kaolinite by Monte Carlo Simulations, Materials 13(12) (2020) 2851.

[112] Y. Liu, J. Hou, Selective adsorption of CO_2/CH_4 mixture on clay-rich shale using molecular simulations, Journal of CO_2 Utilization 39 (2020) 101143.

[113] Y. Ma, G. Lu, C. Shao, X. Li, Molecular dynamics simulation of hydrocarbon molecule adsorption on kaolinite (0 0 1) surface, Fuel 237 (2019) 989-1002.

[114] J. Lainé, Y. Foucaud, A. Bonilla-Petriciolet, M. Badawi, Molecular picture of the adsorption of phenol, toluene, carbon dioxide and water on kaolinite basal surfaces, Applied Surface Science 585 (2022) 152699.

[115] J. Rouquerol, D. Avnir, C. Fairbridge, D. Everett, J. Haynes, N. Pernicone, J. Ramsay, K. Sing, K. Unger, Recommendations for the characterization of porous solids (Technical Report), Pure and Applied Chemistry 66(8) (1994) 1739-1758.

[116] J. Fangzheng, Re-recognition of "unconventional" in unconventional oil and gas, Petroleum Exploration and Development 46(5) (2019) 847-855.

[117] G. Feng, Y. Zhu, S. Chen, Y. Wang, W. Ju, Y. Hu, Z. You, G.G. Wang, Supercritical methane adsorption on shale over wide pressure and temperature ranges: Implications for Gas-in-Place estimation, Energy Fuels 34(3) (2020) 3121-3134.

[118] R.T. Cygan, J.-J. Liang, A.G. Kalinichev, Molecular models of hydroxide, oxyhydroxide, and clay phases and the development of a general force field, The Journal of Physical Chemistry B 108(4) (2004) 1255-1266.

[119] F. Jiménez-Ángeles, A. Firoozabadi, Contact angle, liquid film, and liquid–liquid and liquid–solid interfaces in model oil–brine–substrate systems, Phys. Chem. C 120(22) (2016) 11910-11917.

[120] R. Shahsavari, R.J.-M. Pellenq, F.-J. Ulm, Empirical force fields for complex hydrated calcio-silicate layered materials, Physical Chemistry Chemical Physics 13(3) (2011) 1002-1011.

[121] J.J. Potoff, J.I. Siepmann, Vapor–liquid equilibria of mixtures containing alkanes, carbon dioxide, and nitrogen, AIChE J. 47(7) (2001) 1676-1682.

[122] G. Chen, S. Lu, K. Liu, T. Han, C. Xu, Q. Xue, B. Shen, Z. Guo, GCMC simulations on the adsorption mechanisms of CH_4 and CO_2 in K-illite and their implications for shale gas exploration and development, Fuel 224 (2018) 521-528.

[123] H.A. Lorentz, Ueber die Anwendung des Satzes vom Virial in der kinetischen Theorie der Gase, Ann. Phys. 248(1) (1881) 127-136.

[124] E. Pollock, J. Glosli, Comments on P3M, FMM, and the Ewald method for large periodic Coulombic systems, Computer Physics Communications 95(2-3) (1996) 93-110.

[125] M.G. Martin, MCCCS Towhee: a tool for Monte Carlo molecular simulation, Mol. Simul. 39(14-15) (2013) 1212-1222.

[126] B. Widom, Some topics in the theory of fluids, The Journal of Chemical Physics 39(11) (1963) 2808-2812.

[127] W.C. Swope, H.C. Andersen, A computer simulation method for the calculation of chemical potentials of liquids and solids using the bicanonical ensemble, The Journal of chemical physics 102(7) (1995) 2851-2863.

[128] P. Bai, J.I. Siepmann, Assessment and optimization of configurational-bias Monte Carlo particle swap strategies for simulations of water in the Gibbs ensemble, Journal of Chemical Theory and Computation 13(2) (2017) 431-440.

[129] D. Van Der Spoel, E. Lindahl, B. Hess, G. Groenhof, A.E. Mark, H.J. Berendsen, GROMACS: fast, flexible, and free, Journal of computational chemistry 26(16) (2005) 1701-1718.

[130] L. Chong, E.M. Myshakin, The effect of residual water content on preferential adsorption in carbon dioxide–methane–illite clay minerals: A molecular simulation study, Fluid Phase Equilib. 504 (2020) 112333.

[131] D.J. Evans, B.L. Holian, The nose–hoover thermostat, The Journal of chemical physics 83(8) (1985) 4069-4074.

[132] W. Humphrey, A. Dalke, K. Schulten, VMD: Visual molecular dynamics, Journal of Molecular Graphics 14(1) (1996) 33-38.

[133] J. Chen, F.-f. Min, L.-y. Liu, C.-f. Liu, Mechanism research on surface hydration of kaolinite, insights from DFT and MD simulations, Applied Surface Science 476 (2019) 6-15.

[134] X. Li, D.A. Ross, J.M. Trusler, G.C. Maitland, E.S. Boek, Molecular dynamics simulations of CO2 and brine interfacial tension at high temperatures and pressures, Phys. Chem. B 117(18) (2013) 5647-5652.

[135] E.A. Müller, A.s. Mejía, Resolving discrepancies in the measurements of the interfacial tension for the CO_2+H_2O mixture by computer simulation, The journal of physical chemistry letters 5(7) (2014) 1267-1271.

[136] J. Zhou, J. Zhang, J. Yang, Z. Jin, K.H. Luo, Mechanisms for kerogen wettability transition from water-wet to CO_2-wet: Implications for CO_2 sequestration, Chemical Engineering Journal 428 (2022) 132020.

[137] B. Pan, C. Gong, X. Wang, Y. Li, S. Iglauer, The interfacial properties of clay-coated quartz at reservoir conditions, Fuel 262 (2020) 116461.

[138] A.K. Giri, F. Teixeira, M.N.D. Cordeiro, Structure and kinetics of water in highly confined conditions: A molecular dynamics simulation study, Journal of Molecular Liquids 268 (2018) 625-636.

[139] J. Marti, G. Nagy, M. Gordillo, E. Guardia, Molecular simulation of liquid water confined inside graphite channels: Thermodynamics and structural properties, The Journal of chemical physics 124(9) (2006) 094703.

[140] J. Wang, Y. Zhu, J. Zhou, X.-H. Lu, Diameter and helicity effects on static properties of water molecules confined in carbon nanotubes, Physical Chemistry Chemical Physics 6(4) (2004) 829-835.

[141] S.R. da Rocha, K.P. Johnston, R.E. Westacott, P.J. Rossky, Molecular structure of the water− supercritical CO_2 interface, The Journal of Physical Chemistry B 105(48) (2001) 12092-12104.

[142] L. Liu, S.K. Bhatia, Molecular simulation of CO_2 adsorption in the presence of water in single-walled carbon nanotubes, The Journal of Physical Chemistry C 117(26) (2013) 13479-13491.

[143] S. Bachu, D.B. Bennion, Dependence of CO_2-brine interfacial tension on aquifer pressure, temperature and water salinity, Energy Procedia 1(1) (2009) 3157-3164.

[144] D.M. Jarvie, R.J. Hill, T.E. Ruble, R.M. Pollastro, Unconventional shale-gas systems: The Mississippian Barnett Shale of north-central Texas as one model for thermogenic shale-gas assessment, AAPG Bull. 91(4) (2007) 475-499.

[145] S.L. Montgomery, D.M. Jarvie, K.A. Bowker, R.M. Pollastro, Mississippian Barnett Shale, Fort Worth basin, north-central Texas: Gas-shale play with multi–trillion cubic foot potential, AAPG Bull. 89(2) (2005) 155-175.

[146] J. Yuan, D. Luo, L. Feng, A review of the technical and economic evaluation techniques for shale gas development, Applied Energy 148 (2015) 49-65.

[147] B. Lin, M. Chen, Y. Jin, H. Pang, Modeling pore size distribution of southern Sichuan shale gas reservoirs, J. Nat. Gas Sci. Eng. 26 (2015) 883-894.

[148] X.-C. Lu, F.-C. Li, A.T. Watson, Adsorption measurements in Devonian shales, Fuel 74(4) (1995) 599-603.

[149] Y. Sun, G. Zhang, S. Li, S. Jiang, CO_2/N_2 injection into $CH_4+C_3H_8$ hydrates for gas recovery and CO_2 sequestration, Chem. Eng. J. (2019) 121973.

[150] Z. Li, D. Elsworth, Controls of CO_2–N_2 gas flood ratios on enhanced shale gas recovery and ultimate CO_2 sequestration, J. Pet. Sci. Eng. 179 (2019) 1037-1045.

[151] X. Li, D. Elsworth, Geomechanics of CO_2 enhanced shale gas recovery, J. Nat. Gas Sci. Eng. 26 (2015) 1607-1619.

[152] M.O. Eshkalak, E.W. Al-Shalabi, A. Sanaei, U. Aybar, K. Sepehrnoori, Simulation study on the CO_2-driven enhanced gas recovery with sequestration versus the re-fracturing treatment of horizontal wells in the US unconventional shale reservoirs, J. Nat. Gas Sci. Eng. 21 (2014) 1015-1024.

[153] P. Zuloaga, W. Yu, J. Miao, K. Sepehrnoori, Performance evaluation of CO_2 Huff-n-Puff and continuous CO2 injection in tight oil reservoirs, Energy 134 (2017) 181-192.

[154] C. Song, D. Yang, Experimental and numerical evaluation of CO_2 huff-n-puff processes in Bakken formation, Fuel 190 (2017) 145-162.

[155] A. Abedini, F. Torabi, Oil recovery performance of immiscible and miscible CO_2 huff-and-puff processes, Energy Fuels 28(2) (2014) 774-784.

[156] F. Torabi, A.Q. Firouz, A. Kavousi, K. Asghari, Comparative evaluation of immiscible, near miscible and miscible CO_2 huff-n-puff to enhance oil recovery from a single matrix–fracture system (experimental and simulation studies), Fuel 93 (2012) 443-453.

[157] M. Heuchel, G. Davies, E. Buss, N. Seaton, Adsorption of carbon dioxide and methane and their mixtures on an activated carbon: simulation and experiment, Langmuir 15(25) (1999) 8695-8705.

[158] S. Ottiger, R. Pini, G. Storti, M. Mazzotti, Measuring and modeling the competitive adsorption of CO_2, CH_4, and N_2 on a dry coal, Langmuir 24(17) (2008) 9531-9540.

[159] A. Busch, Y. Gensterblum, B.M. Krooss, Methane and CO_2 sorption and desorption measurements on dry Argonne premium coals: pure components and mixtures, Int. J. Coal Geol. 55(2-4) (2003) 205-224.

[160] G. Zhao, C. Wang, Influence of CO_2 on the adsorption of CH_4 on shale using low-field nuclear magnetic resonance technique, Fuel 238 (2019) 51-58.

[161] J. Zhang, K. Liu, M. Clennell, D. Dewhurst, M. Pervukhina, Molecular simulation of CO_2–CH_4 competitive adsorption and induced coal swelling, Fuel 160 (2015) 309-317.

[162] F. Luo, R.-N. Xu, P.-X. Jiang, Numerical investigation of the influence of vertical permeability heterogeneity in stratified formation and of injection/production well perforation placement on CO_2 geological storage with enhanced CH_4 recovery, Appl. Energy 102 (2013) 1314-1323.

[163] Q. Yuan, X. Zhu, K. Lin, Y.-P. Zhao, Molecular dynamics simulations of the enhanced recovery of confined methane with carbon dioxide, Physical Chemistry Chemical Physics 17(47) (2015) 31887-31893.

[164] J. Zhou, Z. Jin, K.H. Luo, Effects of Moisture Contents on Shale Gas Recovery and CO_2 Sequestration, Langmuir 35(26) (2019) 8716-8725.

[165] K.A. Bulba, P.E. Krouskop, Compositional variety complicates processing plans for US shale gas, Oil Gas J. 107(10) (2009) 50-55.

[166] R. Reich, W.T. Ziegler, K.A. Rogers, Adsorption of methane, ethane, and ethylene gases and their binary and ternary mixtures and carbon dioxide on activated carbon at 212-301 K and pressures to 35 atmospheres, Industrial & engineering chemistry process design and development 19(3) (1980) 336-344.

[167] A.-L. Cheng, W.-L. Huang, Selective adsorption of hydrocarbon gases on clays and organic matter, Organic geochemistry 35(4) (2004) 413-423.

[168] C. Li, L. Li, T. Kang, Measurement and modeling of the adsorption isotherms of CH_4 and C_2H_6 on shale samples, RSC Adv. 9(24) (2019) 13705-13713.

[169] Y. Wang, T.T. Tsotsis, K. Jessen, Competitive sorption of methane/ethane mixtures on shale: measurements and modeling, Industrial & Engineering Chemistry Research 54(48) (2015) 12187-12195.

[170] Z. Tan, K.E. Gubbins, Selective adsorption of simple mixtures in slit pores: a model of methane-ethane mixtures in carbon, J. Phys. Chem. 96(2) (1992) 845-854.

[171] H. Wu, Y. He, R. Qiao, Recovery of multicomponent shale gas from single nanopores, Energy & Fuels 31(8) (2017) 7932-7940.

[172] T. Pitakbunkate, T. Blasingame, G. Moridis, P. Balbuena, Phase behavior of methane–ethane mixtures in nanopores, Ind. Eng. Chem. Res. 56(40) (2017) 11634-11643.

[173] K. Bui, I.Y. Akkutlu, Hydrocarbons Recovery From Model-Kerogen Nanopores, SPE J. 22(03) (2017) 854-862.

[174] G.P. Lithoxoos, A. Labropoulos, L.D. Peristeras, N. Kanellopoulos, J. Samios, I.G. Economou, Adsorption of N_2, CH_4, CO and CO_2 gases in single walled carbon nanotubes: A combined experimental and Monte Carlo molecular simulation study, J. Supercrit. Fluid 55(2) (2010) 510-523.

[175] Y. Liu, X. Ma, H.A. Li, J. Hou, Competitive adsorption behavior of hydrocarbon (s)/CO_2 mixtures in a double-nanopore system using molecular simulations, Fuel 252 (2019) 612-621.

[176] Y. Wang, Z. Jin, Effect of pore size distribution on hydrocarbon mixtures adsorption in shale nanoporous media from engineering density functional theory, Fuel 254 (2019) 115650.

[177] S. Baek, I.Y. Akkutlu, Produced-Fluid Composition Redistribution in Source Rocks for Hydrocarbon-In-Place and Thermodynamic Recovery Calculations, SPE J. 24 (2019) 1395-1414.

[178] S. Baek, I.Y. Akkutlu, CO_2 Stripping of Kerogen Condensates in Source Rocks, SPE J. 24 (2019) 1415-1434.

[179] T. Le, A. Striolo, D.R. Cole, CO_2–C_4H_{10} mixtures simulated in silica slit pores: relation between structure and dynamics, Phys. Chem. C 119(27) (2015) 15274-15284.

[180] Y. Tian, C. Yan, Z. Jin, Characterization of methane excess and absolute adsorption in various clay nanopores from molecular simulation, Sci. Rep. 7(1) (2017) 12040.

[181] J. Zhang, M.B. Clennell, K. Liu, M. Pervukhina, G. Chen, D.N. Dewhurst, Methane and carbon dioxide adsorption on Illite, Energy Fuels 30(12) (2016) 10643-10652.

[182] W. Zhou, H. Wang, Y. Yan, X. Liu, Adsorption mechanism of CO_2/CH_4 in kaolinite clay: insight from molecular simulation, Energy Fuels (2019).

[183] L. Chong, E.M. Myshakin, Molecular simulations of competitive adsorption of carbon dioxide–methane mixture on illitic clay surfaces, Fluid Phase Equilib. 472 (2018) 185-195.

[184] A. Afsharpoor, F. Javadpour, Liquid slip flow in a network of shale noncircular nanopores, Fuel 180 (2016) 580-590.

[185] S. Zhang, J. Yan, Q. Hu, J. Wang, T. Tian, J. Chao, M. Wang, Integrated NMR and FE-SEM methods for pore structure characterization of Shahejie shale from the Dongying Depression, Bohai Bay Basin, Mar. Pet. Geol. 100 (2019) 85-94.

[186] M.E. Curtis, B.J. Cardott, C.H. Sondergeld, C.S. Rai, Development of organic porosity in the Woodford Shale with increasing thermal maturity, Int. J. Coal Geol. 103 (2012) 26-31.

[187] W.A. Steele, The physical interaction of gases with crystalline solids: I. Gas-solid energies and properties of isolated adsorbed atoms, Surf. Sci. 36(1) (1973) 317-352.

[188] Y. Liu, H.A. Li, Y. Tian, Z. Jin, H. Deng, Determination of the absolute adsorption/desorption isotherms of CH_4 and n-C_4H_{10} on shale from a nano-scale perspective, Fuel 218 (2018) 67-77.

[189] W. Pang, Y. He, C. Yan, Z. Jin, Tackling the challenges in the estimation of methane absolute adsorption in kerogen nanoporous media from molecular and analytical approaches, Fuel 242 (2019) 687-698.

[190] M. Sweatman, N. Quirke, Modelling gas adsorption in slit-pores using Monte Carlo simulation, Mol. Simul. 27(5-6) (2001) 295-321.

[191] K. Refson, S.-H. Park, G. Sposito, Ab initio computational crystallography of 2: 1 clay minerals: 1. Pyrophyllite-1Tc, Phys. Chem. B 107(48) (2003) 13376-13383.

[192] J.H. Lee, S. Guggenheim, Single crystal X-ray refinement of pyrophyllite-1 Tc, Am. Miner. 66(3-4) (1981) 350-357.

[193] R. Wardle, G. Brindley, The crystal structures of pyrophyllite, 1Te, and of its dehydroxylate, American Mineralogist: Journal of Earth and Planetary Materials 57(5-6) (1972) 732-750.

[194] M.G. Martin, J.I. Siepmann, Transferable potentials for phase equilibria. 1. United-atom description of n-alkanes, Phys. Chem. B 102(14) (1998) 2569-2577.

[195] I.-C. Yeh, M.L. Berkowitz, Ewald summation for systems with slab geometry, The Journal of chemical physics 111(7) (1999) 3155-3162.

[196] J. Shelley, Boundary condition effects in simulations of water confined between planar walls, Molecular Physics 88(2) (1996) 385-398.

[197] J. Alejandre, D.J. Tildesley, G.A. Chapela, Molecular dynamics simulation of the orthobaric densities and surface tension of water, J. Chem. Phys. 102(11) (1995) 4574-4583.

[198] E. Spohr, Effect of electrostatic boundary conditions and system size on the interfacial properties of water and aqueous solutions, J. Chem. Phys. 107(16) (1997) 6342-6348.

[199] W. Humphrey, A. Dalke, K. Schulten, VMD: visual molecular dynamics, J. Mol. Graph. 14(1) (1996) 33-38.

[200] D.-Y. Peng, D.B. Robinson, A new two-constant equation of state, Industrial & Engineering Chemistry Fundamentals 15(1) (1976) 59-64.

[201] E. Hensen, T. Tambach, A. Bliek, B. Smit, Adsorption isotherms of water in Li–, Na–, and K–montmorillonite by molecular simulation, The Journal of Chemical Physics 115(7) (2001) 3322-3329.

[202] D. Frenkel, G. Mooij, B. Smit, Novel scheme to study structural and thermal properties of continuously deformable molecules, J. Phys.-Condes. Matter 4(12) (1992) 3053-3076.

[203] L. Lu, Q. Wang, Y. Liu, Adsorption and separation of ternary and quaternary mixtures of short linear alkanes in zeolites by molecular simulation, Langmuir 19(25) (2003) 10617-10623.

[204] S. Baek, I.Y. Akkutlu, CO_2 Stripping of Kerogen Condensates in Source Rocks, SPE J. 24 (2019) 1415-1434.

[205] A. Buckingham, R.-L. Disch, The quadrupole moment of the carbon dioxide molecule, Proc. Royal Soc. A 273(1353) (1963) 275-289.

[206] G. Sethia, R.S. Somani, H.C. Bajaj, Adsorption of carbon monoxide, methane and nitrogen on alkaline earth metal ion exchanged zeolite-X: structure, cation position and adsorption relationship, RSC Adv. 5(17) (2015) 12773-12781.

[207] A. Muggeridge, A. Cockin, K. Webb, H. Frampton, I. Collins, T. Moulds, P. Salino, Recovery rates, enhanced oil recovery and technological limits, Philosophical Transactions of the Royal Society A: Mathematical, Physical and Engineering Sciences 372(2006) (2014) 20120320.

[208] A.O. Gbadamosi, R. Junin, M.A. Manan, A. Agi, A.S. Yusuff, An overview of chemical enhanced oil recovery: recent advances and prospects, International Nano Letters 9(3) (2019) 171-202.

[209] H. Zhao, W. Kang, H. Yang, H. Zhang, T. Zhu, F. Wang, X. Li, B. Zhou, B. Sarsenbekuly, S. Aidarova, Imbibition enhancing oil recovery mechanism of the two surfactants, Physics of Fluids 32(4) (2020) 047103.

[210] D. Langevin, S. Poteau, I. Hénaut, J. Argillier, Crude oil emulsion properties and their application to heavy oil transportation, Oil & gas science and technology 59(5) (2004) 511-521.

[211] R. Zolfaghari, A. Fakhru'l-Razi, L.C. Abdullah, S.S. Elnashaie, A. Pendashteh, Demulsification techniques of water-in-oil and oil-in-water emulsions in petroleum industry, Separation and Purification Technology 170 (2016) 377-407.

[212] G. Shi, Y. Shen, P. Mu, Q. Wang, Y. Yang, S. Ma, J. Li, Effective separation of surfactant-stabilized crude oil-in-water emulsions by using waste brick powder-coated membranes under corrosive conditions, Green Chemistry 22(4) (2020) 1345-1352.

[213] R.K. Gupta, G.J. Dunderdale, M.W. England, A. Hozumi, Oil/water separation techniques: a review of recent progresses and future directions, Journal of Materials Chemistry A 5(31) (2017) 16025-16058.

[214] D. Wang, D. Yang, C. Huang, Y. Huang, D. Yang, H. Zhang, Q. Liu, T. Tang, M.G. El-Din, T. Kemppi, Stabilization mechanism and chemical demulsification of water-in-oil and oil-in-water emulsions in petroleum industry: A review, Fuel 286 (2021) 119390.

[215] Y. Lu, Y. Zhu, F. Yang, Z. Xu, Q. Liu, Advanced Switchable Molecules and Materials for Oil Recovery and Oily Waste Cleanup, Advanced Science (2021) 2004082.

[216] Y. Liu, P.G. Jessop, M. Cunningham, C.A. Eckert, C.L. Liotta, Switchable surfactants, Science 313(5789) (2006) 958-960.

[217] L.Q. Xu, B. Zhang, M. Sun, L. Hong, K.-G. Neoh, E.-T. Kang, G.D. Fu, CO_2-triggered fluorescence “turn-on” response of perylene diimide-containing poly (N, N-dimethylaminoethyl methacrylate), Journal of Materials Chemistry A 1(4) (2013) 1207-1212.

[218] J. Wang, M. Liang, Q. Tian, Y. Feng, H. Yin, G. Lu, CO_2-switchable foams stabilized by a long-chain viscoelastic surfactant, Journal of colloid and interface science 523 (2018) 65-74.

[219] P. Xu, Z. Wang, Z. Xu, J. Hao, D. Sun, Highly effective emulsification/demulsification with a CO2-switchable superamphiphile, Journal of colloid and interface science 480 (2016) 198-204.

[220] P. Brown, C.P. Butts, J. Eastoe, Stimuli-responsive surfactants, Soft Matter 9(8) (2013) 2365-2374.

[221] S. Dai, Y. Suo, D. Liu, P. Zhu, J. Zhao, J. Tan, H. Lu, Controllable CO_2-responsiveness of O/W emulsions by varying the alkane carbon number of a tertiary amine, Physical Chemistry Chemical Physics 20(16) (2018) 11285-11295.

[222] Y. Fan, Y. Zhang, X. Liu, K. Zhong, Z. Ge, Recovery and Recycling of CO_2/N_2-Switchable Anionic Surfactants in Emulsions, Journal of Surfactants and Detergents 20(6) (2017) 1301-1309.

[223] H. Li, Q. Li, J. Hao, Z. Xu, D. Sun, Preparation of CO_2-responsive emulsions with switchable hydrophobic tertiary amine, Colloids and Surfaces A: Physicochemical and Engineering Aspects 502 (2016) 107-113.

[224] X. Su, T. Robert, S.M. Mercer, C. Humphries, M.F. Cunningham, P.G. Jessop, A conventional surfactant becomes CO_2-responsive in the presence of switchable water additives, Chemistry–A European Journal 19(18) (2013) 5595-5601.

[225] H. Lu, D. Liu, B. Wang, D. Qing, Z. Huang, CO_2-switchable nanoemulsion based on N, N-dimethyl oleoaminde-propylamine (DOAPA) and sodium dodecyl sulphate (SDS), Journal of Dispersion Science and Technology 37(12) (2016) 1819-1825.

[226] D. Liu, Y. Suo, J. Tan, H. Lu, CO_2-Switchable microemulsion based on a pseudogemini surfactant, Soft Matter 13(20) (2017) 3783-3788.

[227] G. Rıos, C. Pazos, J. Coca, Destabilization of cutting oil emulsions using inorganic salts as coagulants, Colloids and Surfaces A: Physicochemical and Engineering Aspects 138(2-3) (1998) 383-389.

[228] P. Mignon, P. Ugliengo, M. Sodupe, E.R. Hernandez, Ab initio molecular dynamics study of the hydration of Li+, Na+ and K+ in a montmorillonite model. Influence of isomorphic substitution, Physical Chemistry Chemical Physics 12(3) (2010) 688-697.

[229] N. Shahidzadeh, D. Bonn, J. Meunier, M. Nabavi, M. Airiau, M. Morvan, Dynamics of spontaneous emulsification for fabrication of oil in water emulsions, Langmuir 16(25) (2000) 9703-9708.

[230] L. Zhang, X. Lu, X. Liu, Q. Li, Y. Cheng, Q. Hou, Molecular dynamics simulation of CO_2-switchable surfactant regulated reversible emulsification/demulsification processes of a dodecane–saline system, Physical Chemistry Chemical Physics 22(41) (2020) 23574-23585.

[231] X. Liu, Y. Li, S. Tian, H. Yan, Molecular dynamics simulation of emulsification/demulsification with a gas switchable surfactant, Phys. Chem. C 123(41) (2019) 25246-25254.

[232] X.-L. Sun, S.-S. Li, Z.-B. Liu, P. Wang, S. Pei, J. Zhang, Design of pH-responsive “on-off” emulsions using CTAB/PPA emulsifiers by simulations and experiments, Colloids and Surfaces A: Physicochemical and Engineering Aspects 533 (2017) 140-146.

[233] Z. Jin, J. Wu, Hybrid MC− DFT method for studying multidimensional entropic forces, The Journal of Physical Chemistry B 115(6) (2011) 1450-1460.

[234] M. Kinoshita, Spatial distribution of a depletion potential between a big solute of arbitrary geometry and a big sphere immersed in small spheres, The Journal of Chemical Physics 116(8) (2002) 3493-3501.

[235] S. Sacanna, W.T.M. Irvine, P.M. Chaikin, D.J. Pine, Lock and key colloids, Nature 464(7288) (2010) 575-578.

[236] Z. Duan, R. Sun, An improved model calculating CO_2 solubility in pure water and aqueous NaCl solutions from 273 to 533 K and from 0 to 2000 bar, Chemical geology 193(3-4) (2003) 257-271.

[237] J. Huang, A.D. MacKerell Jr, CHARMM36 all-atom additive protein force field: Validation based on comparison to NMR data, Journal of computational chemistry 34(25) (2013) 2135-2145.

[238] R. Pastor, A. MacKerell Jr, Development of the CHARMM force field for lipids, The journal of physical chemistry letters 2(13) (2011) 1526-1532.

[239] B. Qiao, W. Jiang, All-Atom Molecular Dynamics Study of Water–Dodecane Interface in the Presence of Octanol, The Journal of Physical Chemistry C 122(1) (2018) 687-693.

[240] P. Sun, K. Huang, H. Liu, Competitive Adsorption of Ions at the Oil–Water Interface: A Possible Mechanism Underlying the Separation Selectivity for Liquid–Liquid Solvent Extraction, Langmuir 34(44) (2018) 13155-13161.

[241] H. Miyamoto, D.M. Rein, K. Ueda, C. Yamane, Y. Cohen, Molecular dynamics simulation of cellulose-coated oil-in-water emulsions, Cellulose 24(7) (2017) 2699-2711.

[242] R.J. Good, C.J. Hope, New combining rule for intermolecular distances in intermolecular potential functions, The Journal of Chemical Physics 53(2) (1970) 540-543.

[243] D. Berthelot, Sur le mélange des gaz, Compt. Rendus 126 (1898) 1703-1706.

[244] Y. Nan, W. Li, Z. Jin, Role of Alcohol as a Cosurfactant at the Brine–Oil Interface under a Typical Reservoir Condition, Langmuir 36(19) (2020) 5198-5207.

[245] S. Miyamoto, P.A. Kollman, Settle: An analytical version of the SHAKE and RATTLE algorithm for rigid water models, Journal of computational chemistry 13(8) (1992) 952-962.

[246] B. Hess, H. Bekker, H.J. Berendsen, J.G. Fraaije, LINCS: a linear constraint solver for molecular simulations, Journal of computational chemistry 18(12) (1997) 1463-1472.

[247] R.W. Hockney, J.W. Eastwood, Computer simulation using particles, crc Press1988.

[248] M. Aralaguppi, C. Jadar, T. Aminabhavi, Density, refractive index, viscosity, and speed of sound in binary mixtures of cyclohexanone with hexane, heptane, octane, nonane, decane, dodecane, and 2, 2, 4-trimethylpentane, Journal of Chemical & Engineering Data 44(3) (1999) 435-440.

[249] H. Noureddini, B. Teoh, L. Davis Clements, Densities of vegetable oils and fatty acids, Journal of the American Oil Chemists' Society 69(12) (1992) 1184-1188.

[250] A.H. Demond, A.S. Lindner, Estimation of interfacial tension between organic liquids and water, Environmental science & technology 27(12) (1993) 2318-2331.

[251] A.T. Gros, R. Feuge, Surface and interfacial tensions, viscosities, and other physical properties of some n-aliphatic acids and their methyl and ethyl esters, Journal of the American Oil Chemists' Society 29(8) (1952) 313-317.

[252] J. Kästner, Umbrella sampling, Wiley Interdisciplinary Reviews: Computational Molecular Science 1(6) (2011) 932-942.

[253] S.A. Sanders, M. Sammalkorpi, A.Z. Panagiotopoulos, Atomistic simulations of micellization of sodium hexyl, heptyl, octyl, and nonyl sulfates, The Journal of Physical Chemistry B 116(8) (2012) 2430-2437.

[254] M.Y. Lobanov, N. Bogatyreva, O. Galzitskaya, Radius of gyration as an indicator of protein structure compactness, Molecular Biology 42(4) (2008) 623-628.

[255] C.D. Bruce, M.L. Berkowitz, L. Perera, M.D. Forbes, Molecular dynamics simulation of sodium dodecyl sulfate micelle in water: micellar structural characteristics and counterion distribution, The Journal of Physical Chemistry B 106(15) (2002) 3788-3793.

[256] S. Bogusz, R.M. Venable, R.W. Pastor, Molecular dynamics simulations of octyl glucoside micelles: structural properties, The Journal of Physical Chemistry B 104(23) (2000) 5462-5470.

[257] S. Zhan, Y. Su, Z. Jin, M. Zhang, W. Wang, Y. Hao, L. Li, Study of liquid-liquid two-phase flow in hydrophilic nanochannels by molecular simulations and theoretical modeling, Chem. Eng. J. 395 (2020) 125053.

[258] S.S. Jang, S.-T. Lin, P.K. Maiti, M. Blanco, W.A. Goddard, P. Shuler, Y. Tang, Molecular dynamics study of a surfactant-mediated decane− water interface: Effect of molecular architecture of alkyl benzene sulfonate, The Journal of Physical Chemistry B 108(32) (2004) 12130-12140.

[259] L.K. Holte, B.A. Kuran, G.L. Richmond, K.E. Johnson, Computational modeling of lauric acid at the organic–water interface, The Journal of Physical Chemistry C 118(19) (2014) 10024-10032.

[260] W. Li, Y. Nan, Q. You, Q. Xie, Z. Jin, Effects of salts and silica nanoparticles on oil-brine interfacial properties under hydrocarbon reservoir conditions: A molecular dynamics simulation study, Journal of Molecular Liquids 305 (2020) 112860.

[261] J. Padró, L. Saiz, E. Guardia, Hydrogen bonding in liquid alcohols: a computer simulation study, Journal of Molecular Structure 416(1-3) (1997) 243-248.

[262] W. Li, Y. Nan, Q. You, Z. Jin, CO_2 solubility in brine in silica nanopores in relation to geological CO_2 sequestration in tight formations: Effect of salinity and pH, Chemical Engineering Journal (2020) 127626.

[263] M. Zhang, H. Mao, Z. Jin, Molecular dynamic study on structural and dynamic properties of water, counter-ions and polyethylene glycols in Na-montmorillonite interlayers, Applied Surface Science 536 (2021) 147700.

[264] Y. Yang, L. Pan, F.C. Lightstone, K. Merz Jr, The role of molecular dynamics potential of mean force calculations in the investigation of enzyme catalysis, Methods in enzymology 577 (2016) 1-29.

[265] Y. Nan, W. Li, M. Zhang, Z. Jin, Ethanol Blending to Improve Reverse Micelle Dispersity in Supercritical CO_2: A Molecular Dynamics Study, The Journal of Physical Chemistry B (2021).

[266] D. Liu, Y. Suo, J. Tan, H. Lu, CO_2-Switchable microemulsion based on a pseudogemini surfactant, Soft Matter 13(20) (2017) 3783-3788.

[267] H. Sun, Q. Wang, X. Li, X. He, Novel polyether-polyquaternium copolymer as an effective reverse demulsifier for O/W emulsions: Demulsification performance and mechanism, Fuel 263 (2020) 116770.

[268] J. Wu, D. Bratko, J.M. Prausnitz, Interaction between like-charged colloidal spheres in electrolyte solutions, Proceedings of the National Academy of Sciences 95(26) (1998) 15169-15172.

[269] S. Maaref, S. Ayatollahi, The effect of brine salinity on water-in-oil emulsion stability through droplet size distribution analysis: a case study, Journal of Dispersion Science and Technology 39(5) (2018) 721-733.

[270] M. Al-Yaari, I. Hussein, A. Al-Sarkhi, M. Abbad, F. Chang, Effect of water salinity on surfactant-stabilized water–oil emulsions flow characteristics, Experimental Thermal and Fluid Science 64 (2015) 54-61.

[271] P. Ungerer, J. Collell, M. Yiannourakou, Molecular modeling of the volumetric and thermodynamic properties of kerogen: Influence of organic type and maturity, Energy & Fuels 29(1) (2015) 91-105.

[272] M. Parrinello, A. Rahman, Polymorphic transitions in single crystals: A new molecular dynamics method, Journal of Applied physics 52(12) (1981) 7182-7190.

[273] J.S. Hub, B.L. De Groot, D. Van Der Spoel, g_wham−A Free Weighted Histogram Analysis Implementation Including Robust Error and Autocorrelation Estimates, Journal of chemical theory and computation 6(12) (2010) 3713-3720.

[274] D. Tieleman, D. Van der Spoel, H. Berendsen, Molecular dynamics simulations of dodecylphosphocholine micelles at three different aggregate sizes: micellar structure and chain relaxation, The Journal of Physical Chemistry B 104(27) (2000) 6380-6388.

[275] D.T. Searls, The utilization of a known coefficient of variation in the estimation procedure, Journal of the American Statistical Association 59(308) (1964) 1225-1226.

[276] L.A. Asimow, M.M. Maxwell, Probability and statistics with applications: A problem solving text, Actex Publications2010.

[277] D.E. Sagnella, G.A. Voth, Structure and dynamics of hydronium in the ion channel gramicidin A, Biophysical journal 70(5) (1996) 2043-2051.

Appendix A

A1. Electric field calculation

We calculate the electric field inside siloxane nanopores devoid of any fluid by computing the electrostatic force on a test proton with charge *e*. The LJ parameter of the proton is set to 0 to make sure that only electrostatic forces are applied to the testing atoms. As shown in equation S1, the electrostatic force *F* is the product of the electric field *E* and the charge *e*

$$F = Ee, \tag{A-1}$$

Because we use a test atom with charge *e*, the electrostatic force is equal to the electric field. To obtain the position-dependent electric field, we moved the testing atoms from the bottom to the top surface of the pore and calculate the electric field at different Z positions.

A2. Analysis of energy local minimum of water bridge structure

In this part, we analyze the surface energy of the systems with different water configurations to illustrate the formation of water bridges arising from local minimum effects. Here, we assume that the water clusters have ideal geometry shape (cylinder, hemisphere and hemicylinder), while the line tension is not considered. In siloxane mesopores, it contains 880 water molecules. To simplify, we assume that the density of water is $1\ \mathrm{g/cm^3}$ and the total water volume is $V = 26.31\ \mathrm{nm^3}$.

Case I: If the water exists as a **cylinder** with generatrix vertical to surface with a radius of r_1 and the height of the cylinder is equal to the pore size $H = 4\ \mathrm{nm}$ as shown in **Figure A2.1**,

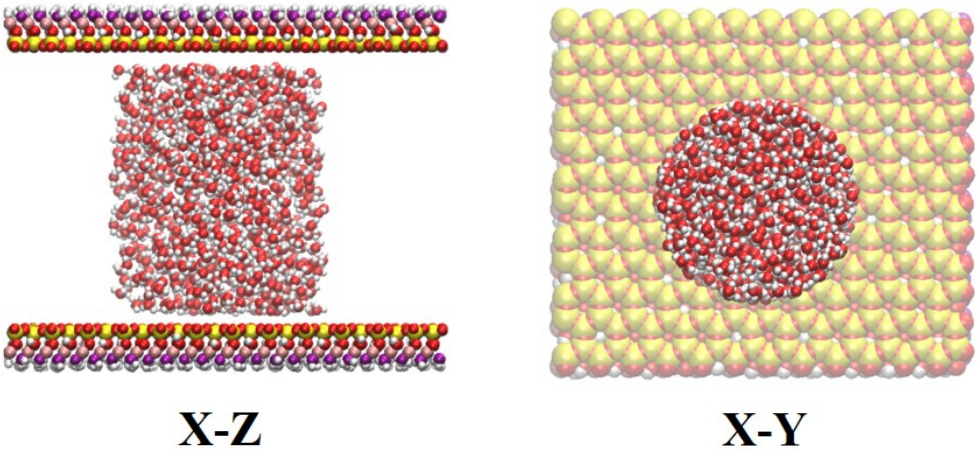

Figure A2.1. Schematic graph of the cylinder shape of water cluster in siloxane nanopore from the (a) *x-z*; (b) *x-y* plane view.

Then, we can get

$$\pi \times r_I^2 \times H = V, \tag{A-2}$$

then $r_I = 1.446$ nm, the gas-water surface area is $A_{VL}^I = 2 \times \pi \times r_I^2 \times H = 36.36$ nm^2, the top and bottom solid-water surface area is $\pi \times r_I^2 = 6.57$ nm^2, total liquid-solid area is $A_{LS}^I = 13.14$ nm^2.

Case II: If the water exists as the **hemisphere** with a radius of r_{II} as shown in **Figure A2.2**

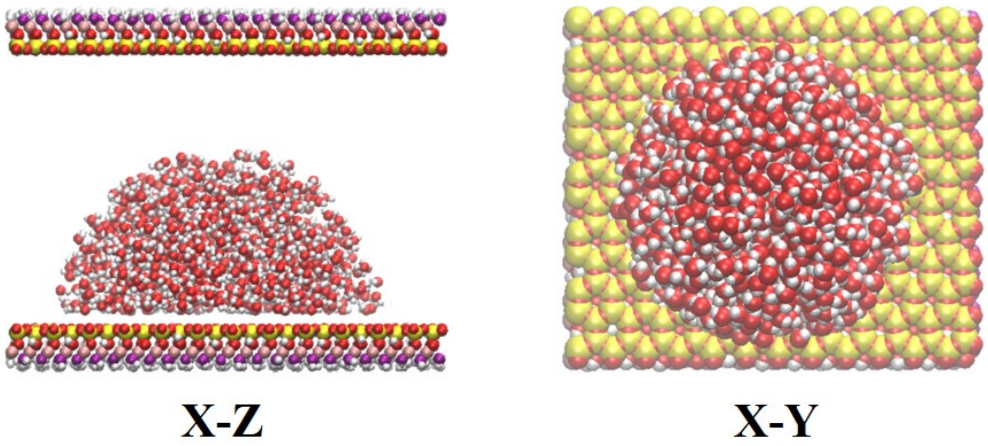

Figure A2.2 Schematic graph of the hemisphere shape of water cluster in siloxane nanopore from the (a) *x-z* and (b) *x-y* plane view.

then we can get

$$\frac{1}{2}\times\frac{4}{3}\times\pi\times r_{II}^3 = V\,, \tag{A-3}$$

then $r_{II} = 2.325$ nm the surface area is $\frac{1}{2}\times 4\times\pi\times r_{II}^2 = 33.96\ \text{nm}^2$, the solid-liquid area is $\pi\times r_{II}^2 = 16.98\ \text{nm}^2$.

Case III: If the water exists as the **hemi-cylinder** with generatrix parallel to surface (extending along y axis) with a radius of r_{III} as shown in **Figure A2.3**

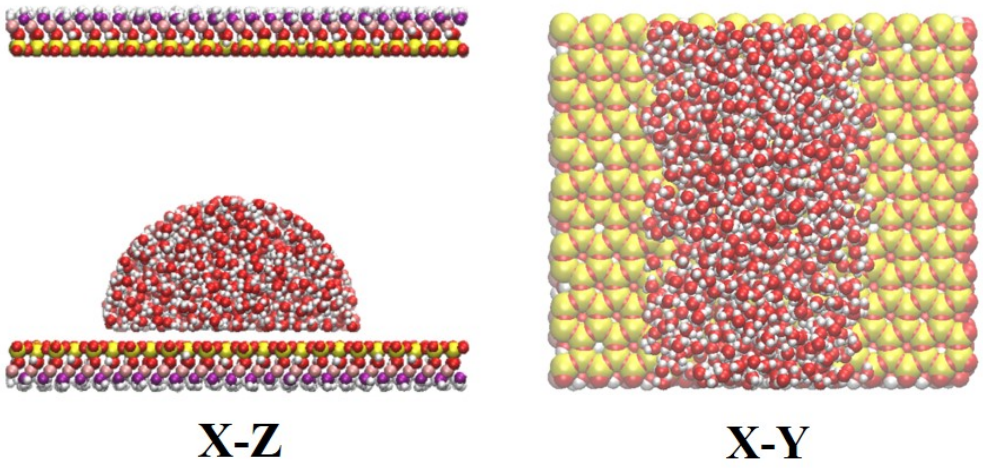

Figure A2.3 Schematic graph of the hemicylinder shape of water cluster in siloxane nanopore from the (a) *x-z* and (b) *x-y* plane view.

Then we can get

$$\frac{1}{2}\times\pi\times r_{III}^2\times L_y = V\,, \tag{A-4}$$

then $r_{III} = 1.767$ nm, the gas-water surface area is $\frac{1}{2}\times 2\times\pi\times r_{III}\times L_y = 29.78\ \text{nm}^2$, the solid-liquid area is $2\times r_{III}\times L_y = 18.96\ \text{nm}^2$

In summary, from **Case I** to **Case III**, vapor-liquid surface (*VL*) areas show the decline trend, while the liquid-solid (*LS*) surface areas increase. Accordingly, the vapor-solid (*VS*) surface areas will decrease due to the increase of liquid-solid surface areas. In the following, we would analyze

the surface energy change from **Case I** to other two cases. The total change of surface energy arises from the increase of *LS* surface area and decrease of *VS* and *VL* surface area.

$$\Delta E = \gamma_{LS}\Delta A_{LS} - \gamma_{VL}\Delta A_{\mathrm{VL}} - \gamma_{VS}\Delta A_{VS}, \tag{A-5}$$

The increment of *LS* surface area equals to the decrease of *VS* surface area

$$\Delta A_{LS} = \Delta A_{VS}, \tag{A-6}$$

Then we get

$$\Delta E = \gamma_{LS}\Delta A_{LS} - \gamma_{VL}\Delta A_{VL} - \gamma_{VS}\Delta A_{VS} = \Delta A_{LS}(\gamma_{LS} - \gamma_{VS}) - \gamma_{VL}\Delta A_{VL}, \tag{A-7}$$

Based on the three-phase contact angle equation, we know that

$$\gamma_{LS} = \gamma_{VS} + \gamma_{VL} \times \cos(180^{\circ} - \theta) \ \ (\theta > 90^{\circ}), \tag{A-8}$$

Then the change of surface energy turns into

$$\Delta E = \gamma_{VL} \times \cos(180 - \theta)\Delta A_{LS} - \gamma_{VL}\Delta A_{\mathrm{VL}} = \gamma_{VL} \times (\cos(180 - \theta)\Delta A_{LS} - \Delta A_{\mathrm{VL}}), \tag{A-9}$$

The water contact angle on siloxane surface is $\theta = 105^{\circ}$ when the surrounding is vacuum [101]

From **Case I** to **Case II**, ΔA_{LS} =3.84 nm^2, ΔA_{VL} =2.4 nm^2

$$\Delta E_{I-II} = \gamma_{VL} \times (3.84 \times \cos 75 - 2.4) = -1.41\gamma_{VL} < 0, \tag{A-10}$$

From **Case I** to **Case III**, $\Delta A_{LS} = 5.82$ nm^2, ΔA_{VL} =6.58nm^2

$$\Delta E_{I-III} = \gamma_{VL} \times (5.82 \times \cos 75 - 6.58) = -4.59\gamma_{VL} < 0, \tag{A-11}$$

While the θ value varies with different conditions, ΔE_{I-III} is always less than 0, which means that the water structure in **Case III** has the minimum surface energy. As a result, the water bridge structure in **Case I** should be a metastable state. In this work, the water is initially randomly distributed in the nanopores, and at the early stage the water bridge is preferably formed. Because the siloxane surfaces do not like water molecules driving water molecules to assemble into hemi-spherical ones on both sides of the kaolinite surfaces and finally the water clusters would connect

together to form water bridge structure. To covert the water bridge to other forms, firstly it would experience an intermediate conformation which needs overcome an energy barrier.

Let's suppose that the water bridge change from a cylinder shape to an intermediate configuration-circular conical frustum as shown in **Figure A2.4.** The radius of top and bottom plane on the cone is r_1 and r_2, and the height of the cone is $H = 4$ nm. The volume of circular conical frustum equals to

$$V = 1/3 \times \pi \times H \times (r_1^2 + r_1 r_2 + r_2^2) = 26.31 \text{ nm}^3, \tag{A-12}$$

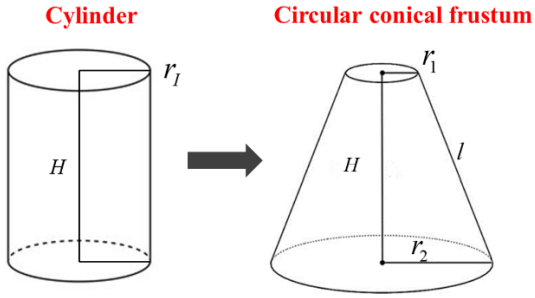

Figure A2.4. Schematic graph of the transformation of water cluster from cylinder to circular conical frustum.

We assume that radius of cylinder ($r_I = 1.446$ nm) on the top surface in **Case** I decrease to $r_1 = 1.20$ nm when it turns to the circular conical frustum. Based on eq (S-12), the radius of the cone on the bottom can be determined $r_2 = 1.68$ nm. The surface areas of liquid-solid interface increase to

$$\Delta A_{LS} = \pi \times (r_1^2 + r_2^2) - A_{LS}^I = 0.25 \text{ nm}^2, \tag{A-13}$$

Accordingly, surface areas of gas-solid interface decrease to

$$\Delta A_{VS} = \Delta A_{LS}, \tag{A-14}$$

The vapor-liquid surface areas increase to

$$\Delta A_{\text{VL}} = \pi \times (r_1 + r_2) \times l - A_{VL}^I, \tag{A-15}$$

where $l = \sqrt{(H^2 + (r_2^2 - r_1^2))}$

Total surface energy change (increase of *LS*, *VL* surfaces and decrease of *VS* surfaces)

$$\Delta E = \gamma_{LS}\Delta A_{LS} + \gamma_{VL}\Delta A_{VL} - \gamma_{VS}\Delta A_{VS} = \Delta A_{LS}(\gamma_{LS} - \gamma_{VS}) + \gamma_{VL}\Delta A_{VL}, \quad \text{(A-16)}$$

Then the change of surface energy turns into

$$\Delta E = \gamma_{LS}\Delta A_{LS} + \gamma_{VL}\Delta A_{VL} - \gamma_{VS}\Delta A_{VS} = \Delta A_{LS}(\gamma_{LS} - \gamma_{VS}) + \gamma_{VL}\Delta A_{VL}, \quad \text{(A-17)}$$

Combine with eq(A-8)

$$\Delta E = \gamma_{VL} \times \cos(180 - \theta)\Delta A_{LS} + \gamma_{VL}\Delta A_{\mathrm{VL}} = \gamma_{VL} \times (\cos(180 - \theta)\Delta A_{LS} + \Delta A_{\mathrm{VL}}) > 0, \quad \text{(A-18)}$$

We can see that ΔE always has a positive value. Therefore, it is unfavorable to transform into the intermediate state once the water bridge is initially formed resulting in a local energy minimum.

Table A.1 Shape factor ($\lambda = \frac{R_s}{R_m}$) values for water clusters at different conditions.

λ	5 MPa	10 MPa	15 MPa	20 MPa
Siloxane Mesopore	1.15	1.23	1.70	1.71
Siloxane Micropore	1.13	1.13	1.13	1.15

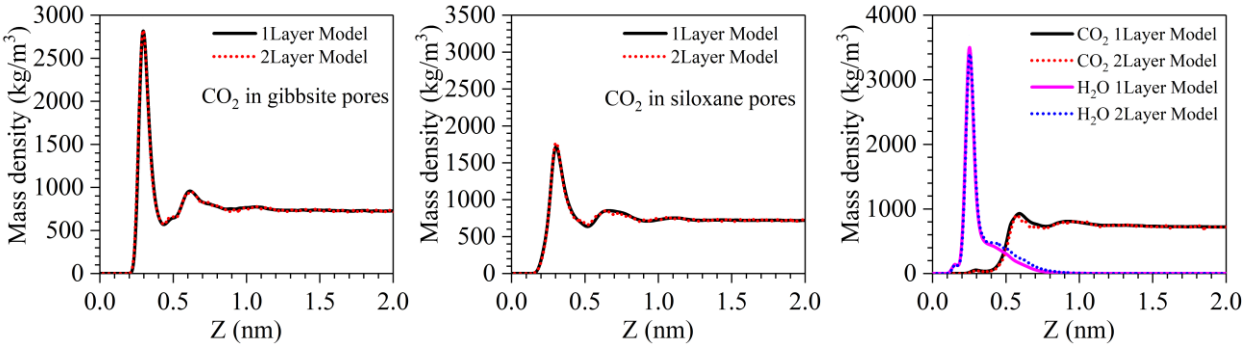

Figure A.1 CO_2 density profile in (a) gibbsite; (b) siloxane kaolinite mesopores in **Scenario I** and (c) CO_2 and water density profiles in gibbsite kaolinite mesopores in **Scenario II** at 20 MPa and 333.15 K.

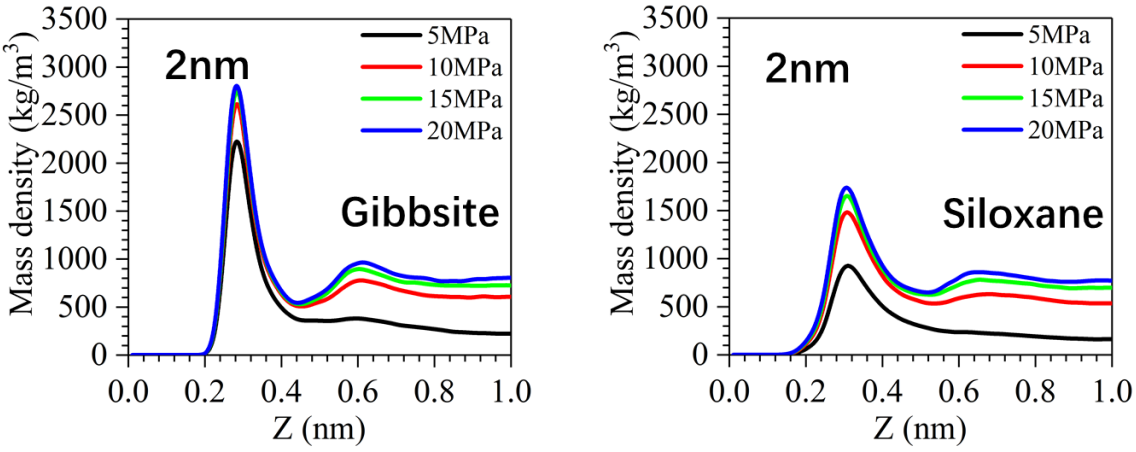

(a) (b)

Figure A.2 CO_2 density profile in (a) gibbsite; (b) siloxane kaolinite micropores under different pressure conditions at 333.15 K.

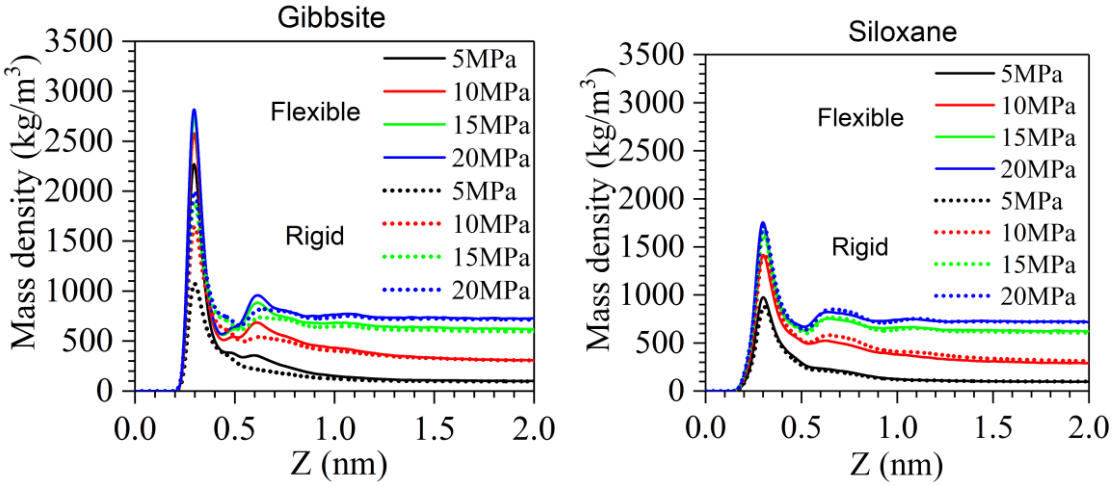

(a) (b)

Figure A.3 CO_2 density profile in (a) gibbsite; (b) siloxane kaolinite mesopores under different pressure conditions at 333.15 K using rigid (dotted line) and flexible (solid line) clay models.

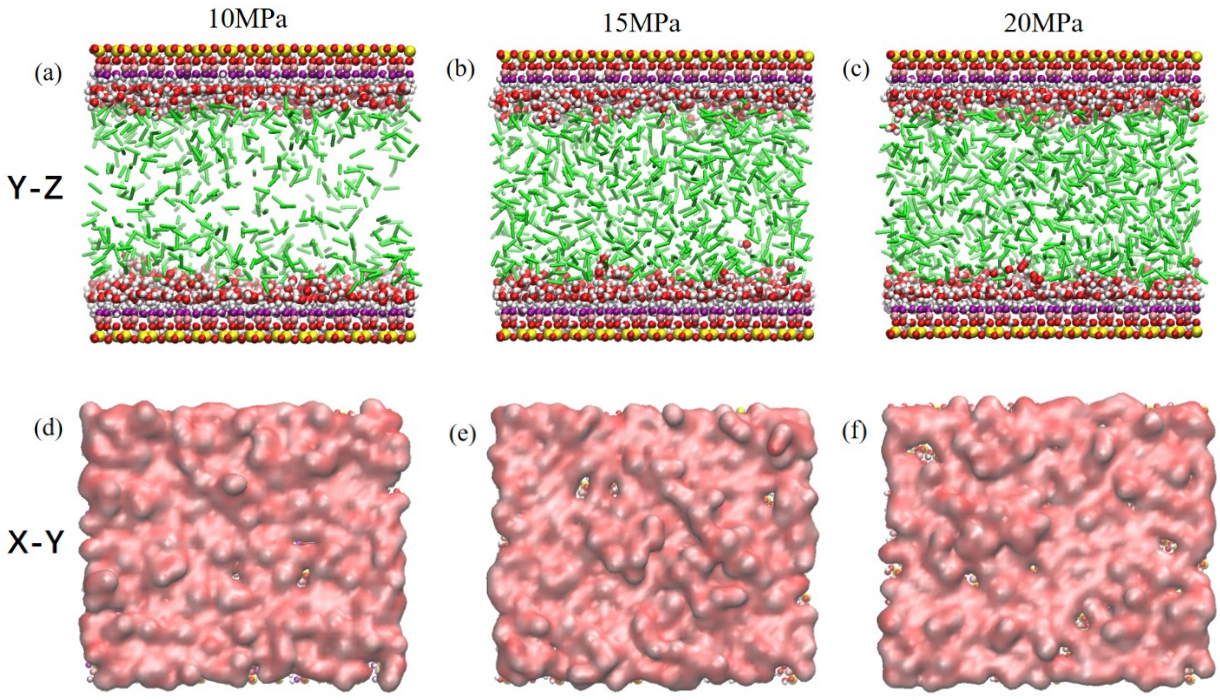

Figure A.4 Schematic representation of CO_2 and water molecular configurations in gibbsite kaolinite mesopores at (a) 10MPa; (b) 15MPa; (c) 20MPa and 333.15 K with the water concentration of 0.2 g/cm^3 from the *y-z* plane view. Water distribution pattern on gibbsite surfaces from the *x-y* plane view at (d) 10 MPa; (e) 15 MPa; (f) 20 MPa and 333.15 K in mesopores. For a better view, water molecules are presented in a quick-surf mode in VMD.

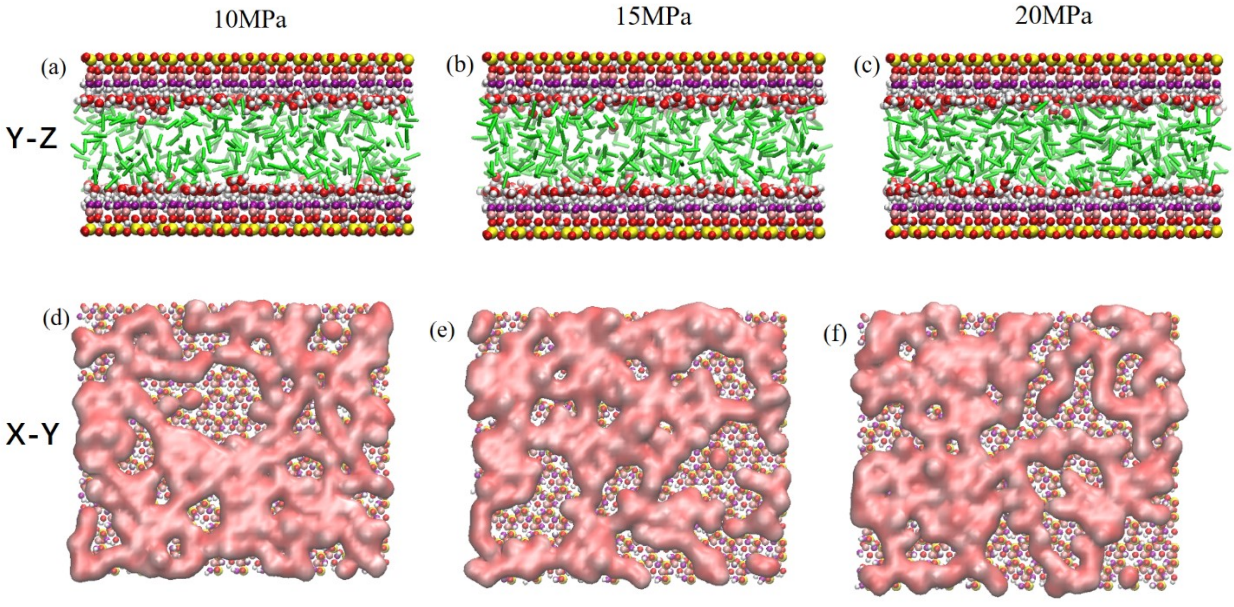

Figure A.5 Schematic representation of CO_2 and water molecular configurations in gibbsite kaolinite micropores at (a) 10MPa; (b) 15MPa; (c) 20MPa and 333.15 K with the water concentration of 0.2 g/cm^3 from the *y*-*z* plane view. Water distribution pattern on gibbsite surfaces from the *x*-*y* plane view at (d) 10 MPa; (e) 15 MPa; (f) 20 MPa and 333.15 K in micropores. For a better view, water molecules are presented in a quick-surf mode in VMD.

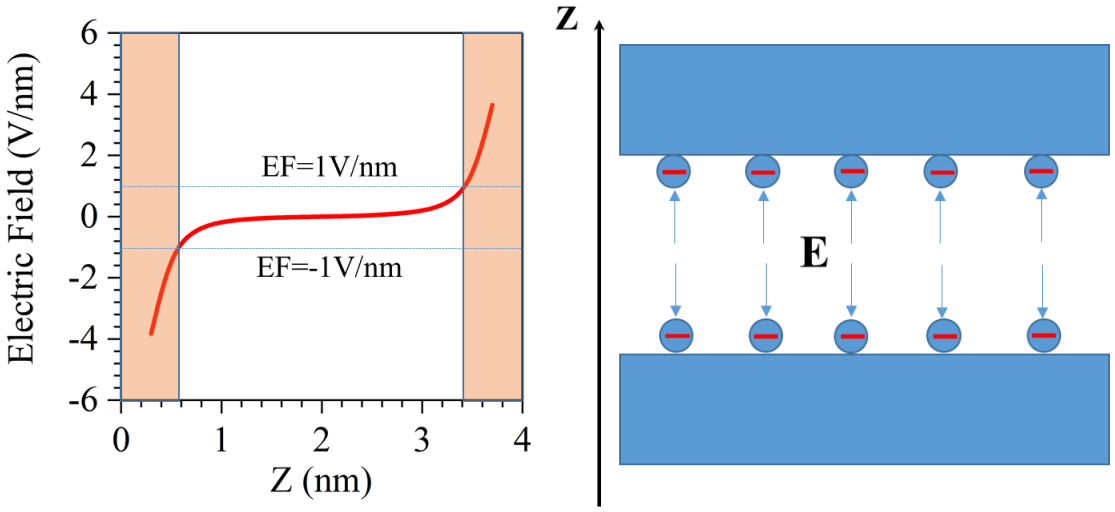

(a) (b)

Figure A.6 (a) Calculated electric filed in siloxane mesopores and (b) schematic graph of the electric field distribution inside the nanopores.

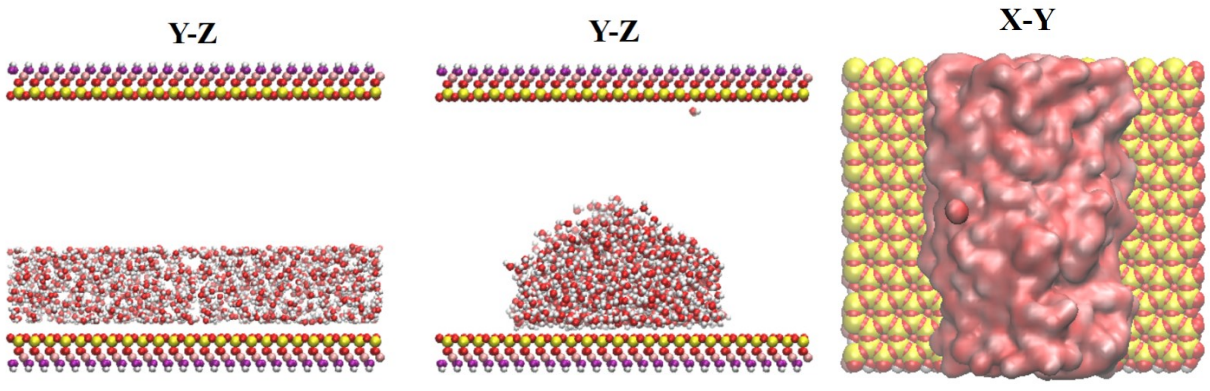

(a) (b) (c)

Figure A. 7 (a) Initial water distribution (on one side) from y-z plane view and final water structure (hemi-cylinder) after 20 ns from the (b) *y-z* and (c) *x-y* plane view in siloxane mesopores with the water concentration of 0.2 g/cm^3.

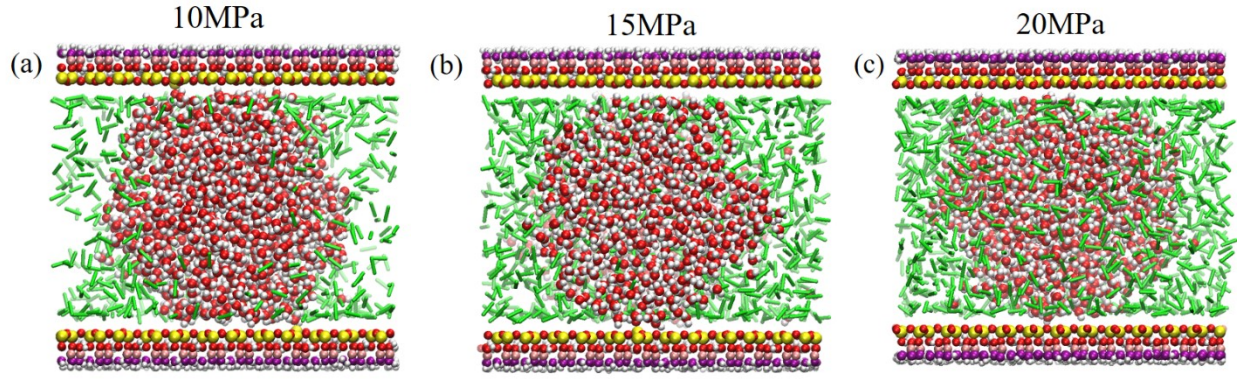

Figure A.8 Schematic representation of CO_2 and water molecular configurations in siloxane kaolinite mesopores at (a) 10 MPa; (b) 15 MPa; (c) 20 MPa from the *y-z* plane view with the water concentration of 0.2 g/cm^3.

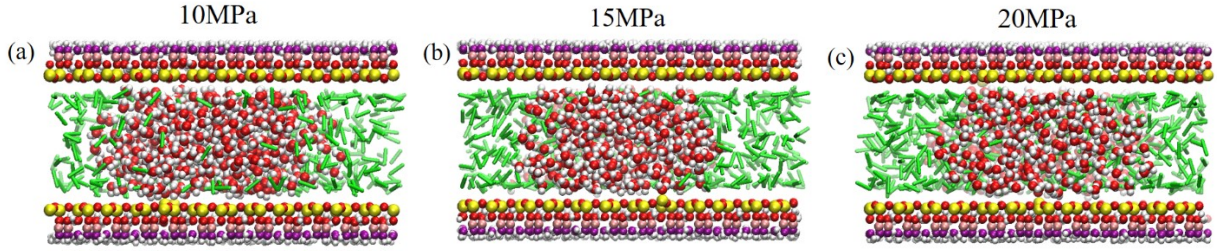

Figure A.9 Schematic representation of CO_2 and water molecular configurations in siloxane kaolinite micropores at (a) 10 MPa; (b) 15 MPa; (c) 20 MPa from the *y-z* plane view with the water concentration of 0.2 g/cm^3.

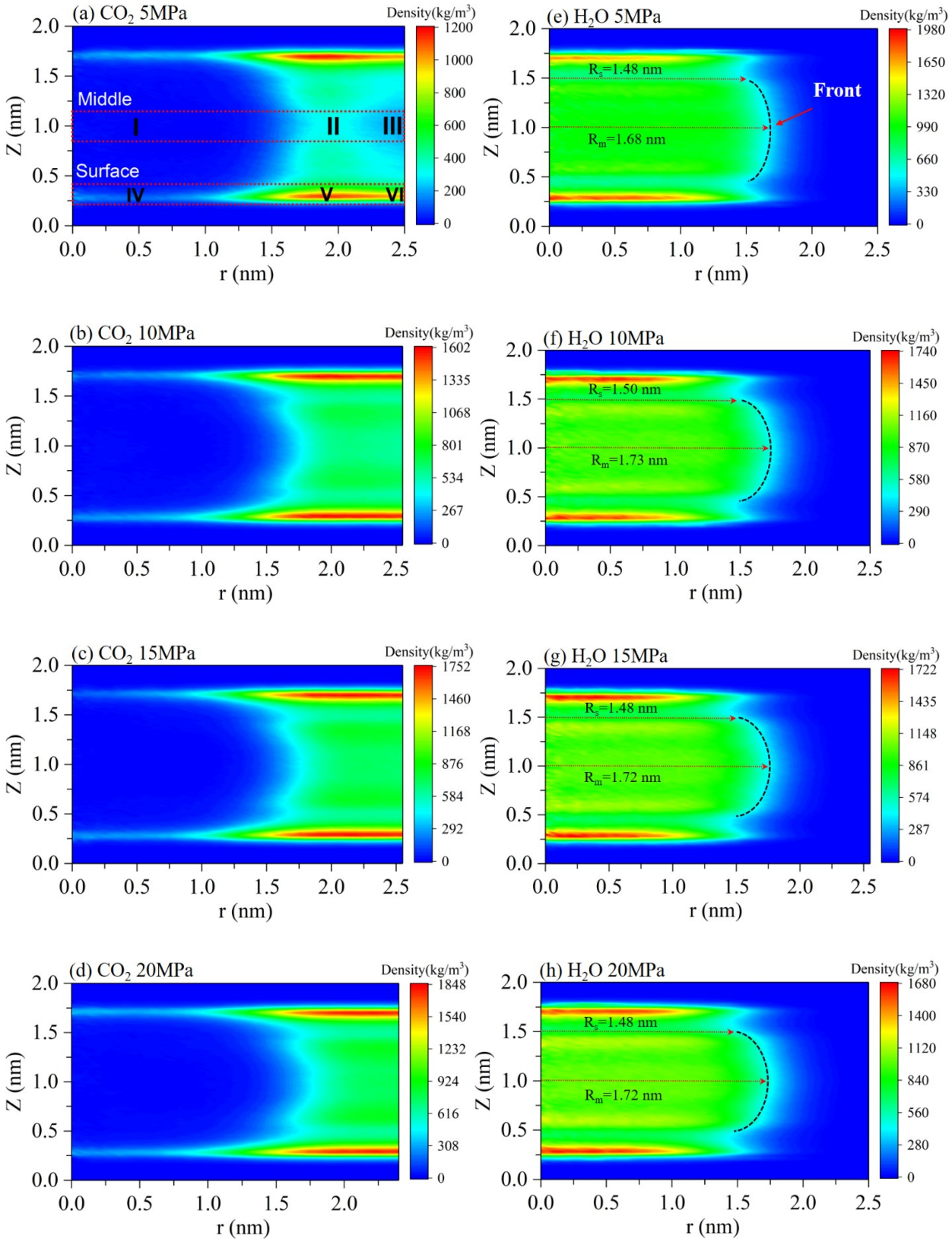
(a) CO2 5MPa
Density(kg/m3)
Middle
Surface
I
II
III
IV
V
VI
Z (nm)
r (nm)
(e) H2O 5MPa
Rs=1.48 nm
Rm=1.68 nm
Front
(b) CO2 10MPa
(f) H2O 10MPa
Rs=1.50 nm
Rm=1.73 nm
(c) CO2 15MPa
(g) H2O 15MPa
Rs=1.48 nm
Rm=1.72 nm
(d) CO2 20MPa
(h) H2O 20MPa
Rs=1.48 nm
Rm=1.72 nm

Figure A.10 2D Contour plots for the CO_2 and H_2O density using cylindrical coordinate with the cylinder axis crossing the mass center of water in siloxane mesopores at different pressure conditions.

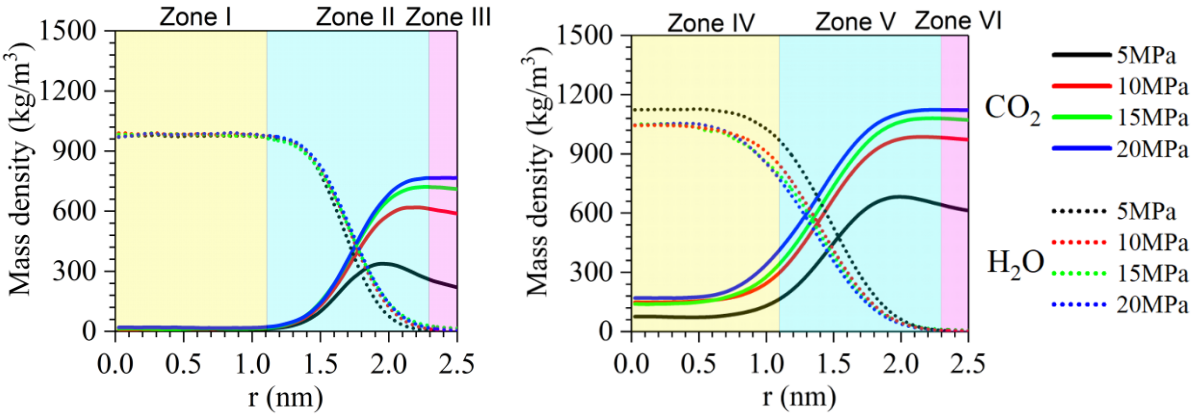

(a) (b)

Figure A.11 1D density profile of CO_2 and water along the radius of the cylinder within (a) middle ($0.75 \le z \le 1.25$ nm) and (b) surface areas ($0.2 \le z \le 0.4$ nm) of siloxane mesopores at different pressure conditions.

Appendix B

Table B.1 Potential parameters of hydrocarbons, CO_2 and clay.

Atom	ε (K)	σ (nm)	q (e)
Hydrocarbons[194]			
CH4	148	0.373	0
CH3	98.0	0.375	0
CH2	46.0	0.395	0
Carbon dioxide[121]			
C	27	0.28	+0.7
O	79	0.305	-0.35
Clay[118]			
st	0.000926	0.3302	+2.1
ob	78.2	0.3165	-1.05
obts	78.2	0.3165	-1.16875
oh	78.2	0.3165	-0.95
ho	0	0	+1.05
ao	0.000669	0.4271	+1.575
at	0.000926	0.3302	+1.575
K	50.3	0.3334	+1

Appendix C

C1. Umbrella sampling method for potential mean force (PMF) calculation

Within the framework of umbrella sampling, a series of windows along the reaction coordinate are needed. As a result, before the PMF calculations, two identical emulsion droplets and the corresponding counter-ions are placed in the water phase with an initial reaction coordinate of 12.5 nm defined as the separation distance d between their center of mass (COM). Then a 2-ns simulation is carried out to drag one of the emulsion droplets to approach the other one via the umbrella potential with the spring constant as 1000 KJ/mol/nm^2 and pull rate as 0.005 nm/ps, saving trajectory every 1 ps. Later on, a series of coordinate files in each frame are generated based on the pull trajectories. We select the configurations with d from ~6 nm to 12.5 nm with an interval of 0.15 nm to generate different reaction windows. The schematic diagram of the PMF calculation between two emulsion droplets for one specific window in Scenario I in **Figure C1.1**. Then, the umbrella sampling simulations are separately conducted in *NPT* ensemble at 1 bar and 300 K in each window for 30 ns (10-ns equilibration and last 20-ns runs for the PMF calculations) during which harmonic position constraints with a force constant of 1600 KJ/mol/nm^2 are employed to restrain the distance between the emulsion droplets. Temperature is controlled using the Nośe−Hoover thermostat algorithm [131], while pressure is kept constant with the Parrinello-Rahman pressure bath coupling [272]. Finally, the weighted histogram analysis method (WHAM) [273] is implemented in the GROMACS package to calculate PMF by merging each sampling window.

C2. Geometry determination of the emulsion droplet

The geometries of these emulsion droplets can be quantified by the asymmetry parameter α, which is defined as [274],

$$\alpha = \frac{2I_1 - I_2 - I_3}{I_1 + I_2 + I_3}, \tag{1}$$

where I_1, I_2, and I_3 represent principal moments of inertia ($I_1 > I_2 > I_3$). We note that the loose surfactant or oil molecules as discussed above are not considered as emulsion droplets. For a perfectly spherical emulsion droplet, $\alpha = 0$. However, an emulsion droplet can be generally considered as a spherical one if $\alpha \leq 0.05$ [274]. The asymmetry parameter probability distributions $P(\alpha)$ in **Scenario I**, **II**, and **III** are shown in **Figure C2.1**. We also provide the corresponding Gaussian fits, which are given as,

$$P(\alpha) = A \times \exp\left[\frac{(\alpha - \mu)^2}{\sigma^2}\right], \tag{2}$$

where A, σ, and μ denote the peak height, variance and expected value, respectively. Their values for **Scenario I**, **II**, and **III** are listed in **Table C2.1**. According to the Gaussian fittings, we calculate the coefficient of variation (CV), given as [275],

$$CV = \frac{\mu}{\sigma}. \tag{3}$$

If $CV < 1$, it can be regarded as a low-variance distribution [276]. All CV values (see **Table C2.1**) are less than 1, indicating that $P(\alpha)$ concentrate around μ. As μ for each case are in the range of 0.065~0.070, the geometries of these emulsion droplets can be roughly considered as spherical ones.

C3. PMF and density distribution analysis with H_3O^+

Similar to the PMF calculations between two emulsion droplets, the PMF between the emulsion droplet and H_3O^+ is obtained via the umbrella sampling method by dragging one H_3O^+ toward the emulsion droplet along Z-direction which generates a series of 0.15-nm spacing windows as discussed in **Section 4.2**. The force field for H_3O^+ is taken from Sagnella and Voth [277]. The PMF with respect to the reduced coordinates $(d^* - R_s)/\sigma_w$ as well as the charge distributions within the emulsion droplet are shown in **Figure C3.1**. Here d^* refers to the distance between the COM of emulsion droplet and H_3O^+. As H_3O^+ approaches the emulsion droplet, the PMFs tend to decrease moderately first, while dropping sharply when the H_3O^+ enters the region where the charge distribution of emulsion droplet becomes negative. Overall, the negative PMF results show that H_3O^+ exhibits a strong preference to be adsorbed at the nC_7-H_2O interfaces, though MEA molecules form the electrostatic pairings with the -COO^- head groups in PLA at the interface.

To better understand the H_3O^+ adsorption at the interface, we investigate their distributions near the emulsion droplet. Firstly, we place one typical emulsion droplet in **Scenario I** along with MEA molecules (111 in total) in water phase resulting in a box size of ~11 nm in each direction. Then, various numbers of H_3O^+ and Cl^- ions (5, 25, and 55 each) are added randomly to the system, followed by several 60 ns-*NPT* simulations (30 ns for equilibration and last 30 ns for data analysis) at 1 bar and 300 K to analyze H_3O^+ distributions. The fluid density distributions in **Scenario I** with different number of H_3O^+ molecules are shown in **Figure C3.2**. It shows that H_3O^+ has an enrichment at the nC_7-H_2O interface and as H_3O^+ concentration increases, MEA molecules are gradually depleted from the interface.

Table C2.1 Gaussian fitting parameter of $P(\alpha)$ in **Scenario I**, **II**, and **III**

Scenario	A	μ	σ	CV
I	0.085	0.065	0.023	0.35
II	0.080	0.067	0.024	0.36
III	0.078	0.071	0.029	0.41

Table C.1 Simulation results in comparison to experimental data for validation

Density

Compounds	Exp. (g/cm^3)	Sim. (g/cm^3)	Relative Error (%)
LA	0.8634 [249] (333.15 K and 1 bar)	0.8749±0.032	1.33
nC_7	0.6796 [248] (298.15 K and 1 bar)	0.6921±0.028	1.82

IFT comparisons

IFT	Exp. (mN/m)	Sim. (mN/m)
nC_7-H_2O	50.2 [251] (298.15 K and 1 bar)	45.14±0.09
LA-H_2O	8.7 [250] (348.15 K and 1 bar)	15.39±0.36

LA-H_2O IFT with various surface concentrations of DLA (Na^+ as counter-ion)

DLA Surface concentration (#/nm^2)	0	0.2	0.4	0.8	1.2
IFT (mN/m)	15.39±0.36	13.39±0.27	12.28±0.34	11.04±0.29	8.74±0.26

Table C.2 nC_7-H_2O IFT in the presence of DLA molecules at the interface (MEA as counter-ion)

DLA Surface concentration (#/nm^2)	0	1	1.8	2.6
IFT (mN/m)	45.14±0.09	38.89±0.15	27.46±0.24	11.90±0.35

Table C.3 Gaussian fitting parameter of $P(R_s)$ in **Scenario I**, **II**, and **III**

Scenario	A **(nm)**	μ **(nm)**	σ **(nm)**	CV
I	0.151	2.91	0.30	0.10
II	0.102	2.92	0.40	0.14
III	0.086	2.75	0.43	0.16

Table C.4 Radius of select emulsion droplets in each scenario based on various methods

Select Emulsion Droplet	R_s [1] (nm)	R_s [2] (nm)	Relative Error[4] (%)	R_s [3] (nm)	Relative Error[4] (%)
Scenario I_1	2.94	3.00	2.04	3.20	8.84
Scenario I_2	2.74	2.80	2.19	3.00	9.48
Scenario I_3	2.71	2.75	1.48	2.92	7.75
Scenario I_4	3.13	3.15	0.63	3.38	7.98
Scenario II_1	2.83	2.86	1.06	3.10	9.54
Scenario II_2	3.18	3.20	0.68	3.47	8.35
Scenario II_3	2.96	3.00	1.35	3.23	9.12
Scenario II_4	3.38	3.50	3.55	3.72	10.06
Scenario III_1	2.62	2.65	1.15	2.90	10.68
Scenario III_2	2.96	2.95	0.33	3.25	9.79
Scenario III_3	3.62	3.60	-0.56	3.96	9.40
Scenario III_4	1.74	1.70	-2.30	1.85	6.32

R_s^1**:** calculated based on effective gyration radius R_g^* of the nC7 & LAs within a given emulsion droplet as discussed in the main text.

R_s^2**:** obtained from peak position of $O1_{DLA}$ in number density profile

R_s^3**:** obtained from position of 90% bulk water density in number density profile

$$Relative\ error^4 = \frac{(R_s^i - R_s^1)}{R_s^1} \times 100\%,\ (\ i = 2 \text{ or } 3\ )$$

Table C.5 Averaged H-bonding number between LAs and H_2O per LA molecule in different scenarios

Scenario	I	II	III	IV	V	VI
H-bonding	**DLA**			**PLA**		
	5.6±0.11	5.4±0.13	5.3±0.12	2.2±0.06	2.1±0.05	2.0±0.05

Table C.6 HN of head groups in LAs in different scenarios**.**

Scenario	I	II	III	IV	V	VI
HN	**DLA**			**PLA**		
	3.16	3.03	2.91	1.91	1.89	1.86

Table C.7 Gaussian fitting parameter of $P(\alpha)$ in **Scenario IV**, **V**, and **VI.**

Scenario	A	μ	σ	CV
IV	0.113	0.042	0.018	0.43
V	0.114	0.042	0.018	0.43
VI	0.112	0.041	0.017	0.41

Table C.8 nC_7-H_2O IFT in the presence of PLA molecules at the interface with various surface concentration (with MEA and HCO_3^- in aqueous solution).

PLA Surface concentration (#/nm^2)	0	1	1.8	2.6
IFT (mN/m)	45.14±0.09	40.51±0.11	32.23±0.19	25.25±0.32

Table C.9 Averaged H-bonding number between PLA and MEA or HCO_3^- per PLA in different scenarios.

Scenario	IV	V	VI
PLA-MEA	0.011±0.004	0.015±0.003	0.019±0.004
PLA-HCO_3^-	0.021±0.006	0.029±0.006	0.038±0.006

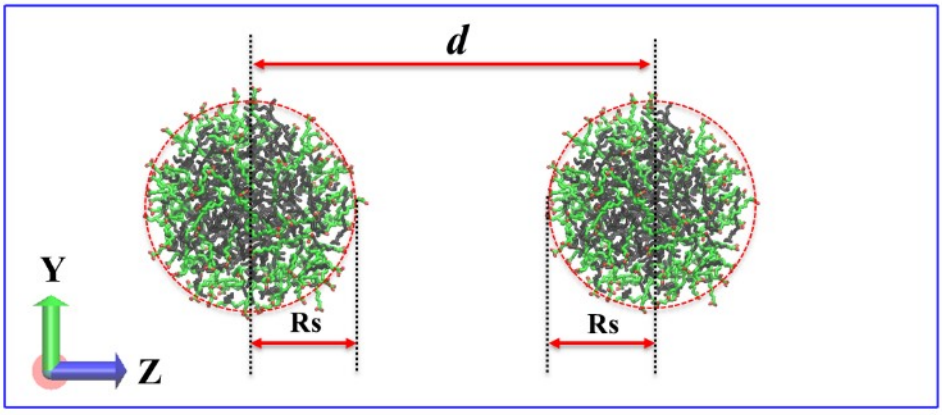

Figure C1.1 Schematic representation of PMF calculations between two emulsion droplets for one specific window in **Scenario I**. The color scheme is the same as **Figure 5.1**. For clarity, H_2O molecules and MEAs are not shown here.

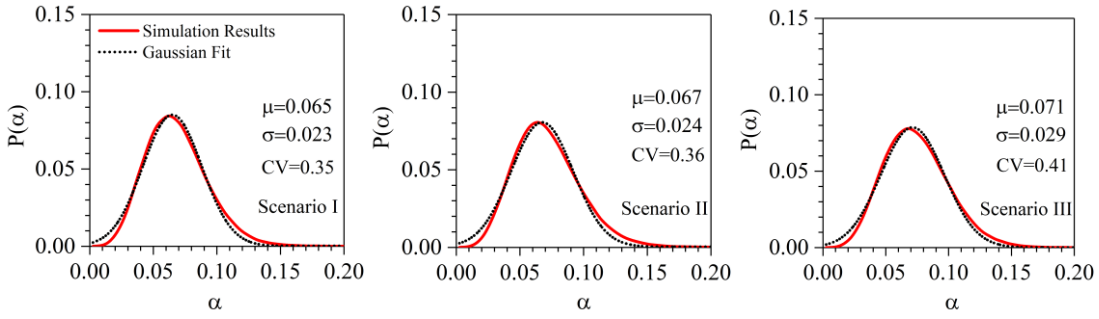

(a) (b) (c)

Figure C2.1 $P(\alpha)$ and the corresponding Gaussian fitting in **Scenario** (a) **I**; (b) **II**; (c) **III**.

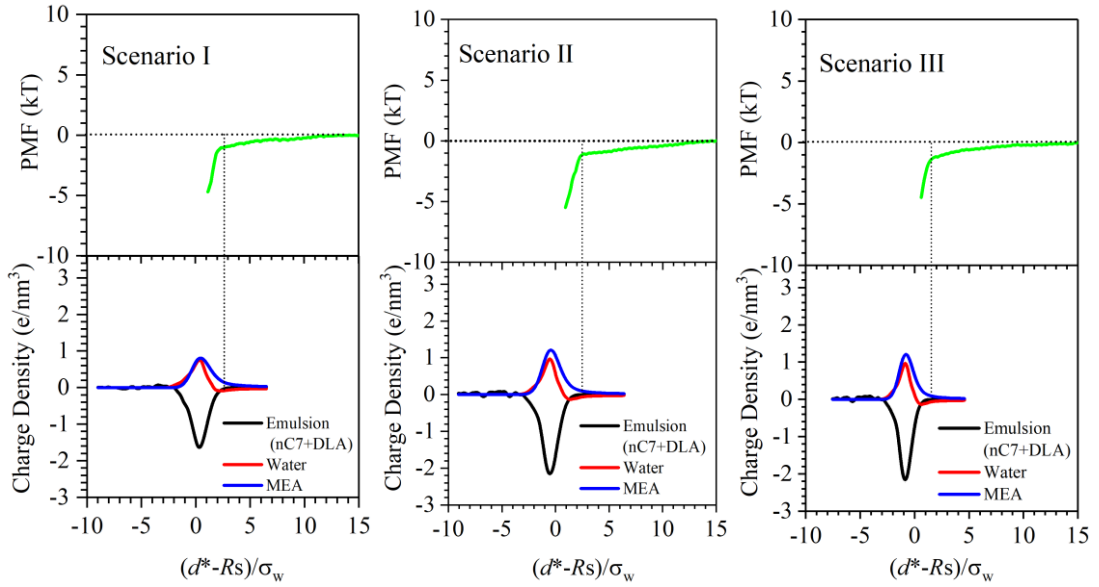

(a) (b) (c)

Figure C3.1 PMF results between emulsion and H_3O^+ and charge density distribution of different species within a given emulsion droplet with respect to reduced coordinates $(d^* - R_s)/\sigma_w$ in different scenarios.

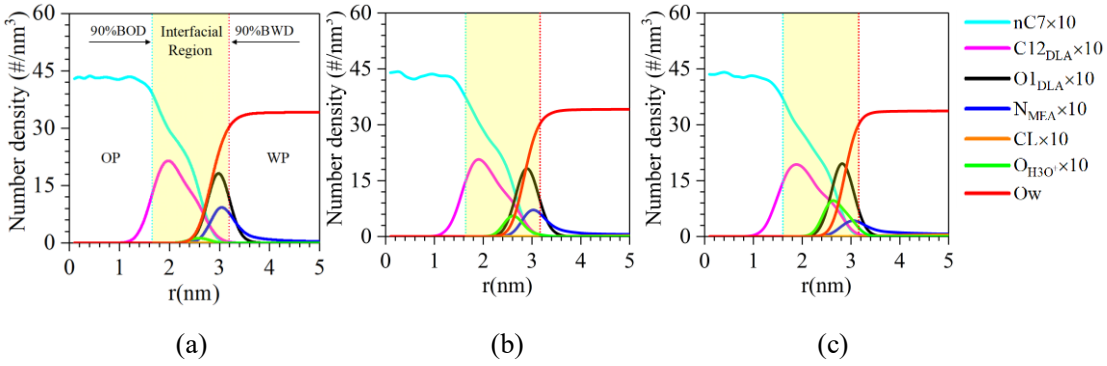

Figure C3.2 Number density distribution of different species within a given emulsion droplet with respect to its COM with (a) 5 (b) 25 and (c) 55 H_3O^+ in the system (each system contains 111 MEA). OP, WP, BOD and BWD denote oil phase, water phase, bulk oil density and bulk water density, respectively. $C12_{DLA}$, $O1_{DLA}$, N_{MEA}, $O_{H3O}{}^+$ represent C12 atoms in PLA, O1 atoms in DLA, N atoms in MEA and O atoms in H_3O^+, respectively.

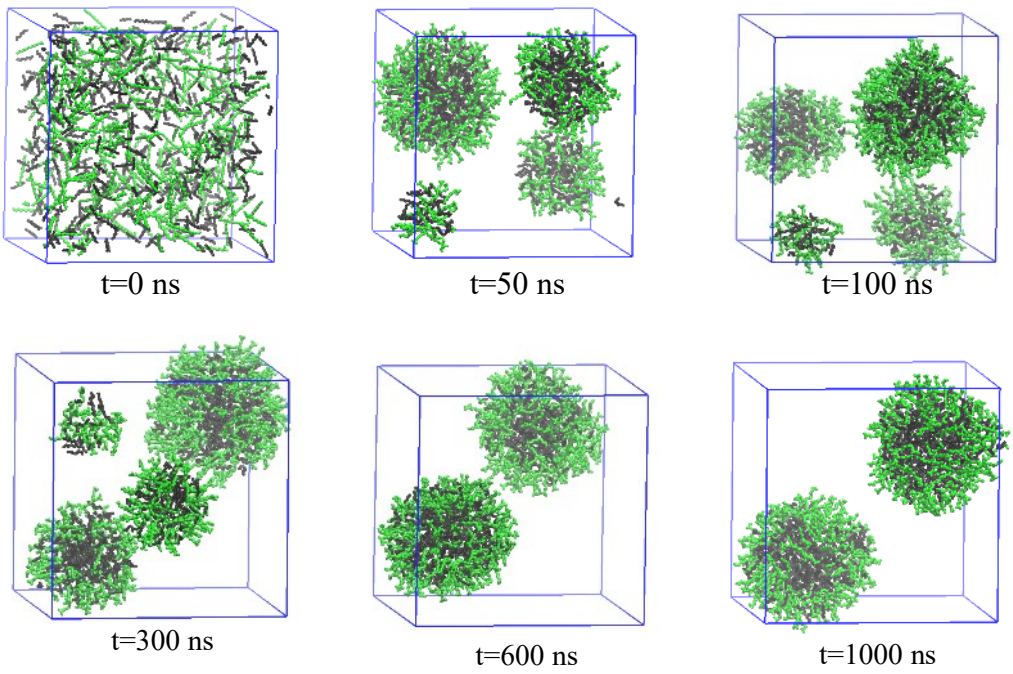

Figure C.1. Formation of O/W emulsion droplets and their evolution (0, 50, 100, 300, 600, and 1000 ns) for one specific initial configuration in **Scenario II**. We use green and black colors to represent DLA and nC_7, respectively. For clarity, H_2O molecules and MEAs are not shown here.

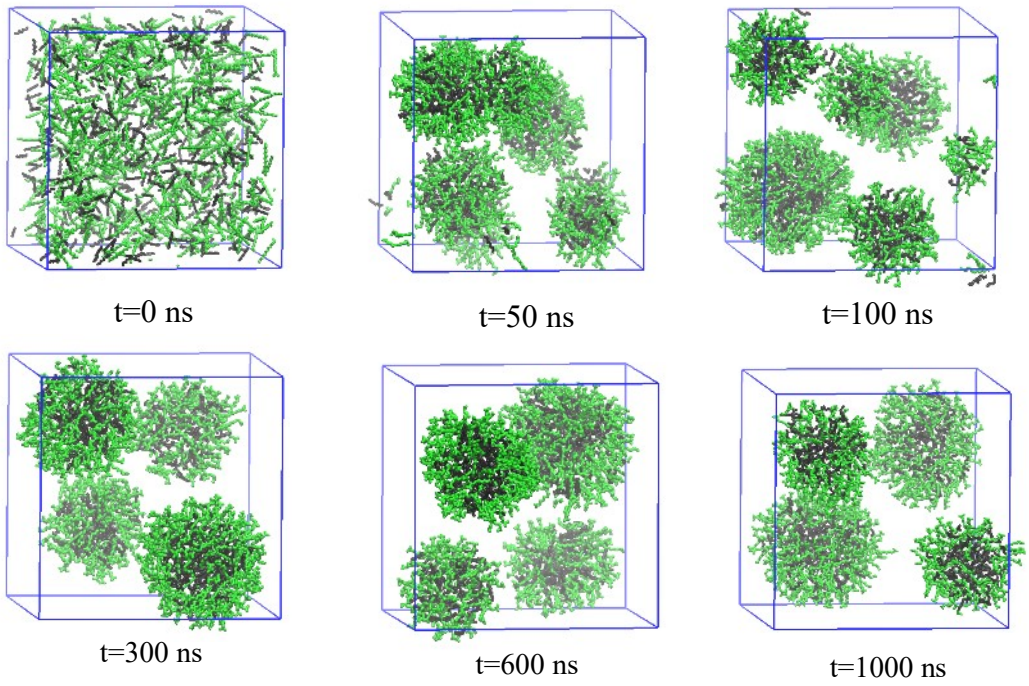

Figure C.2 Formation of O/W emulsion droplets and their evolution (0, 50, 100, 300, 600, and 1000 ns) for one specific initial configuration in **Scenario III**. We use green and black colors to represent DLA and nC_7, respectively. For clarity, H_2O molecules and MEAs are not shown here.

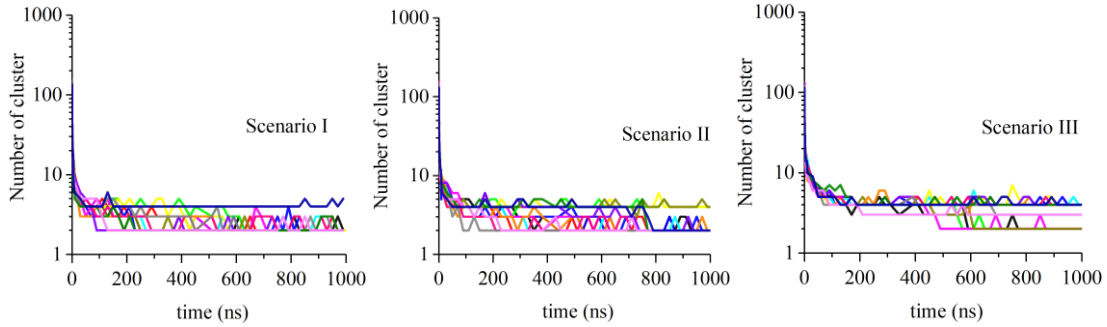

Figure C.3 Evolution of emulsion droplet number in the system in different scenarios with different initial configurations. Various colors represent different initial configuration cases.

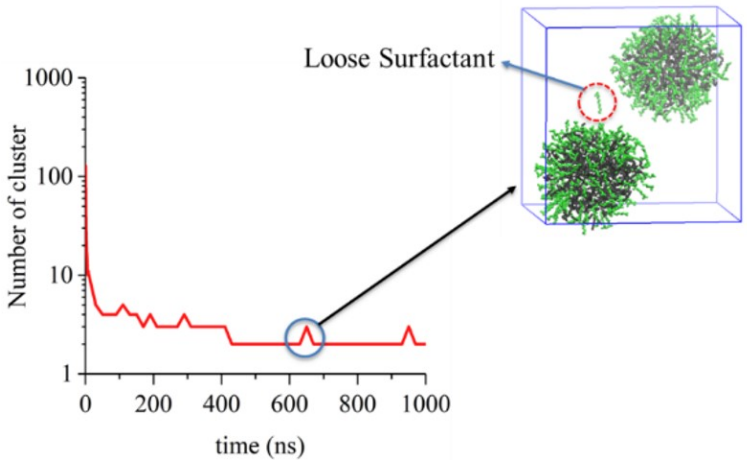

Figure C.4 One specific molecular configuration with loose surfactant detached from the emulsion droplets in **Scenario I**.

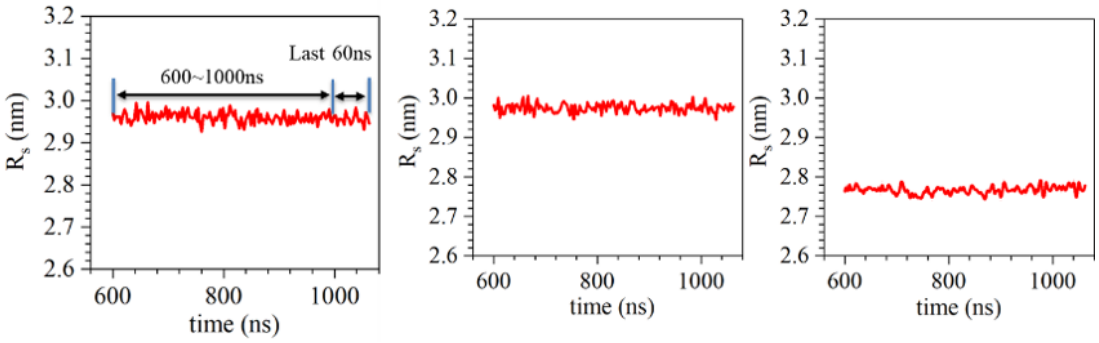

(a) (b) (c)

Figure C.5 Evolution of R_s for select emulsion droplets from 600 ns to 1060 ns in (a) **Scenario I**; (b) **Scenario II**; (c) **Scenario III**.

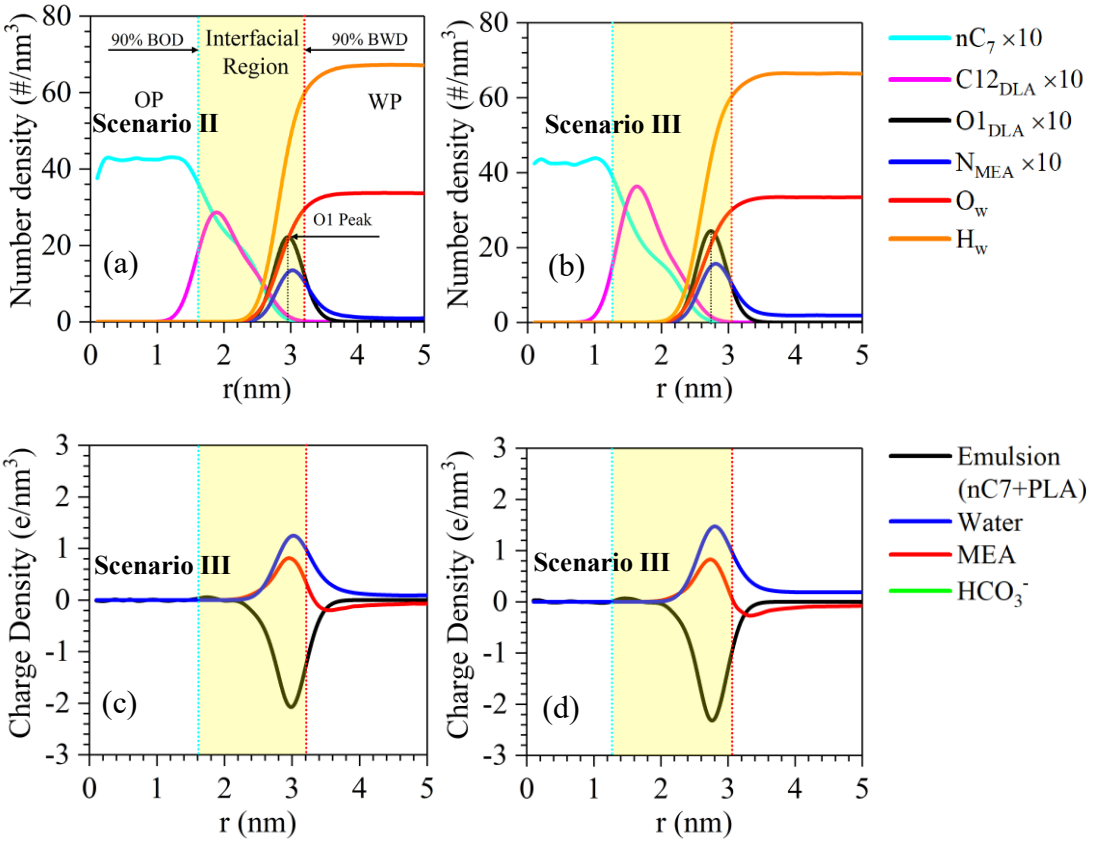

Figure C.6 (a-b) Number density distribution; (c-d) Charge density distribution of different species within a given emulsion droplet with respect to its COM in different scenarios. OP, WP, BOD and BWD denote oil phase, water phase, bulk oil density and bulk water density, respectively. $C12_{DLA}$, $O1_{DLA}$ and N_{MEA} represent C12 atoms in DLA, O1 atoms in DLA and N atoms in MEA as shown in **Figure. 4.1**, respectively.

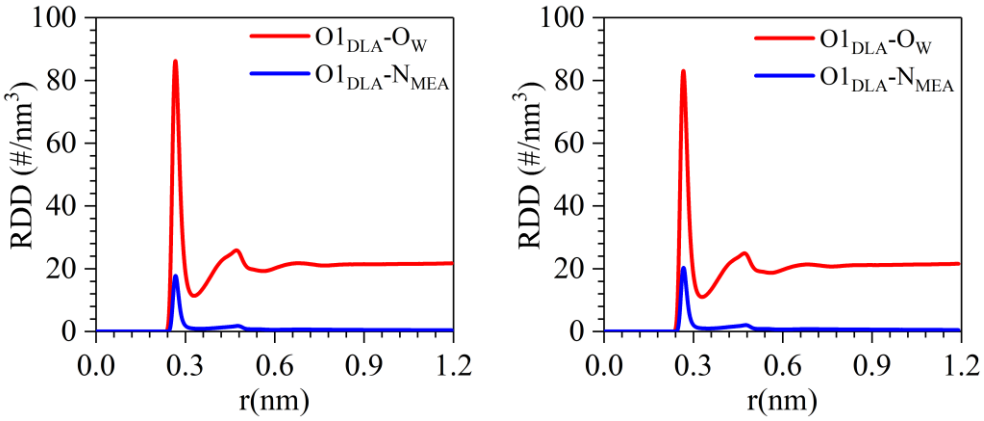

(a) (b)

Figure C.7 RDD of Ow and N_{MEA} around $O1_{DLA}$ in (a) **Scenario II**; (b) **Scenario III.**

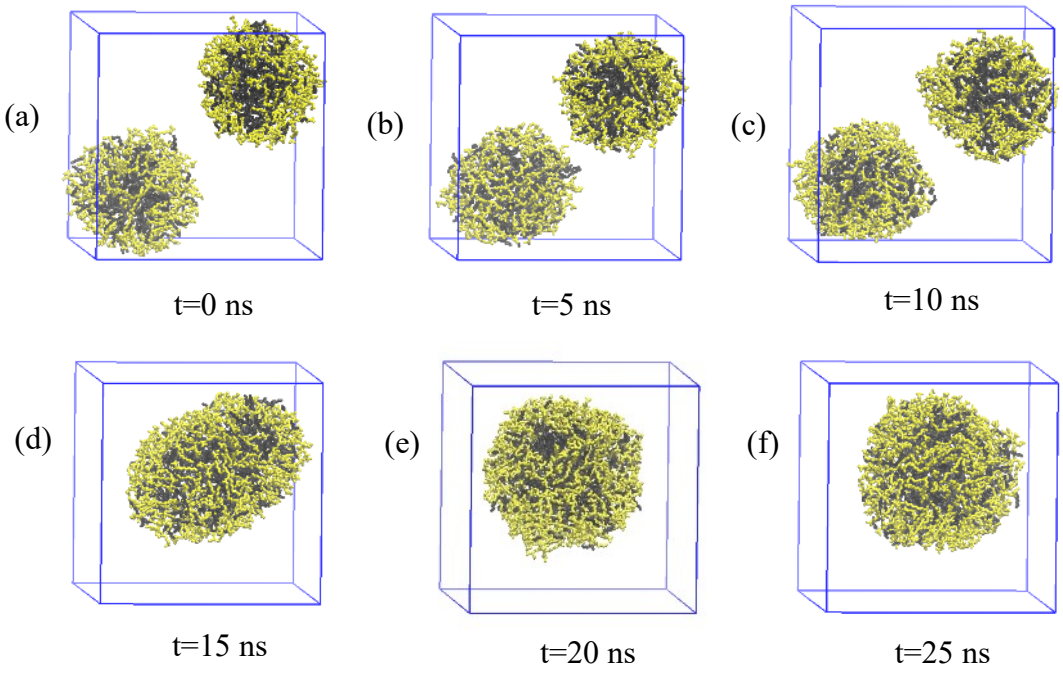

Figure C.8 Coalescence of O/W emulsion droplets and their evolution (0, 5, 10, 15, 20, and 25 ns) for one specific initial configuration in **Scenario V**. The yellow color represents PLA molecules, while nC_7 molecules are described by black color. For clarity, H_2O, MEA, and HCO_3^- are not shown here.

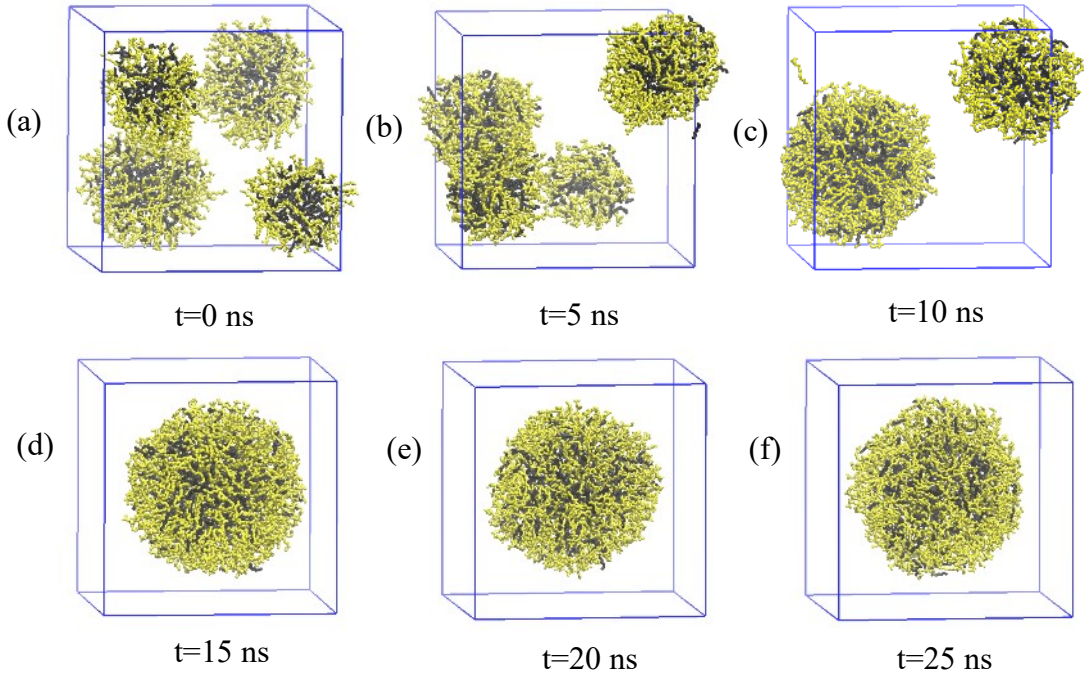

Figure C.9 Coalescence of O/W emulsion droplets and their evolution (0, 5, 10, 15, 20, and 25 ns) for one specific initial configuration in **Scenario VI**. The yellow color represents PLA molecules, while nC_7 molecules are described by black color. For clarity, H_2O, MEA, and HCO_3^- are not shown here.

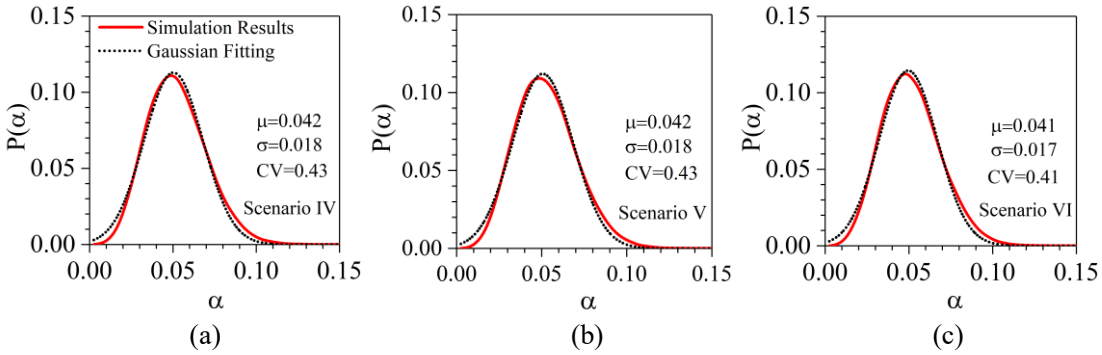

Figure C.10 Asymmetry parameter distributions $P(\alpha)$ and the corresponding gaussian fitting in (a) **Scenario IV**; (b) **Scenario V**; (c) **Scenario VI**.

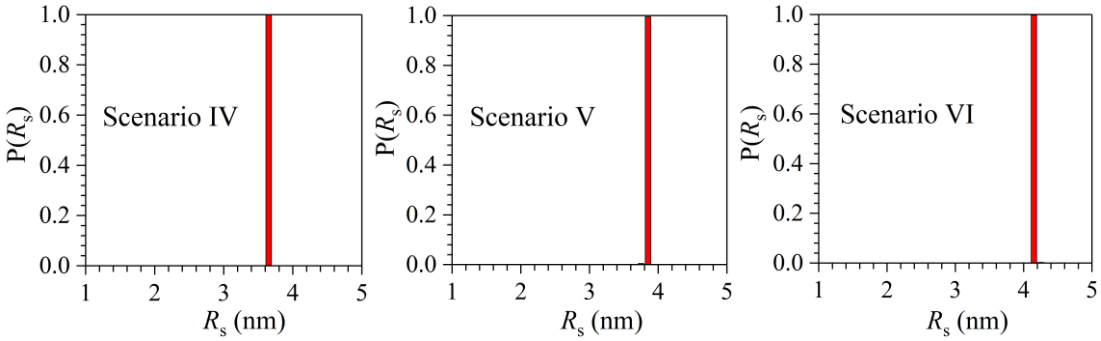

Figure C.11 $P(R_s)$ distribution of emulsions in (a) **Scenario IV**; (b) **Scenario V**; (c) **Scenario VI**.

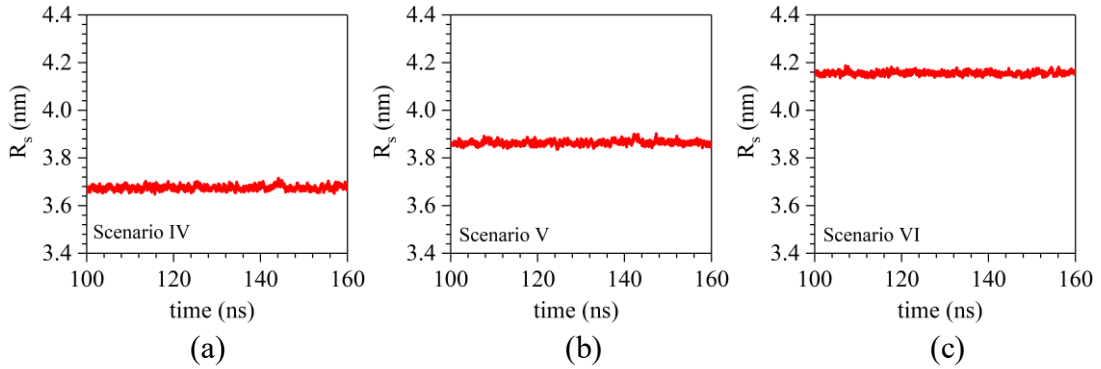

Figure C.12 Evolution of R_s for selected emulsion droplets from 100 ns to 160 ns in (a) **Scenario IV**; (b) **Scenario V**; (c) **Scenario VI**.

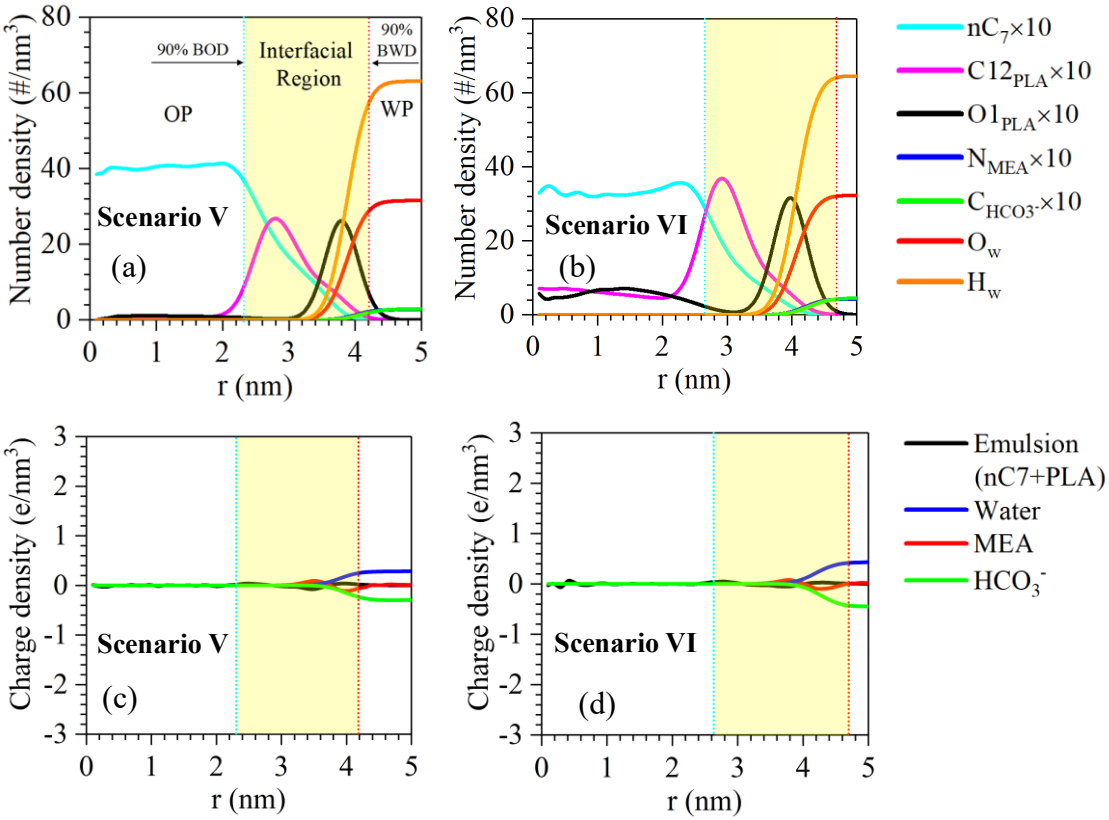

Figure C.13 (a-b) Number density distribution; (c-d) Charge density distribution of different species within a given emulsion droplet with respect to its COM in different scenarios. OP, WP, BOD and BWD denote oil phase, water phase, bulk oil density and bulk water density, respectively. $C12_{PLA}$, $O1_{PLA}$, N_{MEA}, C_{HCO3^-} represent C12 atoms in PLA, O1 atoms in PLA, N atoms in MEA and C atoms in HCO_3^- as shown in **Figure. 4.1**, respectively.

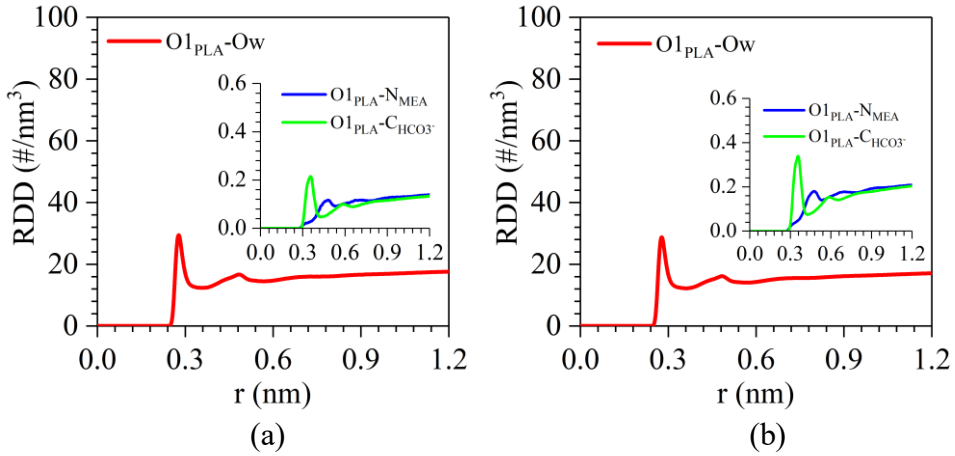

Figure C.14 RDD of Ow, N_{MEA} and C_{HCO3^-} around $O1_{PLA}$ in (a) **Scenario V and** (b) **Scenario VI.**